Transmissibility Operators For State and Output Estimation In Nonlinear Systems

Abdelrahman Khalil

Department of Mechanical Engineering
Memorial University of Newfoundland

This dissertation is submitted for the degree of
Doctor of Philosophy

March 2023

Abstract

Transmissibility operators are mathematical objects that characterize the relationship between two subsets of responses of an underlying system. The importance of transmissiblity operators comes from the fact that these operators are independent on the system inputs. This work develops the transmissibility theory for nonlinear systems for the first time. The system nonlinearities are assumed to be unknown, which gives a wide range of possible engineering applications in different disciplines. Four different methods are developed to deal with these nonlinearities. The first method is by re-constructing the system nonlinearities as independent excitations on the system. This method handles the inherent unmodeled nonlinearities within the system. The second method is by designing a transmissibility-based sliding mode control. This method rejects unwanted nonlinearities such as system faults. The third method is by constructing the system as time-variant linear system, and use recursive least squares to solve it. This method can handle nonlinear systems with time-variant dynamics. The fourth method is by designing a new robust estimation technique called high-gain transmissibility (HGT) that is inspired by high-gain observers. This estimator has the ability to robustly estimate the system states in a high-gain form.

The majority of modern fault detection, control systems, and robots localization depend on mathematically estimating the system states and outputs. Transmissibility-based estimation is incorporated in this work with these three theoretical applications. For fault detection, transmissibility operators are used along a set of outputs to estimate the measurements of another set of outputs. Then faults are detected by comparing the estimated and measured outputs with each other. Control approaches use the transmissibility-based estimation to construct the control signal, in which is injected back to the original system. Robots localization fuses the transmissibility-based estimation with real-time sensor measurements to minimize the error in determining the robot displacements.

These three theoretical applications are applied on four different systems. The first system is Connected Autonomous Vehicles (CAV) platoons. A CAV platoon is a network of connected autonomous vehicles that communicate together to move in a specific path with the desired velocity. Transmissibilities are proposed along with the measurements from sensors available in CAV platoons to identify transmissibility operators. This will be then

developed to mixed autonomous and human-driven vehicle platoons. Besides the wide range of physical and cyber faults in such systems, this is also motivated by the fact that on-road human-drivers' behaviour is unknown and difficult to be predicted. Transmissibility operators are used here to handle both cyber-physical faults as well as the human-drivers' behaviour. The platoon faults are then proposed to be mitigated using a transmissibility-based sliding mode controller. Moreover, transmissibilities are integrated with Kalman filter to localize CAV platoons while operating under non-Gaussian environment as unknown nonlinearities.

The second system is a multi-actuator micro positioning system that is used in the semi-conductors industry. Transmissibility operators are applied on this system for fault detection and fault-tolerant control. Fault detection is represented in applying the proposed developments to actuator fault detection. Some of the most common actuator faults such as actuator loss of effectiveness and fatigue crack in the connection hinges will be considered. Transmissibilities then will be used for fault detection without knowledge of the dynamics of the system or the excitation that acts on the system. Next, a transmissibility-based sliding mode control will be implemented to mitigate common actuator faults in multi-actuator systems.

The third system is flexible structures subjected to unknown and random excitations. Structures used in applications subjected to turbulent fluid flow such as aerospace and underwater applications are subjected to random excitations distributed along the structure. Transmissibility operators are used for the purpose of structural fault detection and localization during the system operation. The fourth system is robotic manipulators with bounded nonlinearities and time-variant parameters. Both parameter variation and system nonlinearities are considered to be unknown. Transmissibility operators are integrated with Recursive Least Squares (RLS) to overcome the unknown variant parameters. RLS identifies transmissibilities used in the structure of noncausal FIR (Finite Impulse Response) models. While parameter variation can be treated as system nonlinearities, the RLS algorithm is used to optimize what time-variant dynamics to include in the transmissibility operator and what dynamics to push to the system nonlinearities over time. The identified transmissibilities are then used for the purpose of fault detection in an experimental robotic arm with variant picked mass.

وَمَا تَوْفِيقِي إِلَّا بِاللَه

To my loving parents . . .

Declaration

I hereby declare that except where specific reference is made to the work of others, the contents of this dissertation are original and have not been submitted in whole or in part for consideration for any other degree or qualification in this, or any other university. This dissertation is a result of work done in collaboration with my advisors and contains nothing which is the outcome of work done in collaboration with others. This dissertation contains fewer than 34,000 words including equations and appendices and has 95 figures.

Abdelrahman Khalil
March 2023

Acknowledgements

I would like to express my special gratitude to my supervisor, Professor Mohammad Al Janaideh, for his supervision and guidance. I thank my advisors, Professor Khaled Aljanaideh and Professor Almuatazbellah Boker, for helping me establish a solid background on which this dissertation was built. Also, I thankfully acknowledge the effort of each instructor, engineer, and colleague who helped me over the last four years; thank you all for your instructions, suggestions, and support.

Special thanks go to my family for their good wishes, especially my brothers Mohammed and Abdulaziz. Special thanks go to my close friend Kevin Hank for standing by my side on every hard day while pursuing this degree. My deepest gratitude for my close friend Alexis Goffin for his encouragements when the time got rough. Special thanks to my close friend Fady Abu-Zeyad for his continuous good wishes. I would also like to thank my good friends Marcos, Laural, Pier-Ann, Ahmed, Jean-Philippe, Aylar, Christian, Mike, Ashley, Derek, Rachel, Eric, and all "Dyslexia" friends for every good day they made me had while pursuing this degree. I am deeply grateful to all the support, appreciation, encouragements, and keen interest in my academic achievements.

Table of contents

Co-authorship Statement

Fortunately, this thesis is written as a collection of peer-reviewed papers published in collaboration with my advisors. This statement is to clarify the origins of each section and the candidate's contributions in each of these papers. The content of the following papers has not been used in any form towards any other degree or qualification. The co-authors of these papers acted as my academic advisors while pursuing this doctorate.

The work in Section 3.4 was published in

- **Abdelrahman Khalil**, Mohammad Al Janaideh, Khaled F. Aljanaideh, and Deepa Kundur, "Transmissibility-Based Health Monitoring of the Future Connected Autonomous Vehicles Networks", *IEEE Transactions on Vehicular Technology*, vol. 71, no. 4, 3633-3647, 2022.

Dr. M. Al Janaideh suggested applying transmissibilities to connected autonomous vehicle platoons first through this paper. I conducted the literature survey, generated the required algorithms, and conducted all experiments. Dr. K. Aljanaideh gave me guidance and reviewed my work before publication. The work in Section 3.5 was published in

- **Abdelrahman Khalil**, Khaled F. Aljanaideh, and Mohammad Al Janaideh, "On Detecting Drunk Drivers in Mixed Autonomous Platoons Using Vehicles Velocity Measurements", *IEEE/ASME Transactions on Mechatronics*, vol. 27, no. 6, 6006-6017, 2022.

Dr. K. Aljanaideh suggested extending this work to detect drunk drivers. I conducted all required work myself under his guidance. The structural fault detection in Section 3.6 was published in

- **Abdelrahman Khalil**, Khaled F. Aljanaideh, and Mohammad Al Janaideh, "Sensor Measurements Only with Transmissibility Operators for Fault Detection in Flexible Beams", *IEEE Sensors Journal*, vol. 22, no. 18, 17977-17987, 2022.

Dr. K. Aljanaideh suggested the idea, and I conducted all work under his guidance. The structural fault localization in Section 3.6 is in

- **Abdelrahman Khalil**, Khaled F. Aljanaideh, and Mohammad Al Janaideh, "Early Crack Localization in Flexible Structures Subjected to Unknown Disturbances using Sensor-Measurements Only", *IEEE/ASME Transactions on Mechatronics*, In Press.

In this paper, I suggested the idea, generated the algorithms, and conducted all required work and experiments. The work in Section 3.7 is published in

- **Abdelrahman Khalil**, Khaled F. Aljanaideh, and Mohammad Al Janaideh, "Output-Only Measurements for Fault Detection of Multi-Actuator Systems in Motion Control Applications“, *IEEE Sensors Journal*, vol. 22, no. 5, 4164-4174, 2022.

Dr. M. Al Janaideh directed applying transmissibilities to detect faults in multi-actuator systems. I conducted the literature survey, generated the required algorithms, and conducted all experiments. Dr. K. Aljanaideh gave me guidance.

The work in Section 4.3 are published in

- **Abdelrahman Khalil**, Khaled F. Aljanaideh, and Mohammad Al Janaideh, "On Connected Autonomous Vehicles With Unknown Human Driven Vehicles Effects Using Transmissibility Operators“, *IEEE Transactions on Automation Science and Engineering*, Early Access, 2022.

Dr. M. Al Janaideh directed this work, and suggested comprising sliding mode control. I managed the merge between transmissibilities and sliding mode, and conducted the stability analysis with all required experiments. Dr. K. Aljanaideh gave me guidance and reviewed the transmissibility merge with sliding mode control.

The work in Chapter 5 is in

- **Abdelrahman Khalil**, Khaled F. Aljanaideh, and Mohammad Al Janaideh, "Transmissibility-based Fault Detection for Robotic Applications with Time-Varying Parameters“, *IEEE/ASME Transactions on Mechatronics*, Early Access, 2023.

This work suggests a novel solution for a well-known issue in the literature. This issue is distinguishing normal dynamic changes from abnormal changes (faults). I suggested the solution and conducted the required mathematical theorem with its proof as well as all required experiments. Dr. K. Aljanaideh reviewed the mathematical theorem along with its proof.

The work in Chapter 6 is in

- **Abdelrahman Khalil**, Allmutazbellah Boker, and Mohammad Al Janaideh, "High-Gain Transmissibility for State Estimation in Systems With Multi Unknown Nonlinearities." *IEEE Conference on Decision and Control*, 5639-5644, Cancun, Mexico, 2022.

The idea of this work was conceived after multiple tries that I suggested. I led all theoretical developments as well as all required experiments. Dr. A. Boker gave theoretical guidance and reviewed the developed theorem and its proof.

The work in Chapter 7 is in

- **Abdelrahman Khalil**, Allmutazbellah Boker, Khaled F. Aljanaideh, and Mohammad Al Janaideh, "Transmissibility-based Kalman Filtering For Systems With Non-Gaussian Process Noise", Accepted for Publications at *American Control Conference*, San Diego, California, 2023.

The idea of this work came to my mind while studying for my comprehensive exam. I proposed it to my advisors, then conducted all the required work.

List of figures

List of tables

Nomenclature

Roman Symbols

$\bar{u}$	System control commands
$\hat{y}_{\mathrm{o}}$	Transmissibility-based estimation of the output y_{o}
$\tilde{v}_i$	Corrupted velocity of the ith autonomous vehicle
A	State matrix of the state space structure
B	Input matrix of the state space structure
B_f	State space input matrix corresponds to f
B_u	State space input matrix corresponds to $\bar{u}$
B_w	State space input matrix corresponds to w
C	Output matrix of the state space structure
C_{i}	State space output matrix corresponds to y_{i}
C_{o}	State space output matrix corresponds to y_{o}
D	Feedforward matrix of the state space structure
D_h	State space feedforward matrix corresponds to h
D_u	State space feedforward matrix corresponds to $\bar{u}$
D_{i}	State space feedforward matrix corresponds to y_{i}
D_{o}	State space feedforward matrix corresponds to y_{o}
E	Norm of the residual e over a sliding window

e $\hat{y}_{\mathrm{o}}$ estimation residual

f System nonlinearities

h Output nonlinearities

u System Input

v_i Velocity of the ith autonomous vehicle

w External disturbances

x System state vector

y System Output

y_{i} A subset of the system outputs, which also represents the transmissibility input vector

y_{o} A subset of the system outputs, which also represents the transmissibility output vector

z High-gain transmissibility virtual state vector

Greek Symbols

δ System characteristic equation

Γ_{i} Zeros of the output y_{i} as polynomials of $\mathbf{p}$

Γ_{o} Zeros of the output y_{o} as polynomials of $\mathbf{p}$

λ Recursive least squares identification forgetting factor

$\mathscr{A}$ System state matrix in the discrete time

$\mathscr{B}$ System input matrix in the discrete time

$\mathscr{P}, \mathscr{M}$ Transmissibility-based sliding mode controller gains

$\mathscr{T}$ Transmissibility

μ Fault detection threshold

Θ FIR model structure parameters

$\tilde{y}_{\mathrm{i}}$ Corrupted measurements of y_{i}

$\tilde{y}_{\mathrm{o}}$ Corrupted measurements of y_{o}

Transmissibility-based sliding mode control signal

K Kalman gain

P Kalman estimation covariance

Q $\tilde{y}_{\mathrm{o}}$ Measurements noise covariance

R $\tilde{y}_{\mathrm{o}}$ Measurements noise covariance

Superscripts

d FIR noncausal order

m Number of independent inputs acting on the system

n System order

p Number of independent system outputs

r FIR causal order

Other Symbols

$\hat{\Theta}^{\mathrm{FIR}}_{r,d}$ Identified transmissibility parameters of the FIR model structure

p Continues Time-differentiation Operator

q Forward shifting operator

Acronyms / Abbreviations

adj Matrix adjugate

CAV Connected Autonomous Vehicle

det Matrix determinant

FIR Finite Impulse Response

HGT High-gain Transmissibility

RLS Recursive least squares

V2C Vehicle-to-Cloud

V2V Vehicle-to-Vehicle

Chapter 1

Introduction

The evolution in automation science and its wide implementation in different life disciplinarians are promising a highly automated future. Without any doubt, control systems engineering and control theory play crucial role in the existence of this automated future. This will therefore be reflected in many aspects, including but not limited to, aerospace applications, robotics, and semiconductor manufacturing. Increasing the level of automation promises with lower operating/products costs, higher work efficiency, less work times, ...etc. Lending machines a higher level of automation with all the advantages it carries, however, carries out trade-offs that always rises. The main two challenges arise are: i) More complicated control systems are required, and ii) Safety.

The first step in most modern control systems is signal estimation. Signal estimators are mathematical relationships that implement sets of time-signals recorded during the system operation to estimate other signals. For example, the system's mathematical model can be used along with the input signals to estimate the system outputs. This approach is the most classical output estimation. Another approach is using the input and the measured output signals to estimate the system states, which is widely used and known as *State Observer*. The estimated signals can then be fed into different controllers. Imagine for example a system operating under high temperature where placing inertial sensors is not possible. Signal estimators can be used to estimate the sensors' measurements in this case, in which they are fed back to the controller. This approach is known as *Soft Sensing*.

The second challenge is represented in the safe operation of automated systems. Most automated systems are designed with strict aspects to guarantee safe operation. However, systems might diverge from the designed safe operating conditions to other conditions that can lead to fatal consequences. This divergence is regarded as a system fault. The designed operating conditions are known as *Healthy Conditions*, while any other operating conditions the system diverge to are known as *Faulty Conditions*. Signal estimation is used in this

case to estimate the healthy operating conditions, which is used after for the purpose of fault detection and mitigation. For example, consider a ground vehicle with simple cruise control system. A failure in one of the system components such as the velocity sensor leads to inabilities in maintaining the vehicle desired velocity. Signal estimation can be used to estimate the vehicle response under healthy conditions to detect these faults and maintain the desired velocity.

It is evident that as the technology and complexity of automated systems evolve, more signals are required to be estimated. The availability of some required signals for the estimation such as system's inputs might not be available. Consider for example an aerospace structure, where the excitations (inputs) are resultant of turbulent fluid flow that is difficult to be determined. Another limitation comes from the difficulty modeling some dynamic behaviours such as actuators nonlinearities and ground friction (unknown system nonlinearities and unmodeled dynamics). Moreover, mathematical models are derived while assuming ideal environment, which might be different than the operation environment (external disturbances). These limitations confine the applicability of classical estimators and state observers, which requires new comprehensive estimators that count for unknown inputs, unmodeled dynamics, and external disturbances.

1.1 Transmissibility Operators

Transmissibilities are mathematical relationships between two subsets of outputs in the same system. The inputs and outputs of transmissibilities are both outputs of the underlying system. Transmissibility operators have been used in a variety of applications, including fault detection and output prediction when the dynamics and inputs of the underlying system are unknown. [8, 5, 7, 68, 64]. These operators became extremely important when dealing with systems with distributed inputs. For example, in aerospace structures or structures immersed in fluids where the inputs are a combination of turbulent fluid flow distributed around the structure. For these systems, transmissibilities have high capabilities to detect faults in such systems, as highlighted in [79]. Also, transmissibilities were used in multiagent systems to allow agents to control each other instead of using centralized control algorithms for the entire system, see for example [64]. When dealing with systems with distributed inputs, transmissibilities became extremely important. Transmissibilities have been shown to be the most effective method for detecting faults in these systems, as shown in [85]. Because of their simplicity and ability to identify the modal parameters, frequency-domain transmissibilities are commonly used in the literature [73, 78] [33]. Frequency-domain transmissibilities are simply the ratio of frequency responses of two linear system outputs. The frequency-domain

transmissibilities, on the other hand, were found to be dependent on the excitation signal under nonzero initial conditions [8].

Time-domain transmissibilities were introduced in [8] by using the differentiation operator $\mathbf{p} = \frac{\mathbf{d}}{\mathbf{d}t}$ instead of the Laplace variable s to count for non-zero initial conditions. In [5], least-squares identification was used with noncausal FIR (Finite Impulse Response) models to identify transmissibilities with noncausal and unstable components under unknown dynamics of the underlying system. Identified models of transmissibility operators were also used in [7] to reconstruct the underlying system dynamics from output-only measurements. These studies assumed a linear and time-invariant underlying system. In [68], transmissibilities were applied to systems with bounded unknown nonlinearities by considering the nonlinear terms as independent excitations on the system. This work extends the applicability of transmissibility operators to systems with time-varying parameters.

1.2 Connected Autonomous Vehicle Platoon

Connected autonomous vehicles (CAV) platoons represent a new technology where a network of vehicles communicates together using wireless communication to achieve the desired speed and position of the vehicles in the network. This new technology represents an emerging cyber-physical system (networking, computation, and physical processes) with significant potential to enhance traffic safety, ease congestion, and positively impact the environment through autonomous platoon control.

1.3 Multi-actuator Systems

Recently, the design and control of motion systems with multi-actuators have received considerable efforts and attention from different fields that require high-precision motion control. For example, optical lithography machines include different types of actuators including lorentz and piezoelectric actuators that provide the necessary high-precision motions for microchips fabrication. Lorentz actuators are electromagnetic actuators provide motions within the range of millimetres, while piezoceramic actuators are smart material-based actuators that provide motions within micrometers. For example, due to the severe operating conditions, these actuators may partially or fully lose the ability to follow-up with the desired trajectory, which is known as loss of effectiveness.

1.4 Flexible Structures

Fault detection in flexible beams can be difficult to achieve due to the complexity of their dynamics, and a measurement of the excitation that acts on the beam might not be available. For example, the structures of transportation vehicles that are immersed in a fluid such as an aircraft or an underwater vehicle where the excitation signals on the structure are distributed along the structure. Moreover, these structures are highly subjected to external disturbances such as turbulent fluid flow. The problem that arises here is that it is not possible to measure the level of an individual component's excitation due to the multiple sources of its excitation. This work proposes a solution to this issue by using a technique that assumes unknown excitations and can provide model-free fault detection.

1.5 Dissertation Organization

This dissertation is organized as illustrated in Figure 1.1, and as follows: A literature survey is conducted in Chapter 2. Section 3.1 extends transmissibility operators to a class of nonlinear systems. Section 3.2.1 presents an algorithm to identify transmissibility operators. The obtained transmissibility operators are implemented for fault detection in Section 3.2.2. Next, the transmissibility-based fault detection algorithm is applied to CAV platoons in Section 3.3, detecting drunk drivers in Section 3.4, structural health monitoring in Section 3.5, and actuator fault detection in section 3.6.

Chapter 4 represents transmissibility-based fault mitigation using transmissibility-based sliding mode control. The controller is designed in Section 4.1, and the stability is investigated in Section 4.2. This fault mitigation algorithm is applied to CAV platoons in Section 4.3 and multi-actuator systems in Section 4.4.

Chapter 5 extends transmissibility operators to systems with time-variant dynamics. Section 5.1 derives transmissibility operators for time-variant systems. Section 5.2 introduces a recursive algorithm to identify time-variant transmissibilities. Section 5.3 distinguishes normal dynamic variation from abnormal dynamic variation, allowing fault detection in systems with time-variant dynamics. This technique is applied to connected autonomous robots in Section 5.4, Flexible structure in Section 5.5, robotic manipulators in Section 5.6, and Section 5.7 discusses the superiority of the claimed contributions.

Chapter 6 introduces a new transmissibility-based state estimator called High-gain Transmissibility (HGT) to estimate the system states while the states are fully or partially subjected to unknown nonlinearities. This problem is formulated in Section 6.1 and derived for systems with single nonlinearities in Section 6.2. Section 6.3 shows the relationship between HGT

and high-gain observers. This technique is generalized on systems with multiple unknown nonlinearities in Section 6.4 and verified numerically in Section 6.5.

Chapter 7 incorporates transmissibility operators with a Kalman filter to filter measurement noise in systems subjected to non-Gaussian process noise. This problem is formulated in Section 7.1 and applied to systems with single noisy output to be filtered in Section 7.2. The technique is then generalized to systems with multi-noise outputs and unknown nonlinearities in Section 7.3. Section 7.4 shows the convergence analysis and derives the optimal filtering gain. This approach is tested numerically in Section 7.5, and experimentally on connected autonomous robots in Section 7.6.

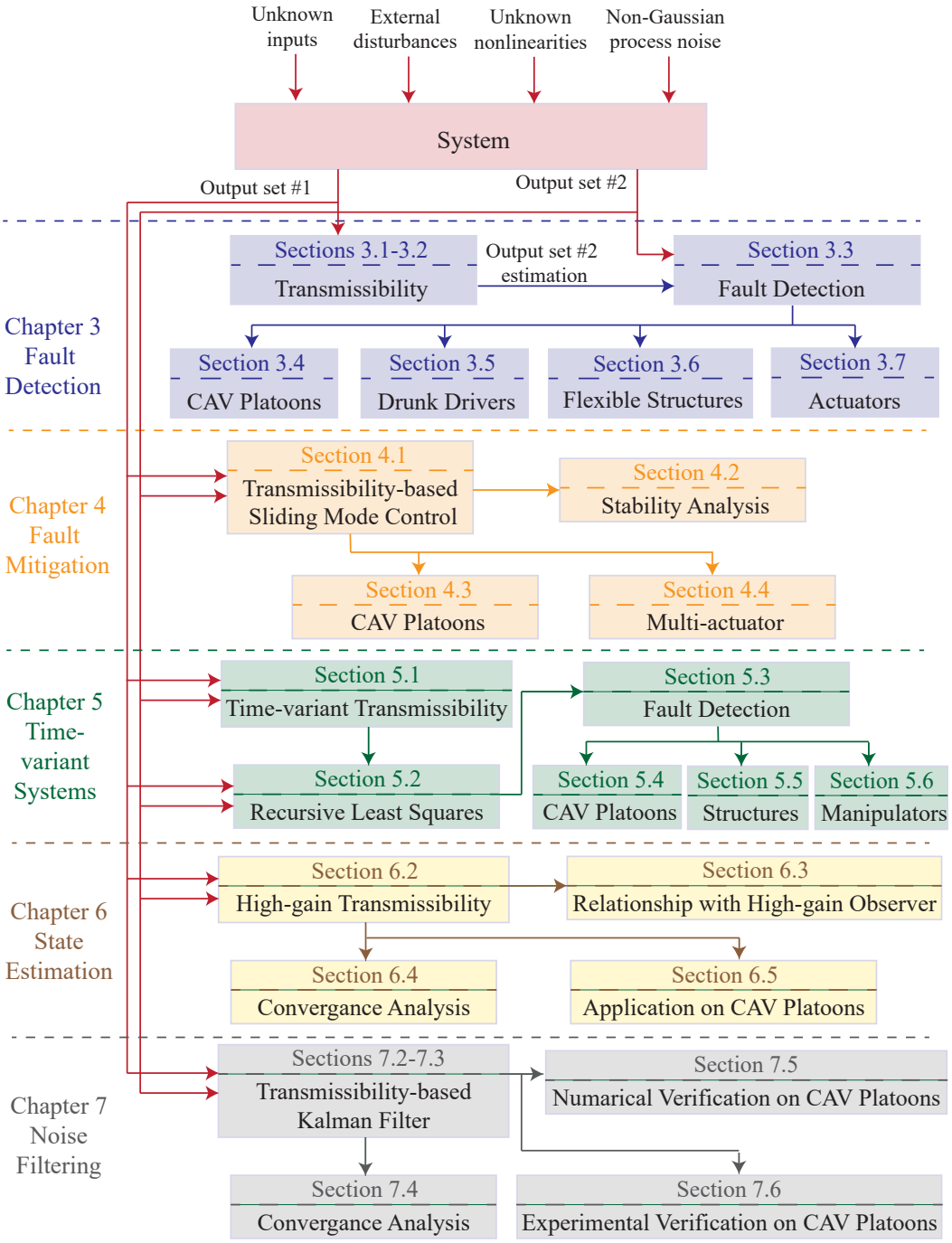

Fig. 1.1 Flow diagram of the work presented in this dissertation. Chapter 3 defines transmissibility operators and implements them in fault detection. Chapter 4 presents fault mitigation. Chapter 5 implements transmissibility to systems with time-variant dynamics. Chapter 6 implements transmissibility in state estimation. And Chapter 7 incorporates transmissibility with Kalman filter in filtering noise.

Chapter 2

Literature Survey

2.1 Soft Sensing and State Observers

Soft sensing is a model-based approach of estimating unmeasured outputs from the inputs. As referred to in [58], soft sensing techniques have some challenges including minimizing the assistance of human experts, such as in the model selection, and filling the gap between the laboratory outcome and the industrial practice. Considering the soft sensing techniques in [58], some of these techniques require building a special hardware for the soft sensor that is used for fault detection [54, 2, 82], where other require knowledge of the excitation signal or the dynamics of the system [129, 10, 34], or some information about the system like the impulse response parameters [35, 45].

System state estimation is the most essential tool in modern control systems. State estimation was referred to as the hottest issue in the field of control in [86]. State observers are mathematical models that use the system inputs along with the measured outputs to estimate the system states. Linear state observers showed superiority in state estimation, see the following survey [140]. Aside from the fact that most state observers require the knowledge of the system input, some difficulties raised when the system is subjected to more nonlinearities. Estimating the states of nonlinear systems with unknown nonlinearities is one of the most challenges in the estimation theory, see for example [24, 145]. Robust state estimators such as high-gain observers showed ability to overcome unknown nonlinearities while the system is on the canonical form, see the survey [70]. In the literature of high-gain observers, the system model is typically reformulated as a chain of integrators, where the first state is always directly measured and all the uncertainties/unknown dynamics are pushed to the last state.

2.2 Fault Detection and Mitigation

Fault detection techniques can be categorized into three categories: model-based techniques, data-driven techniques, and hybrid techniques [14]. Model-based fault detection methods, such as analytical redundancy and observer-based techniques as in [31, 36], can detect actuator faults. However, these methods require knowledge of the actuator input, actuator dynamics, and the underlying dynamics of the system. Data-driven techniques that include methods based on machine learning need an excessive amount of machine learning training [87]. In [72], a data-driven method for fault diagnosis of a multi-functional spoiler system based on signal processing techniques. Hybrid techniques integrate model-based techniques with data-driven techniques. See for example [28] where a particle filter is integrated with recurrent neural networks for the purpose of fault detection in gas turbine engines. These techniques also require knowledge of the actuator input and the underlying dynamics [81, 107].

Model-based techniques have attained the most attention in the literature. These techniques compare available measurements with a model-based estimate of the output. The discrepancy between the measured and estimated outputs is considered a fault indicator. According to [114] most of the model-based techniques use the following: (a) analytical estimation, (b) parity space, (c) parameter estimation, (d) graph-theoretic approaches, and so on. The analytical estimation includes analytical redundancy, observer-based techniques, and filtering techniques. Analytical redundancy is achieved by obtaining an input-output mathematical model of the system, which is used along with the input to obtain an estimate of the output. The difference between the measured and estimated outputs is considered as a health indicator [137]. Observer-based fault detection is widely used, for example, in [23] an adaptive observer is designed to obtain a set of residuals that are used to detect and isolate actuator faults, then an observer is used to estimate the variation in the model parameters. The linear observer theory was developed in [132] to include a class of nonlinear systems for the purpose of fault detection. A two-stage Kalman filter was proposed in [9] to detect and estimate different faults in a quadrotor helicopter. In [13], a nonlinear adaptive estimation technique scheme is introduced for actuator fault detection, isolation, and accommodation. Nevertheless, observer-based techniques require knowledge of the excitation input. Parity space techniques are also model-based techniques that require knowledge of the excitation input. In [52], an integrated parity space method with a recursive least squares algorithm was introduced to detect faults in quadrotor helicopters and estimate their severity.

Parameter estimation techniques represent another class of model-based techniques [114], where the healthy estimated parameters are set as a reference and continuously compared to an online estimation of the same parameters. The discrepancy between the reference values

and the estimated ones obtained is considered as a fault indicator, see for example [116, 57]. Another class of model-based techniques is graph-theoretic approaches, such as bond graphs [114], which model the power propagation within a dynamic system as a schematic graph. Bond graphs merge information from different domains in one complete model due to their causal and structural features that enable to deduce directly a set of fault indicators, see for example [104]. Other techniques use a mixture of a system model and a non-parametric model to detect and isolate actuator faults [122]. The system model is used to isolate the faulty channel, and then the non-parametric model is used to isolate the specific variable in the faulty channel. However, most of the model-based techniques require knowledge of the actuator inputs and the system dynamics.

A class of data-driven techniques is based on machine learning [114]. Supervised approaches define the observations with labels and train a network to classify similar data. Supervised techniques can use Bayesian networks [22, 11, 118] and artificial neural networks [53, 46]. Unsupervised data-driven techniques, which depend on classifying similarity between data sets, include control charts and principal component analysis. Control charts are used to monitor the quality characteristics of a process in order to identify special causes of variability, see for example [130]. Principal component analysis is a multivariate statistical analysis, which depends first on reducing the data dimensionality for easier analysis of the essential data. Then it monitors the maximum variance and the correlation between the process parameters, see for example [143]. Some other data-driven techniques such as that based on multivariate statistical analysis and subspace aided approaches are more suitable for stochastic systems [59]. Such model-free techniques consider a recursive timely update of the system status to overcome the problem of external disturbances. This requires the assumption that the system is healthy during these updates.

2.3 Connected Autonomous Vehicle (CAV) Platoon

Connected autonomous vehicles (CAV) platoons represent a new technology where a network of vehicles communicates together using wireless communication to achieve the desired speed and position of the vehicles in the network.

This new technology represents an emerging cyber-physical system (networking, computation, and physical processes) with significant potential to enhance traffic safety, ease congestion, and positively impact the environment through autonomous platoon control, see for example [55, 16, 106]. The cyber component of such a system incorporates the vehicle-to-vehicle (V2V) and vehicle-to-cloud (V2C) communication networks [27], while the physical component includes physical vehicle dynamics and human-driver responses.

Within CAV, communication networks enable opportunities for greater situational awareness, collaborative decision-making, and improved control[113]. It is evident that as the technology and complexity of connected autonomous vehicles evolve, several grand research challenges need to be addressed. These include securing the connected autonomous vehicles from malicious cyberattacks that can affect the actuators and sensors in the CAV platoon, see for example [61, 76]. Other sources of failures include cyber-physical attacks, faults in sensors and actuators, and unknown nonlinear dynamics in the CAV [105].

Connected autonomous vehicles faults can lead to catastrophic losses [110, 127, 84]. The presence of cyberattacks can lead to faulty sensor measurements, faulty control signals, or delayed control signals that appear as cyber-physical attacks on actuators [61]. Moreover, disturbances can occur in the communication between two vehicles, as in [105]. Furthermore, each system is subjected to system jamming, that is, time delay in one or more of the cyber-physical components of the system [76, 43]. Time delay affects V2V communication and can lead to instability in the control system [76]. Time delay requires a high management level in a way that presents no significant effect on platoon string stability [42]. Therefore, there is a critical need to provide fault mitigation for different uncertainties that may affect the dynamics of the CAV. Since the CAV may include different uncertainties, then it is essential, from a practical point of view, for the fault mitigation technique to be able to perform under unknown dynamics of the CAV.

In CAVs, besides the reported failures within the vehicle such as sensor faults or the vehicle's controller failure as in [76], a wide range of cyber faults might occur. Each vehicle will have the ability to communicate with other vehicles, infrastructure, and the cloud. These communication channels will be open for any CAV to join, which makes it highly vulnerable to cyber-attacks. Moreover, the vulnerability to other communication failures such as communication time-delay and packet loss, see for example [105, 76, 98]. These faults can lead to inaccuracies that will drop the CAVs efficiency, and more importantly, instabilities in the control systems.

The existence of CAV platoons is basically related to the safe transition from on-road human-driven vehicles to CAVs. This means CAVs have to adapt to the surrounding human-driven vehicles and guarantee their safety and security. The main challenge that arises here is the unknown human-drivers behavior that is due to different driving experiences and sudden changes in decisions. However, combining these failures with the human effects threatens the safety of on-road vehicles as well. Therefore, there is a critical need to provide a fault mitigation algorithm to overcome faulty behaviors in CAV platoons. Moreover, since CAV models may include different types of uncertainties, then providing a fault mitigation

algorithm that is independent of the dynamics of the platoon helps in avoiding any faulty behaviors in the fault mitigation algorithm due to modeling errors.

The first generation of CAVs will interact with the current on-road human-driven vehicles. Since the current on-road vehicles are not supplied with adequate technology for communication, CAVs will mainly depend on the onboard perception sensors to supervise their surroundings and safely coexist with the human-driven vehicles. The novel work introduced in [126, 125] showed the fatal consequences that can occur due to sensor faults. Such faults in vehicle platoons can lead to an enormous loss in both lives and costs. This is regarded as the fault degradation over time as explained in [125]. Indeed, in [138] the authors showed the importance of dealing with unknown sensor fault degradation and the necessity for health monitoring techniques that consider unknown fault dynamics. Therefore, it is essential to consider methods that can mitigate different unknown fault dynamics, such as transmissibility-based techniques.

An important issue that always arises when autonomy cooperates with humans is the unknown human effect. More precisely, in mixed platoons the human-driver response is unknown. Some studies have considered estimating the human-driver response such as in [18, 91], however, such methods are not applicable in abnormal driving situations such as careless and novice drivers. Moreover, estimating the human-driver response in mixed platoons depends greatly on the CAVs' perception sensors, and as was shown in [126, 125, 138] sensors are highly subjected to fault degradation. Many other studies considered the estimation of the driver's behavior in human-driven vehicles to remain a challenge [83, 32, 142, 109]. Therefore, the human-driver response is considered as unknown bounded nonlinearities within the platoon, and the proposed health monitoring technique is developed to be independent of the human-driver response.

Adapting autonomous vehicles with human-driven vehicles greatly depends on the perception sensors on the autonomous vehicles. For example, in [47], an algorithm is introduced to control mixed autonomous and human-driven platoons to harmonize traffic, improve fuel-efficiency and reduce environmental impacts. A novel algorithm is introduced in [123] to control mixed autonomous and human-driven platoons using deep reinforcement learning. This algorithm assumes the resulting policies and emergent behaviors in mixed-autonomy traffic to provide insight into the traffic through mixed platoons. However, these algorithms mainly depend on CAVs to measure different information about human-driven vehicles and share them through the V2V communication links. CAV failures will limit the availability of useful information about human-driven vehicles, and therefore the failure of these control algorithms. In this work, we aim to recover the healthy behaviour of the mixed platoon so the designated control algorithms such as the ones introduced in [47, 123] are effective again.

Many studies in the literature investigated the risk that can be carried by CAVs faults in mixed autonomous and human-driven platoons. The study introduced in [17] shows that supplying autonomous vehicles with cyber components increases the risk of the human-driven vehicles significantly due to increasing the range of possible technological failures. That is, in addition to the faults in the physical components of the current autonomous vehicles, adding the cyber components will carry out more possible faults, and thus, higher risk on the human-driven vehicles. The study in [133] proposed CAVs as a safety line for human-driven vehicles. In such architectures, a failure in CAVs will directly impact the safety of human-driven vehicles, which necessitate a health monitoring system for mixed platoons. The study in [92] argues about the ethical aspects of increasing the on-road automation without taking the autonomous vehicles' faults into consideration.

2.4 Multi-actuator Systems Health Monitoring

Recently, the design and control of motion systems with multi-actuators have received considerable efforts and attention from different fields that require high-precision motion control, see for example [93, 49]. For example, optical lithography machines include different types of actuators including lorentz and piezoelectric actuators that provide the necessary high-precision motions for microchips fabrication. Lorentz actuators are electromagnetic actuators provide motions within the range of millimetres, while piezoceramic actuators are smart material-based actuators that provide motions within micromenetarsi. For example, due to the severe operating conditions, these actuators may partially or fully lose the ability to follow-up with the desired trajectory, which is known as loss of effectiveness [112]. Another example in [100] where two dual stage actuators drive hard disk drivers, each comprising of a voice coil motor actuator and a piezoelectric micro actuator operating on the same pivot point. Both dual stages operate independently, however, the control forces and torques generated by one affect the operation of the other. That is, the operation of each of them affects the other with unknown disturbances, which can considered as unknown excitations. A similar application was introduced in [15] for a multi-actuator hydraulic system, where a second actuator is required to reject the disturbances from the first actuator due to throttling losses. Therefore, due to the wide range of possible actuator faults and different actuator models, it is required to develop a fault detection technique that can capture different types of faults in different types of actuators.

Some studies introduced in the literature specified the problem of fault detection in applications with multi-actuators. In [75], sliding mode control is used to fault-tolerant control actuator faults in quadcopters with multi-actuators. This method requires the knowledge of

the input signal and is not robust against external disturbances.In [101], cracks in piezoelectric beams are detected through monitoring the natural frequencies. An assumption is made in [101] that the cracks are always assumed to reduce the natural frequencies of the piezoelectric beam. Comparing to the proposed method, transmissibility-based fault detection can detect different fault classes and unknown fault dynamics. In [51], an observer-based fault tolerant control algorithm is introduced for actuator faults. This method not only requires the knowledge of the input signals and the system dynamics, assumptions are also made regarding input constraints in order to monitor the actuator health. In [120], the aircraft states are modeled as hybrid states, then a modified observer-based health monitoring technique is proposed for the aircraft actuators. Besides the required knowledge of the system inputs for the observer, the knowledge of the switching mechanism is required and must be fed back to the observer.

Transmissibility operators have been improved over the recent years, and have become one of the most beneficial output estimators while the system inputs are unknown, see for example [8]. In recent years, transmissibilities have been improved significantly, and the applicability range was developed. Time-domain transmissibilities were introduced in [8] by implementing the time differentiation operator $\mathbf{p} = \frac{\mathbf{d}}{\mathbf{d}t}$ instead of the Laplace complex variable s to count for non-zero initial conditions. In [5], least-squares identification using noncausal FIR models was introduced for transmissibilities to count for noncausal transmissibilities, unknown underlying dynamics, and unstable transmissibility operators. The identified models of the transmissibility operators are then used in [7] to reconstruct the original system dynamics. All the studies mentioned earlier considered the original system to be linear.

On the application side, transmissibilities showed exceptional fault detection abilities in systems subjected to distributed unknown inputs. This includes aerospace structures that are immersed in turbulent fluid flow. This is highlighted in the literature survey in [79]. Another class of systems that showed the importance of transmissibilities is systems multi-agent systems where each agent adapts to its surroundings while staying within the system. The inputs used within an agent for the adaptation are most likely not to be shared with other agents, and only sensor measurements are shared. Transmissibilities were used in multiagent systems to allow agents to control each other instead of using centralized control algorithms for the entire systems, see for example [64, 67].

2.5 Structural Health Monitoring

Monitoring the health of flexible structures arises with the severe operating conditions that some industrial applications are subjected to. A wide range of fault detection techniques

introduced in the literature, including model-based techniques such as observer-based [80, 144], data-driven techniques such as techniques based on signal processing [60], and hybrid techniques [28, 81]. However, the problem of fault localization within the structure remains a challenge that becomes harder in large structures such as aerospace applications and wind turbines. This challenge becomes harder if the faults are internal and don't appear on the structure surface. Commonly, non-destructive tests (NDT) are used to localize faults and cracks in flexible structures. For example, in [134] ultrasonic waves were used to detect weak bonds in composite-adhesive bonded structures. In [108], pulsed thermography was used to estimate the thickness in fiber-reinforced composites. Infrared thermography testing was used in [37] to estimate the corrosion defect characterization. In [30], radiographic testing was used to detect and localize faults in low-carbon steel welded joints. In [139], DC electromagnetic testing based on the drag effect was used to detect and characterize cracks in high-speed moving ferromagnetic material. In [19], acoustic emission testing was used to detect and localize material damages in glass fiber-reinforced plastics. However, non-destructive tests require additional hardware, comprise human efforts to conduct the test, and in most cases, require stopping the system operation till the test is done. This results in a high cost of localizing faults in flexible structures.

The problem of fault and damage localization in flexible structures based on the dynamic behaviour was investigated through some previous studies. In [71, 90], a frequency-based damage detection and localization algorithms in flexible structures were proposed based on the natural frequencies shifting. Apart from the fact that not all faults can be detected based on the natural frequency shift, this technique requires the knowledge of the fault dynamics. In [1], vibration measurements were used along with dynamic models to localize faults. Similarly to [71, 90], this technique requires the knowledge of the fault dynamics, limited robustness against external disturbances, and accurate dynamic models. In [38], the frequency domain analysis along with the vibration measurements were aided with finite element models. This approach requires accurate dynamic models and the knowledge of the fault dynamics as well. In [117], a fault localization technique was introduced by identifying the stiffness, and then based on the stiffness degradation the faults are detected and localized. However, this technique requires knowledge of all excitations, sensitive to measurements noise, and known fault dynamics.

Another set of common fault localization techniques was introduced in the literature to localize faults in systems without physical connections. For example, in [94], a set of H_∞ filters were designed to detect and isolate faulty sensors. The key in such techniques is the fact that the output of the faulty sensor doesn't have a physical connection with the structure. The best way to observe the difference here is by following the energy propagation within the

structure. External excitations supply the structure with kinetic energy, in which its delivered and propagated to the sensors. However, sensors won't supply the structure back with any energy. A fault in the structure will have effects on all sensors, since the structure propagate energy to all sensors. However, a fault in one of the sensors won't affect the structure or other sensors, thus localizing the fault is possible using such methods. Note that even if the sensor measurements are used to control the structure, only the measurements' information will be delivered to the controller but no energy will be propagated from the sensor back to the structure. See other similar sensor fault localization and isolation in [128, 44, 121, 12].

2.6 Robotic Manipulators Fault Detection

The main challenge in fault detection in robotic manipulators is the unknown parameter variation. Observer-based techniques such as in [21] require the knowledge of the manipulator inputs, knowledge of the parameter variations, and known nonlinearities. The knowledge of the parameter variations highly limits the use of residual-based techniques, since the residual can't be distinguished if its due to parameter variation or system fault. Most techniques consider a sensor to measure the parameter variation and feed it back to the detection algorithm. Some work has been introduced to solve this problem as in [25] where neural networks are used to aid the adaptive algorithm, which adds more complexity and cost to the detection approach. Machine learning techniques such in [39] require intense models training. For example, in [26] data from more than 5000 robotic manipulators are used to detect faults.

2.7 Transmissibility Before This Thesis

This section presents the basic concept of transmissibility in its classical form that was established before this thesis. All work on transmissibility operators before this thesis was limited to linear systems only [102, 8, 3, 85]. Mainly, this thesis extends transmissibility operators to a class of nonlinear systems and different robotic applications.

2.7.1 Single-input Single-output Frequency-domain Transmissibility

Consider the following single-input two-outputs state space system

$$\dot{x}(t) = Ax(t) + Bu(t), \tag{2.1}$$

$$y(t) = Cx(t) + Du(t), \tag{2.2}$$

where $u \in \mathbb{R}$ and $y \in \mathbb{R}^2$, $A \in \mathbb{R}^{n\times n}, B \in \mathbb{R}^n, C \in \mathbb{R}^{2\times n}$, and $D \in \mathbb{R}^2$. Define the two outputs such as

$$y(t) = \begin{bmatrix} y_1(t) \\ y_2(t) \end{bmatrix}, \tag{2.3}$$

where

$$y_1(t) = C_1 x(t) + D_1 u(t) \in \mathbb{R}, \tag{2.4}$$
$$y_2(t) = C_2 x(t) + D_2 u(t) \in \mathbb{R}. \tag{2.5}$$

Assume zero initial conditions and obtain the transfer functions from u to y_1, and from u to y_2

$$\frac{Y_1(s)}{U(s)} = \frac{C_1 \text{adj}(sI-A)B + D_1}{\det(sI-A)} = \frac{s^n a_{y1,n} + \cdots + s a_{y1,1} + a_{y1,0}}{s^n b_n + \cdots + s b_1 + b_0}, \tag{2.6}$$
$$\frac{Y_2(s)}{U(s)} = \frac{C_1 \text{adj}(sI-A)B + D_1}{\det(sI-A)} = \frac{s^n a_{y2,n} + \cdots + s a_{y2,1} + a_{y2,0}}{s^n b_n + \cdots + s b_1 + b_0}, \tag{2.7}$$

where $U, Y1, Y2$ are $u, y1, y2$ in the frequency domain. Notice that since both transfer functions share the same input u, then both transfer functions have the same denominator (characteristic equation). Dividing (2.7) on (2.6) yields

$$\frac{Y_2(s)}{Y_1(s)} = \frac{C_2 \text{adj}(sI-A)B + D_2}{C_1 \text{adj}(sI-A)B + D_1} = \frac{s^n a_{y2,n} + \cdots + s a_{y2,1} + a_{y2,0}}{s^n a_{y1,n} + \cdots + s a_{y1,1} + a_{y1,0}}, \tag{2.8}$$

which is called the frequency-domain transmissibility operator from the output y_1 to the output y_2. Notice that the shared input u was cancelled along with the shared denominator. The importance of transmissibility operators is represented in the cancellation of the system input u. This gives the ability to estimate y_2 from y_1 only while the system input u is unknown.

2.7.2 Multi-input Multi-output Frequency-domain Transmissibility

Transmissibility operators started appearing for systems with multi degrees-of-freedom around two decades ago [102, 85]. Consider the state space system in (2.1)-(2.2) with $u \in \mathbb{R}^m$ and $y \in \mathbb{R}^p$, m is the number of independent inputs, and $p > 1$ is the number of sensor

measurements, and split the output y into the two output subsets

$$y_{\mathrm{i}}(t)=C_{\mathrm{i}}x(t)+D_{\mathrm{i}}u(t)\in\mathbb{R}^{m}, \tag{2.9}$$

$$y_{\mathrm{o}}(t)=C_{\mathrm{o}}x(t)+D_{\mathrm{o}}u(t)\in\mathbb{R}^{p-m}, \tag{2.10}$$

where $C_{\mathrm{i}}\in\mathbb{R}^{m\times n}, C_{\mathrm{o}}\in\mathbb{R}^{(p-m)\times n}, D_{\mathrm{i}}\in\mathbb{R}^{m\times m}$, and $D_{\mathrm{o}}\in\mathbb{R}^{(p-m)\times m}$, and

$$C=\begin{bmatrix} C_{\mathrm{i}} \\ C_{\mathrm{o}} \end{bmatrix}, \quad D=\begin{bmatrix} D_{\mathrm{i}} \\ D_{\mathrm{o}} \end{bmatrix}. \tag{2.11}$$

Then transmissibility operator from the output subset y_{i} to the output subset y_{o} satisfies [102]

$$Y_{\mathrm{o}}(s)=\mathscr{T}(s)Y_{\mathrm{i}}(s), \tag{2.12}$$

where $Y_{\mathrm{i}}, Y_{\mathrm{o}}$ are $y_{\mathrm{i}}, y_{\mathrm{o}}$ in the frequency domain. The matrix $\mathscr{T}$ is the transmissibility matrix, in which each entry is a ratio between two numerators similar to equation (2.8) and is given by

$$\mathscr{T}(s)\stackrel{\Delta}{=}\Gamma_{\mathrm{o}}(s)\Gamma_{\mathrm{i}}^{-1}(s), \tag{2.13}$$

and

$$\Gamma_{\mathrm{i}}(s)=C_{\mathrm{i}}\mathrm{adj}(sI-A)B+D_{\mathrm{i}}\delta(s), \tag{2.14}$$

$$\Gamma_{\mathrm{o}}(s)=C_{\mathrm{o}}\mathrm{adj}(sI-A)B+D_{\mathrm{o}}\delta(s), \tag{2.15}$$

$$\delta(s)=\det(sI-A). \tag{2.16}$$

where adj is the matrix adjugate.

2.7.3 Time-domain Transmissibilities

Transmissibilities are developed in the time-domain to count for nonzero initial conditions in [8]. For the system (2.1)-(2.2) with $u\in\mathbb{R}^{m}, y\in\mathbb{R}^{p}$, the transmissibility operator from the output y_{i} to the output y_{o} in the time domain

$$y_{\mathrm{o}}(t)=\mathscr{T}(\mathbf{p})y_{\mathrm{i}}(t), \tag{2.17}$$

where $\mathbf{p} = \frac{\mathbf{d}}{\mathbf{d}t}$ is the time differentiation operator. Note that $\mathbf{p} = s$ under zero initial conditions. Similarly

$$\mathscr{T}(\mathbf{p}) \stackrel{\Delta}{=} \Gamma_{\mathrm{o}}(\mathbf{p})\Gamma_{\mathrm{i}}^{-1}(\mathbf{p}), \tag{2.18}$$

and

$$\Gamma_{\mathrm{i}}(\mathbf{p}) \stackrel{\Delta}{=} C_{\mathrm{i}}\mathrm{adj}(\mathbf{p}I - A)B + D_{\mathrm{i}}\delta(\mathbf{p}), \tag{2.19}$$

$$\Gamma_{\mathrm{o}}(\mathbf{p}) \stackrel{\Delta}{=} C_{\mathrm{o}}\mathrm{adj}(\mathbf{p}I - A)B + D_{\mathrm{o}}\delta(\mathbf{p}), \tag{2.20}$$

$$\delta(\mathbf{p}) \stackrel{\Delta}{=} \det(\mathbf{p}I - A). \tag{2.21}$$

Chapter 3

Transmissibility Operators

3.1 Transmissibility Operators for Smooth Nonlinear Systems

Consider the following smooth nonlinear system

$$\dot{x}(t) = Ax(t) + B_u\bar{u}(t) + B_f f(t,x) + B_w w(t), \tag{3.1}$$
$$y(t) = Cx(t) + D_u\bar{u}(t), \tag{3.2}$$

where $\bar{u} \in \mathbb{R}^{(m-2)}$ is the system input, $f \in \mathbb{R}$ is an unknown bounded nonlinear function, $w \in \mathbb{R}$ is external disturbances, $y \in \mathbb{R}^p$ is the system output, m is the number of independent excitations on the system, and $p > 1$ is the number of sensor measurements, $A \in \mathbb{R}^{n\times n}, B_u \in \mathbb{R}^{n\times(m-2)}, B_f \in \mathbb{R}^n, B_w \in \mathbb{R}^n, C \in \mathbb{R}^{p\times n}$, and $D_u \in \mathbb{R}^{p\times(m-2)}$. Redefine the input vector u to render f and w independent excitations on the system

$$u(t) = \begin{bmatrix} \bar{u}(t) & f(t,x) & w(t) \end{bmatrix}^{\mathrm{T}}.$$

The input and feed-forward matrices then become

$$B = \begin{bmatrix} B_u & B_f & B_w \end{bmatrix} \in \mathbb{R}^{n\times m},$$
$$D = \begin{bmatrix} D_u & 0 & 0 \end{bmatrix} \in \mathbb{R}^{p\times m}.$$

Next, define

$$y_{\mathrm{i}}(t) \triangleq C_{\mathrm{i}}x(t) + D_{\mathrm{i}}u(t) \in \mathbb{R}^m, \tag{3.3}$$

$$y_{\mathrm{o}}(t) \triangleq C_{\mathrm{o}}x(t) + D_{\mathrm{o}}u(t) \in \mathbb{R}^{p-m}, \tag{3.4}$$

where $C_{\mathrm{i}} \in \mathbb{R}^{m\times n}, C_{\mathrm{o}} \in \mathbb{R}^{(p-m)\times n}, D_{\mathrm{i}} \in \mathbb{R}^{m\times m}$, and $D_{\mathrm{o}} \in \mathbb{R}^{(p-m)\times m}$, and

$$C = \begin{bmatrix} C_{\mathrm{i}} \\ C_{\mathrm{o}} \end{bmatrix}, \quad D = \begin{bmatrix} D_{\mathrm{i}} \\ D_{\mathrm{o}} \end{bmatrix}. \tag{3.5}$$

The transmissibility whose pseudo input is y_{i} and whose pseudo output is y_{o}, satisfies [8]

$$y_{\mathrm{o}}(t) = \mathscr{T}(\mathbf{p})y_{\mathrm{i}}(t), \tag{3.6}$$

where $\mathbf{p} = \frac{\mathbf{d}}{\mathbf{d}t}$ is the time differentiation operator. Note that $\mathbf{p} = s$ under zero initial conditions. Moreover,

$$\mathscr{T}(\mathbf{p}) \triangleq \Gamma_{\mathrm{o}}(\mathbf{p})\Gamma_{\mathrm{i}}^{-1}(\mathbf{p}), \tag{3.7}$$

and

$$\Gamma_{\mathrm{i}}(\mathbf{p}) \triangleq C_{\mathrm{i}}\mathrm{adj}(\mathbf{p}I - A)B + D_{\mathrm{i}}\delta(\mathbf{p}), \tag{3.8}$$

$$\Gamma_{\mathrm{o}}(\mathbf{p}) \triangleq C_{\mathrm{o}}\mathrm{adj}(\mathbf{p}I - A)B + D_{\mathrm{o}}\delta(\mathbf{p}), \tag{3.9}$$

$$\delta(\mathbf{p}) \triangleq \det(\mathbf{p}I - A). \tag{3.10}$$

Note that (3.35) can be interpreted as the differential equation

$$\det\Gamma_{\mathrm{i}}(\mathbf{p})y_{\mathrm{o}}(t) = \Gamma_{\mathrm{o}}(\mathbf{p})\mathrm{adj}\,\Gamma_{\mathrm{i}}(\mathbf{p})y_{\mathrm{i}}(t), \tag{3.11}$$

where $\mathrm{adj}\,\Gamma_{\mathrm{i}}$ denotes the adjugate matrix of Γ_{i}. Notice from (3.11) that the relationship between the two output sets y_{i} and y_{o} is independent on the system inputs u.

An estimation of the output y_{o} can be estimated from the transmissibility operator $\mathscr{T}$ along with the measurements of y_{i} from equation (3.35) such that

$$\hat{y}_{\mathrm{o}}(t) = \mathscr{T}(\mathbf{p})y_{\mathrm{i}}(t), \tag{3.12}$$

where $\hat{y}_{\mathrm{o}}$ is the estimation of y_{o}. Since sensor measurements are in discrete time, the measured and estimated outputs are considered in the discrete time domain. Define the residual in

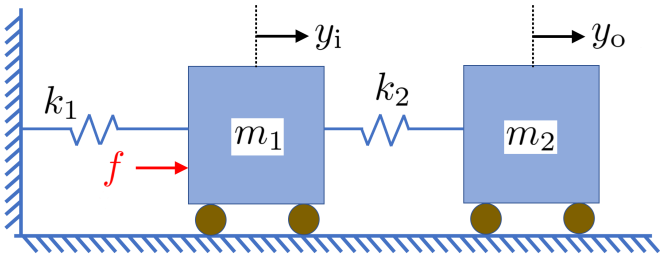

Fig. 3.1 Example 3.1.1: Two consecutive mass-spring system with two outputs y_i, y_o and under unknown nonlinearities f. This example is presented to show the independence of the transmissibility from f.

discrete time

$$e(k) = y_o(k) - \hat{y}_o(k), \tag{3.13}$$

Next, for all $k \geq 0$, compute

$$E(k,w) \triangleq \sqrt{\sum_{i=k}^{w+k} \|e(i)\|}, \tag{3.14}$$

which is the norm of the residual over a sliding window of size w steps.

To explain the formulation further, the following example shows how $\mathscr{T}$ can be constructed in an independent form of f, and then converted from the **p** operator to a chain of integrators.

Example 3.1.1 *In this example, we consider deriving the transmissibility operator between the displacements y_i and y_o of the system shown in Figure A.2 that is under the unknown nonlinearities f. The system can be modeled as in* (A.10) *where*

$$A = \begin{bmatrix} 0 & 0 & 1 & 0 \\ 0 & 0 & 0 & 1 \\ \frac{-(k_2+k_1)}{m_1} & \frac{k_2}{m_1} & 0 & 0 \\ \frac{k_2}{m_2} & \frac{-k_2}{m_2} & 0 & 0 \end{bmatrix},$$

$$B = \begin{bmatrix} 0 & 0 & \frac{1}{m_1} & 0 \end{bmatrix}^{\mathrm{T}},$$

Next, the two displacements y_{i} and y_{o} can be written in the form (6.3)-(5.4) *such that*

$$y_{\mathrm{i}}(t) = C_{\mathrm{i}}x(t) = \begin{bmatrix} 1 & 0 & 0 & 0 \end{bmatrix} x(t), \tag{3.15}$$

$$y_{\mathrm{o}}(t) = C_{\mathrm{o}}x(t) = \begin{bmatrix} 0 & 1 & 0 & 0 \end{bmatrix} x(t). \tag{3.16}$$

Then define

$$\Gamma_{\mathrm{i}}(\mathbf{p}) \triangleq C_{\mathrm{i}}\mathrm{adj}(\mathbf{p}I - A)B = \frac{m_2\mathbf{p}^2 + k_2}{m_1 m_2}, \tag{3.17}$$

$$\Gamma_{\mathrm{o}}(\mathbf{p}) \triangleq C_{x_p}\mathrm{adj}(\mathbf{p}I - A)B = \frac{k_2}{m_1 m_2}. \tag{3.18}$$

Accordingly, the transmissibility operator from the output y_{i} to the output y_{o} while the system is under the nonlinear dynamics f is

$$\mathscr{T}(\mathbf{p}) = \frac{\Gamma_{\mathrm{o}}(\mathbf{p})}{\Gamma_{\mathrm{i}}(\mathbf{p})} = \frac{k_2}{m_2\mathbf{p}^2 + k_2}. \tag{3.19}$$

3.2 Transmissibility Identification and Fault Detection

Notice from (3.35) that if the output channel y_{o} has more zeros than the output channel y_{i}, then the transmissibility operator $\mathscr{T}$ is noncausal. Moreover, if y_{i} has a nonminimum phase zero, then $\mathscr{T}$ is unstable despite the fact that the measurements of y_{o} are bounded due to the system stability. To this end, we consider identifying $\mathscr{T}$ in the structure of noncausal FIR models since they are always stable and can capture the noncausal part.

3.2.1 Transmissibility Identification

Since sensor measurements are obtained in discrete time, we replace $\mathbf{p}$ in (3.36) by the forward shift operator $\mathbf{q}$ [89]. Accordingly, we consider identifying $\mathscr{T}$ in the $\mathbf{q}$ domain [6]. A noncausal FIR model of $\mathscr{T}$ is given by

$$\mathscr{T}(\mathbf{q}) = \sum_{j=-d}^{r} H_j \mathbf{q}^{-j}, \tag{3.20}$$

where r,d denote the order of the causal and noncausal parts of the FIR model of $\mathscr{T}$, respectively, and $H_j \in \mathbb{R}^{1\times m}$ is the jth coefficient of the transmissibility operator $\mathscr{T}$. Let $\Theta = [H_{-d}, \ldots, H_r]^{\mathrm{T}}$, then assume the system to be under healthy conditions for ε steps, then

the least squares estimate of the transmissibility parameters Θ is given by

$$\hat{\Theta} = (\Phi\Phi^{\mathrm{T}})^{-1}\Phi\Psi, \tag{3.21}$$

$$\Psi = \begin{pmatrix} y_{\mathrm{o}}(r) & \cdots & y_{\mathrm{o}}(\varepsilon - d) \end{pmatrix}^{\mathrm{T}}, \tag{3.22}$$

$$\Phi = \begin{pmatrix} \phi(r) & \cdots & \phi(\varepsilon - d) \end{pmatrix}, \tag{3.23}$$

$$\phi(k) = \begin{pmatrix} y_{\mathrm{i}}(k+d) & \cdots & y_{\mathrm{i}}(k-r) \end{pmatrix}^{\mathrm{T}}. \tag{3.24}$$

3.2.2 Fault Detection

Once $\mathscr{T}$ is constructed, either by the derivation in (3.36) or the identification in (3.21), $\mathscr{T}$ can be used along with the measurements of y_{i} to obtain an estimation of y_{o}. Assume the more general case where $\mathscr{T}$ is identified using (3.21), an estimation of the output subset y_{o} can be given at time step k as

$$\begin{aligned} \hat{y}_{\mathrm{o}}(k) &= \mathscr{T}(\mathbf{q})y_{\mathrm{i}}(k) \\ &= \sum_{i=-d}^{r} \hat{H}_i y_{\mathrm{i}}(k-i), \end{aligned} \tag{3.25}$$

where $\hat{\Theta} = [\hat{H}_{-d}, \ldots, \hat{H}_r]^{\mathrm{T}}$. A high level of discrepancies between the measured output y_{o} and its estimation $\hat{y}_{\mathrm{o}}$ can be regarded as fault. Define the estimation residual at time step k

$$e(k) = y_{\mathrm{o}}(k) - \hat{y}_{\mathrm{o}}(k). \tag{3.26}$$

To avoid false alarms, we compute the norm of residual over a sliding window with width W steps for all $k \geq 0$

$$E(k,W) \triangleq \sqrt{\sum_{i=k}^{W+k} \|e(i)\|}. \tag{3.27}$$

Assume $\varepsilon \geq W + d$ and let η be the signal-to-noise ratio, then define the fault detection threshold

$$\mu(W,\varepsilon) \triangleq \frac{\eta}{\varepsilon + 1} \sum_{i=d}^{\varepsilon} E(i,W). \tag{3.28}$$

Operator	Pseudo Inputs	Pseudo Output
$\mathscr{T}_0$	$\{v_5^1, v_5^2, \ldots, v_5^{m-1}\}$	v_5^m
$\mathscr{T}_j$	$\{v_5^1, v_5^2, \ldots, v_5^{m-1}\} \setminus \{v_5^j\}$	v_5^m
$\mathscr{T}_m$	$\{v_5^1, v_5^2, \ldots, v_5^{m-2}\}$	v_5^{m-1}
$\mathscr{T}_{\tilde{j}}^i$	$v_{i-1}^{\tilde{j}}$	$v_i^{\tilde{j}}$

Table 3.1 Transmissibility operators $\mathscr{T}_0, \ldots, \mathscr{T}_m$ are used to detect and localize the faulty platoon in the set of platoons. Next, the transmissibility operators $\mathscr{T}_{\tilde{j}}^i$, where $i = 2, \ldots, 5$ are used to localize the faulty vehicle in the faulty platoon $\tilde{j}$. These transmissibilities are used in Algorithm 1.

3.3 Experiment 1: CAV Platoons Health Monitoring

To ensure that the detected fault is in the structure not the sensor and to localize the faulty sensor, we consider identifying multiple transmissibilities along the set of platoons. All transmissibilities that use the faulty velocity as pseudo input/output will result in high level of the norm of residual. For further explanation on how to localize the faulty vehicle, consider a system of m platoons each with n vehicles, then for all $j = 1, \ldots, m-1$, let $\mathscr{T}_j$ denote a transmissibility operator that relates the velocities of the fifth vehicle in each platoon as defined in Table II that considers a set of m platoons. Moreover, $\mathscr{T}_0$ and $\mathscr{T}_m$ are as defined in Table 3.1. Using Algorithm 1 and Table II, the location of the fault can be determined. If $\mathscr{T}_0$ is faulty and $\mathscr{T}_j$ is healthy then platoon j is faulty. Next, to localize the faulty vehicle, let $\tilde{j}$ denote the number of the faulty platoon, and $\mathscr{T}_{\tilde{j}}^i$ denote the transmissibility from v_{i-1} to v_i in in platoon $\tilde{j}$. If $\mathscr{T}_{\tilde{j}}^i$ is faulty, then vehicle i in platoon $\tilde{j}$ is faulty.

Next, to mitigate faults in vehicle i in platoon $\tilde{j}$, we replace the faulty velocity signal $\tilde{v}_i^{\tilde{j}}$ with the estimated healthy signal obtained from the transmissibility operator $\mathscr{T}_{\tilde{j}}^i$. Note that since $\mathscr{T}_{\tilde{j}}^i$ represents a reflect of vehicle i dynamics, the causal assumption for $\mathscr{T}_{\tilde{j}}^i$ is possible. The correction signal can be obtained for all $k \geq 0$ as

$$v_{i,\text{mit}}(k|\hat{\Theta}_{r,d,\ell}^{\text{FIR}}) \triangleq \begin{cases} v_i(k), & k < \hat{k}, \\ \hat{v}_i(k|\hat{\Theta}_{r,d,\ell}^{\text{FIR}}), & k \geq \hat{k}, \end{cases} \tag{3.29}$$

where $\hat{k}$ is the time sample at which we start using the fault mitigation algorithm, $\hat{v}_i$ is obtained using the transmissibility operator $\mathscr{T}_{\tilde{j}}^i$ along with v_{i-1}. The correction signal $v_{i,\text{mit}}$ replaces the faulty velocity measurement of vehicle i in platoon $\tilde{j}$ and thus is used as a reference for vehicle $i+1$ as shown in Figure 3.2.

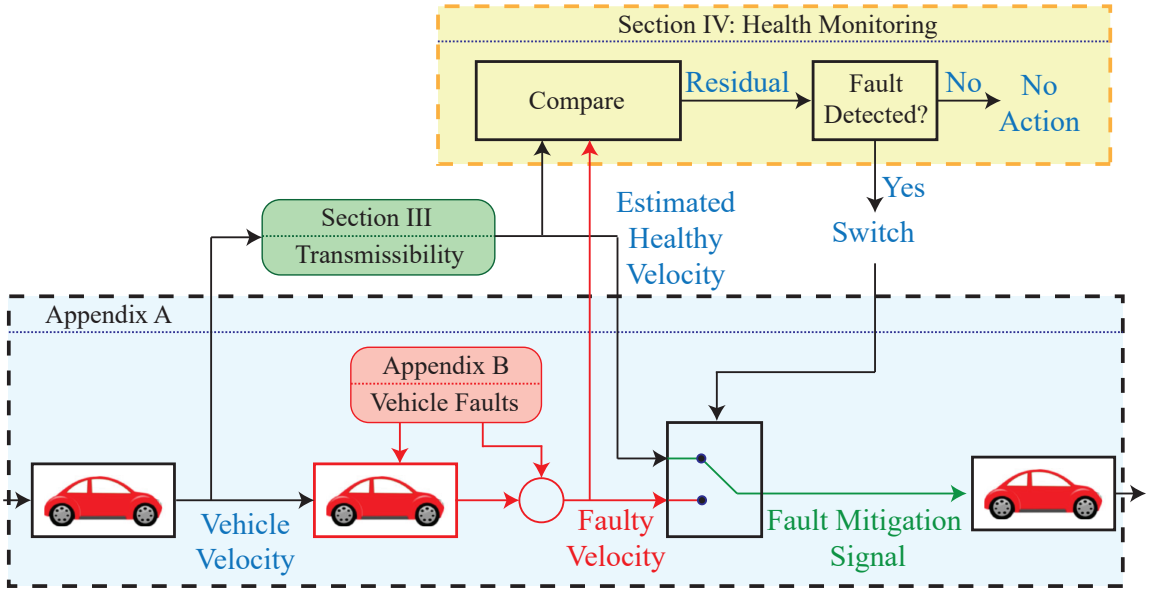

Fig. 3.2 Block diagram for the proposed transmissibility-based fault mitigation algorithm on a three vehicles platoon portion. The platoon is operating under unknown driving conditions and variable velocities. The middle vehicle is faulty. The velocity of the front vehicle is used in the transmissibility to obtain the estimated healthy velocity. Then comparing the measured and estimated velocities gives a fault indicator. If the fault is detected, then the measured velocity is replaced with the estimated one to mitigate the faults effect transmitted to the next vehicle.

3.3.1 Simulation Example

Consider four platoons, each with five identical vehicles with the parameters shown in Table A.2. We model the platoons using the bond graph approach as shown in Appendix A.1. To identify the transmissibility operators defined in Table 3.1 with $m = 4$ and $n = 5$, we set the desired velocities of the platoons to Gaussian white noise with zero mean and unit variance. Algorithm 1 is then used to detect and localize the fault based on the change in the level of the residuals of the identified transmissibilities.

Figure 5.11 shows the estimated Markov parameters of $\mathscr{T}_0$ from each pseudo input to the pseudo output obtained under healthy conditions. Then, the estimated transmissibility $\mathscr{T}_0$ is used with the measurements of v_5^1, v_5^2, and v_5^3 to obtain an estimate of v_5^4. Figure 3.4 shows a plot of v_5^4 and the estimate of v_5^4, which are close to each other.

Next, we introduce the motor disturbances, motor delay, burst transmission, and DoS faults to the system separately as introduced in Appendix B.1. To emulate the motor disturbance fault, a band-limited white noise is added to the motor constant of the third vehicle in the second platoon. To emulate a motor delay, a 1-second delay is introduced to

if $\mathscr{T}_0$ is healthy **then**
  All platoons are healthy;
else
  if $\mathscr{T}_j$ is healthy, where $j = 1, \ldots, m$, **then**
    Platoon j is Faulty;
    Set $\tilde{j} = j$;
  end
  if $\mathscr{T}_{\tilde{j}}^{i}$ is faulty, where $i = 2, \ldots, n$, **then**
    Vehicle i in platoon $\tilde{j}$ is faulty;
  else
    Vehicle 1 in platoon $\tilde{j}$ is faulty;
  end
end

Algorithm 1: Fault localization algorithm for a set of m platoons, each with n autonomous vehicles.

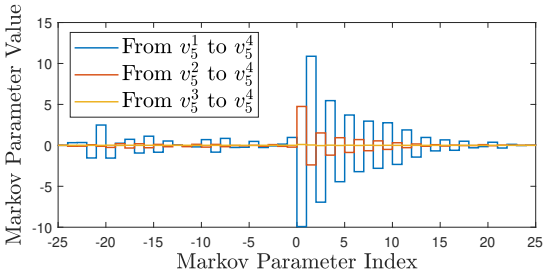

Fig. 3.3 Estimated Markov parameters from each pseudo input to the pseudo output for the transmissibility operator $\mathscr{T}_0$ defined in Table 3.1. The estimated Markov parameters were obtained using least squares with a noncausal FIR model with $r = 25$ and $d = 25$.

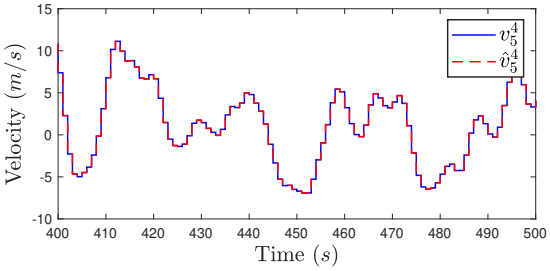

Fig. 3.4 The simulated output velocity v_5^4 and the predicted output velocity $\hat{v}_5^4$, where the predicted velocity is obtained using the identified transmissibility operator $\mathscr{T}_0$ and the measurements of v_1^5, v_2^5, and v_3^5.

the input current of the motor of the third vehicle in the second platoon. To emulate a burst transmission fault, a band-limited white noise is added to the communication link between the third and the fourth vehicles in the second platoon. Moreover, to emulate communication-

link time delay, a time delay of 2 seconds is introduced in the communication link between the third and fourth vehicles in the second platoon. Figures 5.10 and 3.6 show the norm of the residuals of the transmissibility operators defined in Table 3.1, where each fault is introduced separately at $t = 80$ seconds. The threshold limits are obtained by considering a signal-to-noise ratio of 20. Note from Figure 5.10 that at $t = 90$ seconds the norm of the residuals of the transmissibility operators $\mathscr{T}_0, \mathscr{T}_1, \mathscr{T}_3$, and $\mathscr{T}_4$ increased. Moreover, since the level of the residuals of $\mathscr{T}_2$ in Figure 5.10 did not change, then it follows from the Algorithm in 1 that platoon 2 is faulty, and thus $\tilde{j} = 2$. Note that at $t = 90$ seconds the norm of the residuals of the transmissibility operators $\mathscr{T}_2^2, \mathscr{T}_2^4$, and $\mathscr{T}_2^5$ did not change, where the norm of residual of the transmissibility operators $\mathscr{T}_2^3$ increased. Therefore, using the Algorithm in 1 we conclude that the third vehicle in the second platoon is faulty. Similar results are shown for the motor delay, cyberattack, and time-delay faults in Figures 5.10 and 3.6.

Next, we use the fault mitigation algorithm shown in Figure 3.2 to replace the faulty signal from the faulty vehicle i with a healthy signal that will be used as a reference for the succeeding vehicle $i+1$. Figure 3.7 shows the estimated Markov parameters for the transmissibility operator $\mathscr{T}_2^3$ obtained using least squares with a noncausal FIR model with $r = 50$ and $d = 0$. Figure 3.8 shows the velocity v_3^2 and the estimated velocity $\hat{v}_3^2$ obtained using the identified transmissibility $\mathscr{T}_2^3$ along with the measurement of v_2^2. We use the estimate $\hat{v}_3^2$ to obtain the correction signal $v_{3,\mathrm{mit}}$. Figure 3.9 shows the fourth vehicle velocity in the second platoon while the third vehicle is subject to a burst transmission. Note from Figure 3.9 that after applying the proposed fault mitigation algorithm at time $t = 160$ sec, the fourth vehicle in the second platoon starts to operate in a healthy manner again. The norm of the residual of the identified transmissibility $\mathscr{T}_0$ is shown in Figure 3.10 for the motor disturbances, motor delay, burst transmission, and DoS faults. Note from Figure 3.10 that at $t = 160$, the level of the residuals decreased due to utilizing the proposed fault mitigation algorithm.

3.3.2 Experimental Test

We consider the experimental setup shown in Figure 3.11 consisting of three autonomous Quanser robots called Qbots. Each Qbot consists of two coaxial wheels, where each wheel is driven by a DC motor. Qbots use closed-loop inverse kinematic controllers to obtain the DC motors commands for both wheels based on the desired linear and rotational velocities of the robot. Steering the robot leads to difference between the wheels' velocities, and thus angular motion of the Qbot. If the desired angular velocity is zero, then both wheels velocities are equal and the Qbot moves forward or backward in a straight line. Qbot1 receives the excitation signal from a computer through wireless communication, and Qbot2 is connected

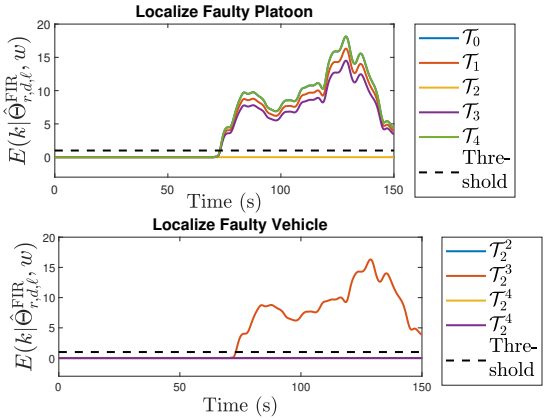

((a)) Motor disturbances.

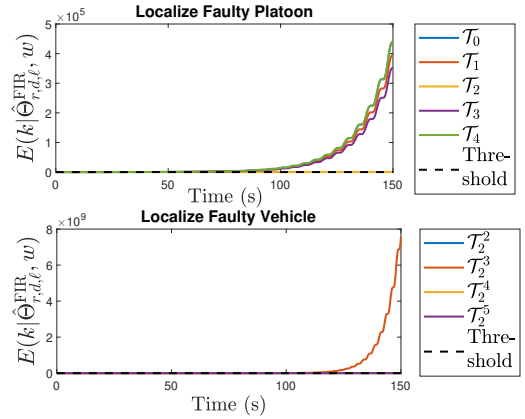

((b)) Motor delay.

Fig. 3.5 Norm of the residuals of the transmissibilities $\mathscr{T}_0,\ldots,\mathscr{T}_4$ and $\mathscr{T}_2^2,\ldots,\mathscr{T}_2^5$ computed using (5.30) with $w = 100$ steps for (a) Motor disturbances, and (b) Motor delay. We use Algorithm 1 to determine the faulty platoon and faulty vehicle. All faults are introduced separately at approximately $t = 80$ seconds.

with Qbot1 via a V2V communication channel. Similarly, Qbot3 is connected with Qbot2 via a V2V communication channel.

For health monitoring, we consider a one-dimensional motion for the platoon. We first run the setup by sending a zero-mean, unit variance, Gaussian random excitation signal to Qbot1. All Qbots run and move simultaneously depending only on V2V communications. We use least squares with a noncausal FIR model with $r = 25$ and $d = 25$ to identify the transmissibility operators $\mathscr{T}_1$ and $\mathscr{T}_2$ defined in Table 3.2, where v_1, v_2, and v_3 denote the velocities of Qbot1, Qbot2, and Qbot3, respectively. The estimated Markov parameters of the transmissibility operator $\mathscr{T}_1$ is shown in Figure 4.9. Moreover, Figure 4.10 shows the measured velocity v_3 and the predicted velocity $\hat{v}_3$ of Qbot3, where the predicted velocity is

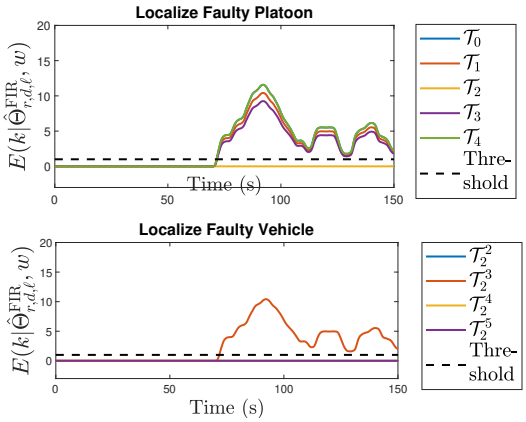

((a)) Burst transmission.

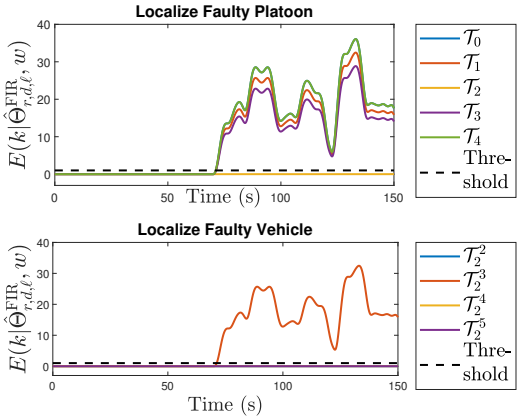

((b)) DoS.

Fig. 3.6 Norm of the residuals of the transmissibilities $\mathcal{T}_0, \ldots, \mathcal{T}_4$ and $\mathcal{T}_2^2, \ldots, \mathcal{T}_2^5$ computed using (5.30) with $w = 100$ steps for (a) Burst transmission, and (b) DoS. We use Algorithm 1 to determine the faulty platoon and faulty vehicle. All faults are introduced separately at approximately $t = 80$ seconds.

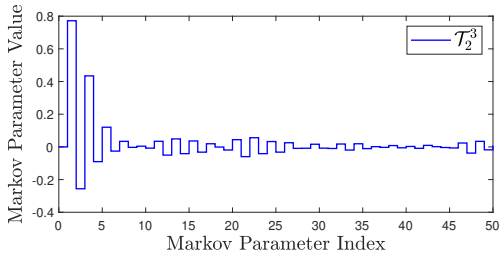

Fig. 3.7 Estimated Markov parameters for the transmissibility operator $\mathcal{T}_2^3$ obtained using least squares with a noncausal FIR model with $r = 50$ and $d = 0$.

obtained using the identified transmissibility and the measured velocities v_1 and v_2. Note

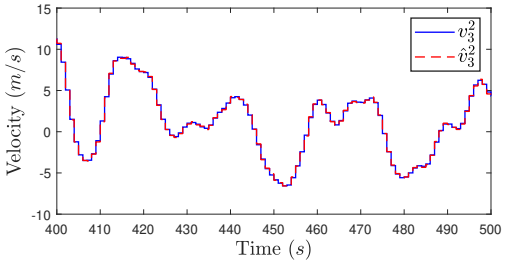

Fig. 3.8 Simulated output velocity and predicted output velocity of v_3^2, where the predicted velocity is obtained using the identified transmissibility $\mathscr{T}_2^3$ whose Markov parameters are shown in Figure 3.7 along with the measurement of v_2^2. The predicted output $\hat{v}_3^2$ is used in the fault mitigation algorithm.

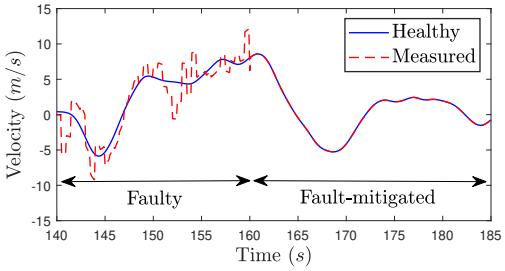

Fig. 3.9 Plot of the fourth vehicle velocity in the second platoon, v_4^2, before and after applying the fault mitigation algorithm, where the third vehicle in the same platoon is subject to a burst transmission. Note that, after applying the fault mitigation algorithm at $t = 160$, the fourth vehicle in the second platoon starts to operate in a healthy manner again.

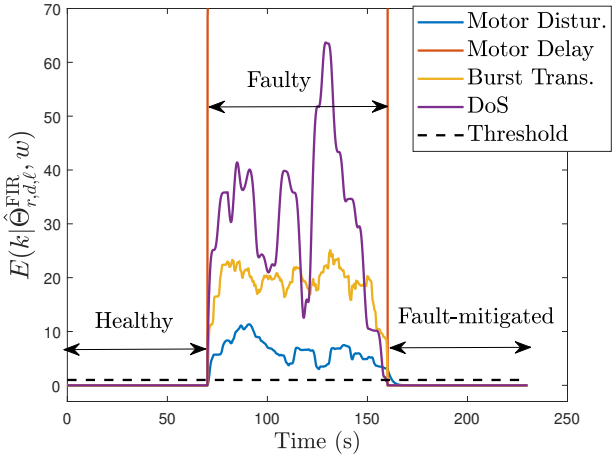

Fig. 3.10 Norm of the residuals of the transmissibility $\mathscr{T}_0$ introduced in Table 3.1. Note that at approximately $t = 160$ sec, the fault mitigation based on transmissibilities implemented, which leads to a decrease in the norm of residuals for proposed faults.

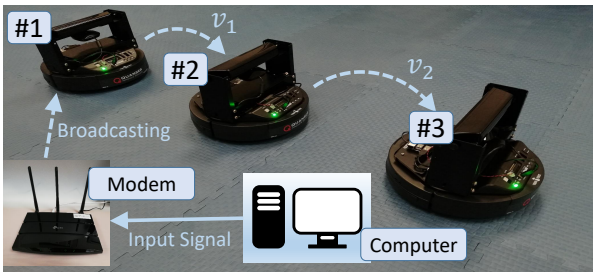

Fig. 3.11 The experimental setup of V2C communications: Qbot1 receives the desired velocity from the computer while Qbot2, and third Qbot3 receive the desired velocity from the preceding Qbot via V2V communication.

Operator	Pseudo Inputs	Pseudo Outputs
$\mathscr{T}_1$	v_1 and v_2	v_3
$\mathscr{T}_2$	v_1	v_2

Table 3.2 Pseudo inputs and pseudo outputs of the transmissibility operators $\mathscr{T}_1$ and $\mathscr{T}_2$ used for fault detection and localization in the experimental setup shown in Figure 3.11.

that neither the dynamics of the network nor the excitation signal of the network is used to obtain the predicted velocity $\hat{v}_3$ of Qbot3.

Next, we identify causal models of the transmissibility operators defined in Table 3.2 to use them for fault mitigation. Figure 3.13(a) shows the identified Markov parameters of the estimated transmissibility from each pseudo input to the pseudo output of the transmissibility operator $\mathscr{T}_1$ defined in Table 3.2. Figure 3.13(b) shows the measured velocity and the predicted velocity of Qbot3, where the predicted velocity is obtained using the identified transmissibility operator $\mathscr{T}_1$ shown in Figure 3.13(a) along with measurements of v_1 and v_2.

Disturbance fault

We consider injecting band-limited white noise in the command signal of the DC-motor that drives the right wheel of Qbot3 as represented in Figure 3.14, which results in a physical fault similar to the motor disturbances introduced in Appendix B.1. This makes the velocities of the wheels in Qbot3 not equal, which results in a 2-D motion of Qbot3 (i.e. a physical fault). Figure 3.15 shows the velocity of Qbot3 under healthy and faulty conditions. Figure 3.16 shows the norm of residual for the transmissibility operators $E(k|\hat{\Theta}^{\text{FIR}}_{r,d,\ell}, w)$ defined in Table 3.2. Note that at $t = 80$ sec, the norm of the residual of $\mathscr{T}_1$ increases, where the norm of the residual of $\mathscr{T}_2$ remains on the same level. Therefore, we conclude that Qbot3 is faulty. For fault mitigation, we use $\mathscr{T}_2$ and the measurements of v_1 to obtain the correction signal, which is used as a reference for Qbot3. Note from Figure 3.16 that after applying the fault mitigation algorithm at approximately $t = 180$ seconds, the norm of residual of $\mathscr{T}_1$ decreased.

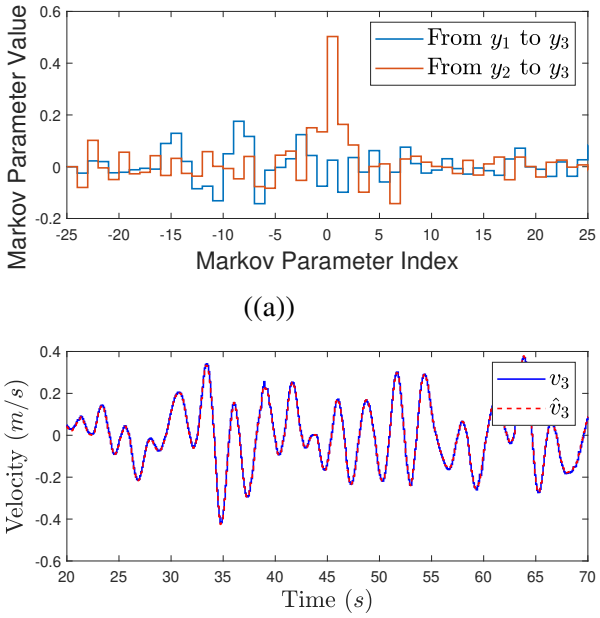

((a)) ((b))

Fig. 3.12 Experimental results: (a) estimated causal Markov parameters from each pseudo input to the pseudo output for the transmissibility operator $\mathscr{T}_1$ defined in Table 3.2, and (b) measured velocity and predicted velocity of Qbot3, where the predicted velocity is obtained using the identified transmissibility operator $\mathscr{T}_1$ whose parameters are shown in (a) and measurements of v_1 and v_2.

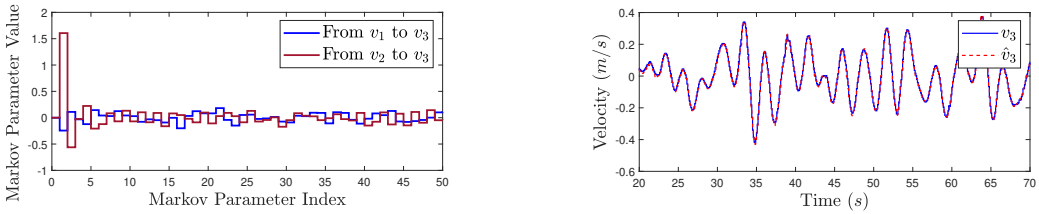

((a)) ((b))

Fig. 3.13 Experimental results: (a) estimated Markov parameters from each pseudo input to the pseudo output for the transmissibility operator $\mathscr{T}_1$ defined in Table 3.2, and (b) the measured velocity v_3 of Qbot3 and the predicted velocity $\hat{v}_3$ obtained using the identified transmissibility operator $\mathscr{T}_1$ whose parameters are shown in (a) and measurements of v_1 and v_2.

Internal time delay

We emulate the internal mechanical delay by considering a transport time delay in both command signals, which results in a similar fault to the motor delay introduced in Appendix B.1. That is a constant time delay between the controller and both actuators. Figure 3.14

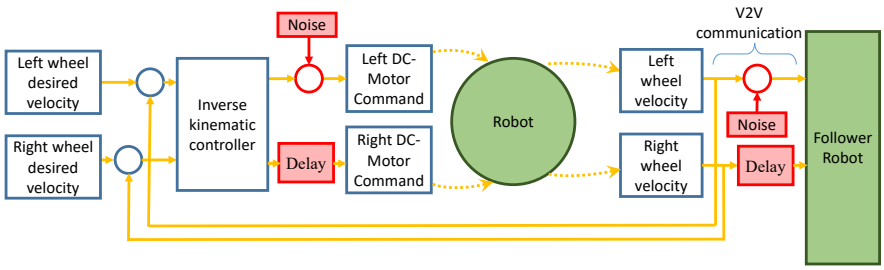

Fig. 3.14 Experimental emulation of the platoon faults. Four faults are considered separately, as represented by the red blocks. The physical faults include internal disturbances and internal mechanical delay within the closed loop control. The cyber faults are represented by injecting noise and delay to the information packet in the V2V communication link.

shows how the internal delay is emulated for the right actuator, which can be applied similarly to the left actuator. Figure 3.15 shows the velocity of Qbot3 under healthy and faulty conditions. Figure 3.16 shows the norm of residuals of the transmissibility operators defined in Table 3.2. Note from Figure 3.16 that at $t = 80$ seconds, the norm of the residual of $\mathscr{T}_1$ increases, where the norm of the residual of $\mathscr{T}_2$ remains on the same level. Therefore, we conclude that Qbot3 is faulty. Such a fault is inherent in the robot and cannot be mitigated using the proposed approach.

Cyber Attacks

Similar results can be obtained for the burst transmission and the DoS attacks as introduced in Appendix B.1, which we apply individually. For the burst transmission, a band-limited white noise signal is added to the velocity of Qbot2. The corrupted signal is then injected into the communication link between Qbot2 and Qbot3. For the communication time-delay fault, we consider individual cases of $1, 2$, and 3 seconds of time delay in the communication link between Qbot2 and Qbot3. Figure 3.14 shows a block diagram on how these faults are emulated. Figure 3.15 shows Qbot3 velocity under healthy and faulty conditions. Figure 3.16 shows the norm of the residuals for the transmissibility operators defined in Table 3.2. Note that, for the proposed faults, at $t = 80$ seconds the norm of the residual of $\mathscr{T}_1$ increases, whereas the norm of the residual of $\mathscr{T}_2$ remains on the same level. Since measurements from Qbot3 were used to construct $\mathscr{T}_1$ but not $\mathscr{T}_2$, we can conclude that Qbot3 is faulty. For fault mitigation, we inject the correction signal obtained using $\mathscr{T}_2$ and the measurements of v_1 in the communication link between Qbot2 and Qbot3. Note from Figure 3.16 that after applying the fault mitigation algorithm at approximately $t = 180$ the norm of the residual of $\mathscr{T}_1$ decreased.

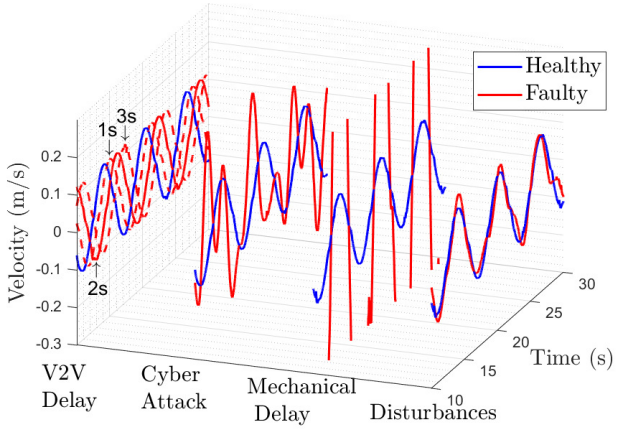

Fig. 3.15 Experimental results: The velocities of Qbot3 under healthy and faulty conditions, where the proposed faults are injected disturbance, mechanical (internal time) delay, cyberattack, and delay in the V2V communication link between Qbot2 and Qbot3.

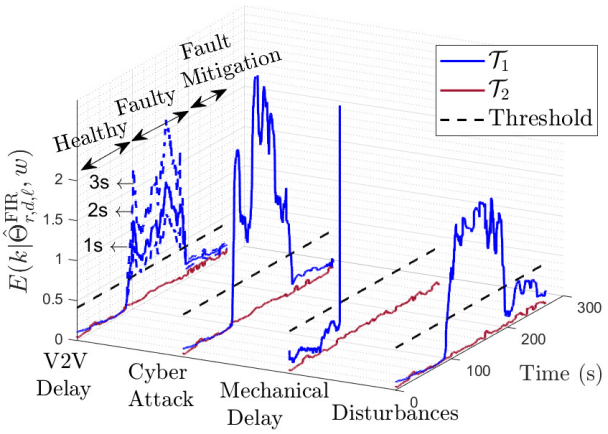

Fig. 3.16 Norm of the residuals of the transmissibilities $\mathscr{T}_1$ and $\mathscr{T}_2$ defined in Table 3.2 under the faults in Fig. 3.14. At $t = 80$ seconds, as $\mathscr{T}_1$ is faulty and $\mathscr{T}_2$ stays healthy, we conclude Qbot3 is faulty. After applying the fault mitigation algorithm at $t = 180$ the norm of the residual of $\mathscr{T}_1$ decreases. Note that since the mechanical delay is inherent in the robot, it cannot be mitigated using the proposed fault mitigation algorithm.

3.4 Experiment 2: Drunk Driver Detection in Mixed CAV Platoons

This section exploits the transmissibility estimation along CAV platoons in detecting drunk and intoxicated drivers while they are sandwiched between two CAVs. The proposed drunk

Table 3.3 The identified transmissibility operators used to detect drunk drivers from each pseudo input to the human-driven output v_3.

Operator	Pseudo inputs	Pseudo output
$\mathscr{T}_1$	v_2, v_4	v_3
$\mathscr{T}_2$	v_1, v_4	v_3
$\mathscr{T}_3$	v_2, v_5	v_3
$\mathscr{T}_4$	v_1, v_5	v_3

driver detection uses of CAVs' velocities along with the transmissibility relations $\mathscr{T}$ to estimate the human-driven vehicle's velocity in the mixed platoon.

3.4.1 Numerical Example

This section tests the proposed approach numerically using the bond graph model in Appendix A.1. We construct a five vehicles mixed platoon, where the third is human-driven and the rest are autonomous. The autonomous vehicles follow the model in Figure A.1. The human-driven vehicle follows the IDM model in (A.1)-(A.2). The platoon is set to move randomly by setting the desired velocity of the first vehicle to Gaussian noise as well as the external disturbances. We first run the platoon model under healthy conditions, and then implement the transmissibility identification introduced in Section 3.2.1. The identified parameters $\hat{\Theta}^{\text{FIR}}_{r,d}$ (Markov parameters) of the transmissibility operator that relates the output subset v_2, v_4 to v_3 are plotted in Figure 4.2. To validate the identified transmissibility first before implementing the drunk driver detection, we use the identified parameters in Figure 4.2 along with the measurements of v_2, v_4 to estimate v_3 while the platoon moves randomly. The measured velocity v_3 and its transmissibility-based estimation $\hat{v}_3$ are plotted in Figure 4.3. For further testing, we identify the transmissibility operators defined in Table 3.3 on the same way that is introduced in Section 3.2.1.

Next, we introduce the simulated drunk driver effects for BAC $= 0.02, 0.05$, and 0.08 separately by setting $\delta_{s^*}, \delta_s, \delta_{i_{\text{H}}-1}$, and $\delta_{i_{\text{H}}}$ to band limited white noise with a signal-to-noise ratio (SNR) of 10, and $t_v = t_s = 1$ second. The driver response time coefficient λ is set to $3, 2$, and 1 for BAC $= 0.02, 0.05$, and 0.08, respectively. To observe the norm of residuals, we compute E using (5.30) with $w = 100$ samples for all operators in Table 3.3 as shown in Figure 4.19 along with their thresholds using (5.31). The jump in the level of the norm of residuals above the threshold limits in Figure 4.19 indicates that abnormal driving conditions are detected.

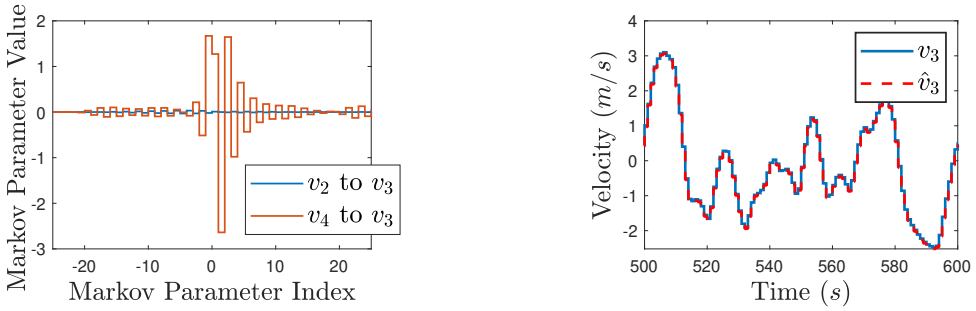

((a)) ((b))

Fig. 3.17 Simulation results: (a) The identified parameters $\hat{\Theta}^{\text{FIR}}_{r,d}$ (Markov parameters) of the transmissibility operator that relates the output subset v_2, v_4 to v_3, and (b) A comparison between the measurements of the velocity v_3 and its transmissibility-based estimation $\hat{v}_3$ The simulated output velocity of the third vehicle v_3 and the predicted output velocity $\hat{v}_3$. The estimation of $\hat{v}_3$ is obtained by implementing the identified transmissibility parameters in Figure 4.2 along with the measurements of v_2 and v_4.

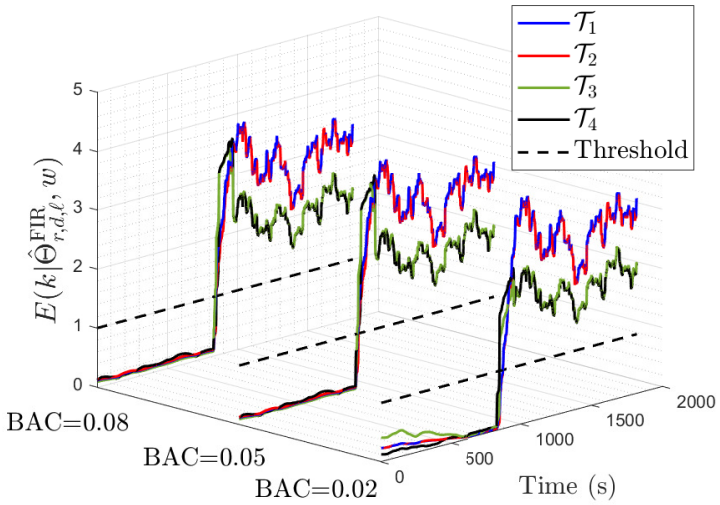

Fig. 3.18 Simulation results: Norm of the residuals of the transmissibilities $\mathcal{T}_1, \ldots, \mathcal{T}_4$ computed using (5.30) with $w = 100$ steps. The jump in the level of E above the threshold limits around time $t = 800$ seconds indicates that abnormal driving conditions are detected.

3.4.2 Experimental Test

Autonomous vehicles are robotics applications that consist of actuators, gross mass, sensors, and closed-loop tracking control. To test the proposed technique experimentally, the experimental setup shown in Figure 7.7 is used. This setup consists of three autonomous laboratory robots manufactured by Quanser called Qbot 2e. Qbot 2e is a differential mobile robot that extracts control commands based on an internal inverse kinematics controller. Similar

to any other differential robot, two control commands are generated from the controller separately to drive each of the two axial wheels. The angular motion of the differential robots is achieved by setting different velocities for each wheel. We construct the setup by setting the desired velocity of the first robot to Gaussian noise. The second robot is controlled remotely by a human to follow the first robot with level 0 automation. The third robot tracks the velocity of the second robot which is measured through an onboard depth sensor in the third robot. Moreover, the third robot receives the velocity signal of the first robot using a V2V communication link.

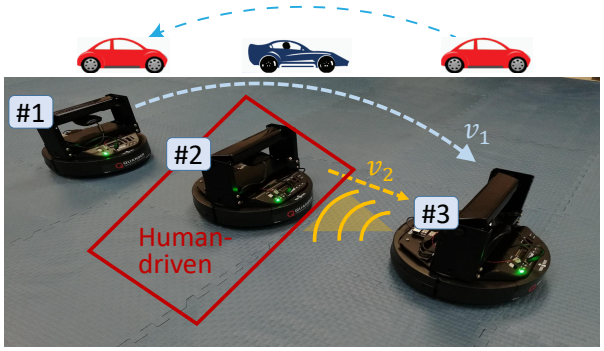

Fig. 3.19 The first experimental setup: The first robot receives the excitation signal from a computer through a wireless connection. The second robot is human-driven through the computer keyboard. The third robot receives the first robot velocity v_1 via V2V communication and measures the second robot velocity v_2 using an onboard depth sensor.

One-dimensional motion of the setup is considered to characterize the longitudinal motion of the platoon. This is done by setting the velocities of both wheels in the same robot to equal each other. Define two transmissibility operators, the first is $\mathscr{T}_1$ from v_1 to v_2, and the second is $\mathscr{T}_3$ from v_3 to v_2. Both operators are identified as in Section 3.2.1. The identified parameters $\hat{\Theta}^{\text{FIR}}_{r,d}$ (Markov parameters) of both transmissibilities $\mathscr{T}_1, \mathscr{T}_3$ are plotted in Figure 4.9. To validate the identified transmissibilities first before implementing the drunk driver detection, we use the identified parameters of the operator $\mathscr{T}_1$ in Figure 4.9 along with the measurements of v_1 to estimate v_2. The measured velocity v_2 and its transmissibility-based estimation $\hat{v}_2$ are plotted in Figure 4.10. To experience the drunk driver behavior, the effects of BAC$=0.05$ shown in Table B.1 were simulated to the interface of the second robot. The reduced coordination and decline in the visual functions are simulated by adding parameters uncertainties to the second robot model. The reduced ability to track moving objects is added as a delay in the human command that is sent from the human to the robot. To simulate the slower response, an equivalent damping was added to the controller of the second robot to yield a higher settling time. To observe the norm of residuals, we compute E using (5.30)

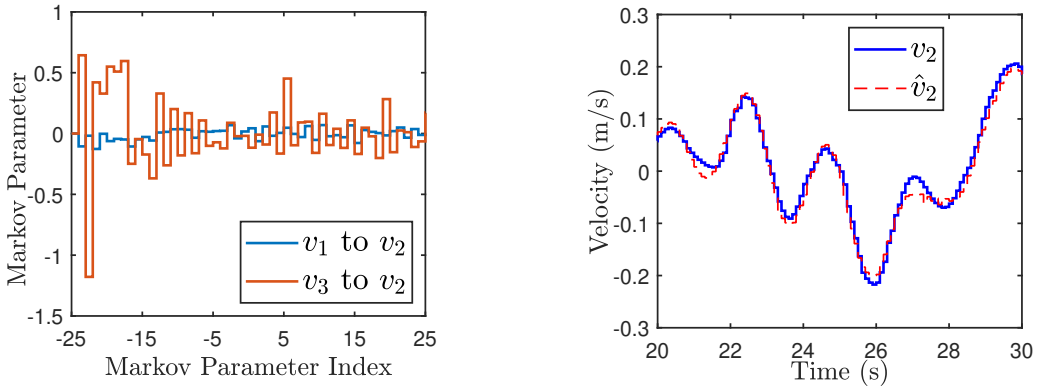

((a)) ((b))

Fig. 3.20 Experiment 1 results: (a) The identified parameters $\hat{\Theta}^{\text{FIR}}_{r,d}$ (Markov parameters) of the transmissibility operators $\mathcal{T}_1, \mathcal{T}_3$ used in the first experiment, and (b) A comparison between the measurements of the velocity v_2 and its transmissibility-based estimation $\hat{v}_2$. The estimation of $\hat{v}_2$ is obtained by implementing the identified transmissibility parameters of $\mathcal{T}_1$ in Figure 4.9 along with the measurements of v_1.

with $w = 100$ samples as in Figure 4.15 along with their thresholds using (5.31). The jump in the level of the norm of residuals above the threshold limits at time $t = 50$ seconds in Figure 4.19 indicates that abnormal driving conditions are detected.

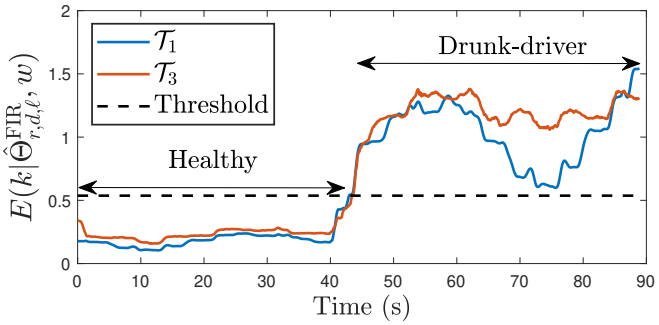

Fig. 3.21 Experiment 1 results: Norm of the residuals of the transmissibility operators $\mathcal{T}_1, \mathcal{T}_3$ used in the first experiment computed using (5.30) with $w = 100$ steps. The jump in the level of E above the threshold limits around time $t = 50$ seconds indicates that abnormal driving conditions are detected.

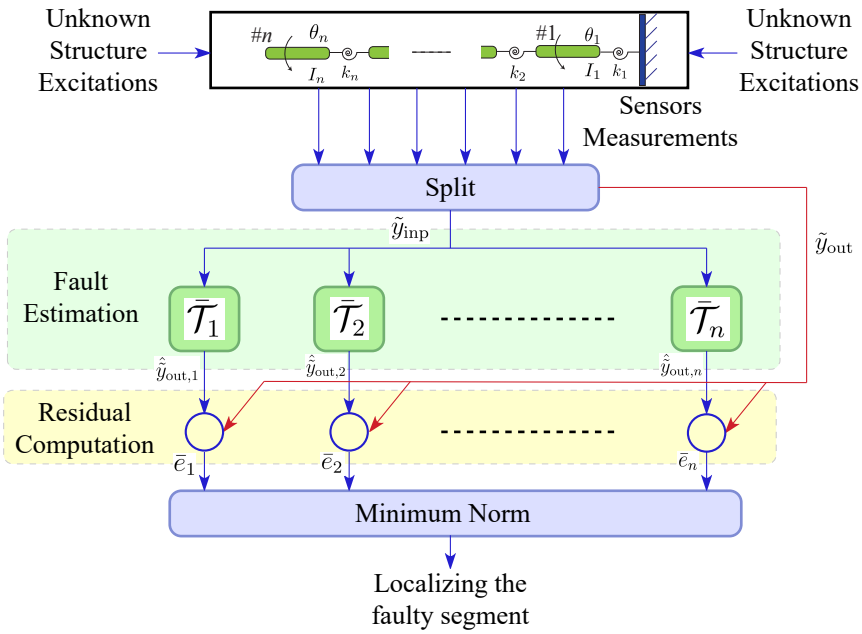

Fig. 3.22 Block diagram of the proposed approach that summarizes the fault localization on a structure with n segments.

3.5 Experiment 3: Structural Health Monitoring

3.5.1 Fault Localization in Flexible Beams

Assume a fault at segment i, and the state space model in (7.1)-(7.3) to be updated accordingly as

$$\dot{\tilde{x}}(t) = A\tilde{x}(t) + Bf(t,\tilde{x},u,w) + B_i F(t), \tag{3.30}$$

$$\tilde{y}_{\text{inp}}(t) = C_{\text{inp}}\tilde{x}(t), \tag{3.31}$$

$$\tilde{y}_{\text{o}}(t) = C_{\text{o}}\tilde{x}(t), \tag{3.32}$$

where $\tilde{x}$ are the faulty states, and $\tilde{y}_{\text{inp}}, \tilde{y}_{\text{o}}$ are the faulty sensor measurements. The fault is represented in the term $B_i F$ such that F represents the unknown fault dynamics on the segment i, and $B_i \in \mathbb{R}^n$ represents the matrix index. F depends on the fault class and its the same for the same fault (e.g. fatigue or creep cracks) regardless of the fault location. The vector B_i determines the fault location within the structure. B_i can be defined for all $i \in \{1,\ldots,n\}$ as

$$\bar{B}_i = \begin{bmatrix} 0 & \ldots & 0 & 1 & 0 & \ldots & 0 \end{bmatrix}^{\text{T}}, \tag{3.33}$$

where the index that carries the number 1 differs according to the fault location. Although, localizing the fault is possible by identifying B_i, the unknown excitations, and nonlinearities f as well as the unknown fault dynamics F prevent implying typical identification algorithms. Rearrange the faulty state equation in (3.30) to render F as an independent excitation, such as

$$\dot{\tilde{x}}(t) = A\tilde{x}(t) + \bar{B}_i \bar{f}(t, \tilde{x}, u, w, F), \tag{3.34}$$

where

$$\bar{f}(t,x,u,w,F) = \begin{bmatrix} f(t,x,u,w) & F(t) \end{bmatrix}^{\mathrm{T}},$$
$$\bar{B}_i = \begin{bmatrix} B & B_i \end{bmatrix}.$$

Next, for all $i \in \{1,\ldots,n\}$ define the transmissibility operator

$$\tilde{y}_{\mathrm{o}}(t) = \bar{\mathscr{T}}_i(\mathbf{p})\tilde{y}_{\mathrm{inp}}(t), \tag{3.35}$$

where

$$\bar{\mathscr{T}}_i(\mathbf{p})\bar{\Gamma}_{\mathrm{o},i}(\mathbf{p})\bar{\Gamma}^{-1}_{\mathrm{inp},i}(\mathbf{p}), \tag{3.36}$$

and

$$\bar{\Gamma}_{\mathrm{inp},i}(\mathbf{p})C_{\mathrm{inp}}\mathrm{adj}(\mathbf{p}I - A)\bar{B}_i \in \mathbb{R}^{m\times m}[\mathbf{p}], \tag{3.37}$$
$$\bar{\Gamma}_{\mathrm{o},i}(\mathbf{p})C_{\mathrm{o}}\mathrm{adj}(\mathbf{p}I - A)\bar{B}_i \in \mathbb{R}^{1\times m}[\mathbf{p}]. \tag{3.38}$$

Notice that the operator $\bar{\mathscr{T}}_i$ is robust against faults at segment i since $\bar{\mathscr{T}}_i$ is constructed using $\bar{B}_i$, and regardless what the excitations collected in f. An estimation of the faulty output subset $\tilde{y}_{\mathrm{o}}$ while the fault is at segment $i \in \{1,\ldots,n\}$ is computed using

$$\hat{\tilde{y}}_{\mathrm{o},i}(k) = \bar{\mathscr{T}}_i(\mathbf{q})\tilde{y}_{\mathrm{inp}}(k). \tag{3.39}$$

Define the residuals each segment

$$\bar{e}_i(k) = y_{\mathrm{o}}(k) - \hat{\tilde{y}}_{\mathrm{o},i}(k). \tag{3.40}$$

Assume the beam to run for ℓ steps, then compute the norm of residual for all $i \in \{1,\ldots,n\}$

$$\bar{E}_i(k) \stackrel{\Delta}{=} \sqrt{\sum_{j=0}^{\ell} \|\bar{e}_i(j)\|}. \tag{3.41}$$

Using $\bar{\mathscr{T}}_i$ along with the faulty measurements of $\tilde{y}_{\text{inp}}$ results in an accurate estimation of the faulty output $\hat{\tilde{y}}_{\text{o}}$ if the faulty segment is i. Since $\bar{\mathscr{T}}_i$ is independent on the fault $F(t)$, then regardless what the fault class is, $\bar{\mathscr{T}}_i$ will accurately estimate the faulty output $\tilde{y}_{\text{o}}$ if the faulty segment is i. However, if the faulty segment is not i, then the estimation of $\bar{\mathscr{T}}_i$ is not accurate. The proposed approach defines $\bar{\mathscr{T}}_i$ for all $i \in \{1,\ldots,n\}$. The operator with the least estimation error level is considered to correspond to the faulty segment. Figure 3.22 summarizes the proposed fault localization algorithm.

3.5.2 Numerical Example

The cantilever beam modeled in Appendix A.3 was constructed with $n = 10$ segments, and the parameters for all $i \in \{1,\ldots,10\}$, $I_i = 0.001kg.m^2, k_i = 22N.m/rad$, and $b_i = 0.01(N.m)/(rad/sec)$. We run the model by setting T_1, T_3, T_5, T_8, g, w to bounded white noise with unit variance and zero mean. The least squares identification in (3.21) is then implemented to identify the operator $\mathscr{T}$ under healthy conditions with $r = d = 5$, and the identified parameters are plotted in Figure 4.2. Figure 3.24 validates the identified parameters in Figure 4.2. To test the fault detection algorithm, the fatigue fault introduced in Section B.3 was emulated on the third segment at time $t = 100$ seconds. Figure 4.19 shows the norm of residual E computed using (5.30) over a sliding window with width $W = 100$ steps. Notice that the operator $\mathscr{T}$ was able to detect the fatigue crack effectively.

Next, to localize faults, the operators $\tilde{\mathscr{T}}_1,\ldots,\tilde{\mathscr{T}}_{10}$ were identified using (3.21) with all orders $r = d = 5$. Figure 3.26 validates the faulty measurements' estimation of $\tilde{y}_{10}$ using $\tilde{\mathscr{T}}_3$, and while the fatigue crack was emulated at the third segment. Notice from Figure 3.26 that the operator $\tilde{\mathscr{T}}_3$ was able to accurately estimate $\tilde{y}_{10}$ since the crack was at the same segment that the transmissibility operator was identified on. The right upper part of Figure 3.27 shows the norm of residual of all faulty operators $\tilde{\mathscr{T}}_1,\ldots,\tilde{\mathscr{T}}_{10}$ over a testing time of 100 seconds. It can be observed that only the transmissibility operator that corresponds to the faulty segment will be able to estimate the faulty measurements $\tilde{y}_{10}$. Thus, we conclude that the fault was in the third segment. The same test was conducted by emulating the fault at the first, eighth, and tenth segments separately. All the norm of residuals is plotted in Figure 3.27. Notice that the proposed approach could even localize the fault at the tip and fixed ends of the cantilever beam.

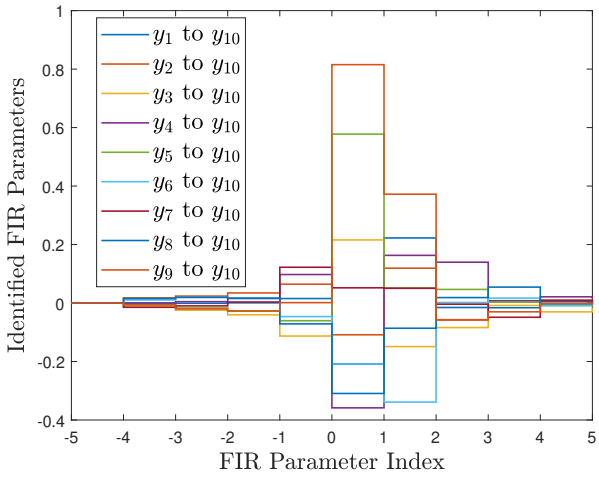

Fig. 3.23 Simulation Results: Identified parameters of the operator $\mathscr{T}$ under healthy conditions with $r = d = 5$.

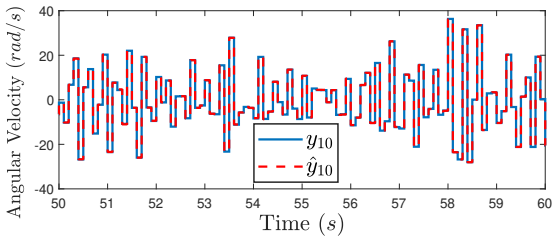

Fig. 3.24 Simulation Results: Comparison between the measured and estimated outputs of the tenth segment under healthy conditions. This Figure validates the identified parameters of the transmissibility operator $\mathscr{T}$ plotted in Figure 4.2.

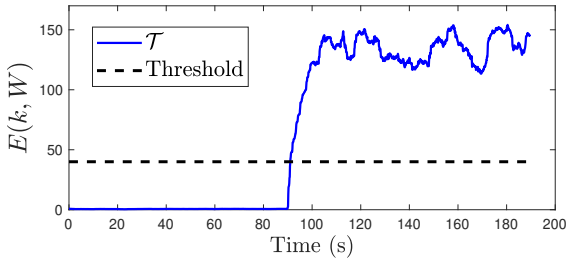

Fig. 3.25 Simulation Results: Norm of residual over a sliding window of the estimation of transmissibility operator $\mathscr{T}$. The fatigue crack was emulated at the third segment around time $t = 100$ seconds.

3.5.3 Experimental Test

The proposed approach was tested on the setup shown in Figure 7.7. This setup consists of a flexible cantilever beam that is excited randomly by hand at the free tip. The beam is

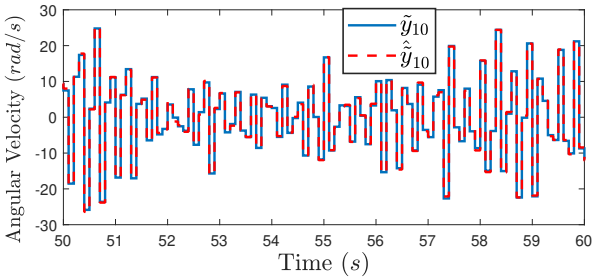

Fig. 3.26 Simulation Results: Comparison between the measured and estimated outputs of the tenth segment, while the third segment is faulty. This Figure validates the ability of the operator $\tilde{\mathscr{T}}_3$ to accurately estimate the faulty measurements if the actual fault location matches the fault location that $\tilde{\mathscr{T}}_3$ was constructed on.

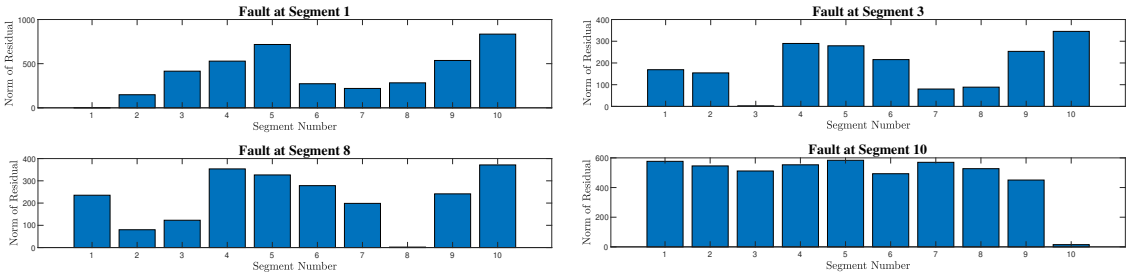

Fig. 3.27 Simulation Results: Norms of residual of the operators $\tilde{\mathscr{T}}_1, \ldots, \tilde{\mathscr{T}}_{10}$ for four separate experiments. The fatigue fault was emulated at a different location during each experiment. Notice that the purposed approach was able to localize the fault even at the free and fixed ends.

divided into the seven segments shown in the Figure. Three laser Polytech IVS-500 laser vibrometers are mounted and adjusted perpendicularly to the beam at stationary at three different locations. The least squares identification in (3.21) is then implemented to identify the operator $\mathscr{T}$ under healthy conditions with $r = d = 50$. The identified parameters of $\mathscr{T}$ are plotted in Figure 3.29. Figure 3.30 validates the identified parameters in Figure 3.29. An experimental fault was emulated by attaching a rigid strain to the beam. This fault will increase the stiffness at the fault location. The fault was first emulated at the third segment around time $t = 100$ seconds. Figure 4.15 shows the norm of residual E computed using (5.30) over a sliding window with width $W = 100$ steps. Notice that the operator $\mathscr{T}$ was able to detect the experimental fault effectively.

Next, to localize the experimental fault the operators $\tilde{\mathscr{T}}_1, \ldots, \tilde{\mathscr{T}}_7$ were identified using (3.21) with all orders $r = d = 50$. Figure 3.32 validates the faulty measurements' estimation of $\tilde{y}_3$ using $\tilde{\mathscr{T}}_3$, and while the experimental fault was emulated at the third segment. Notice from Figure 3.32 that the operator $\tilde{\mathscr{T}}_3$ was able to accurately estimate, $\tilde{y}_3$ since the fault is at

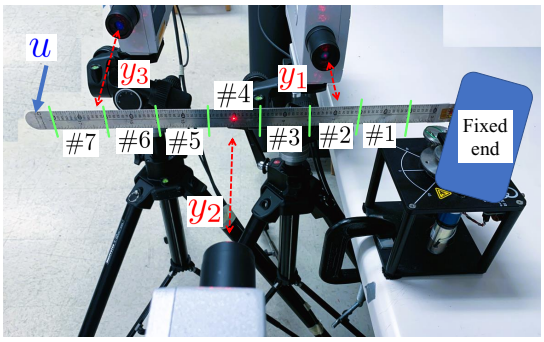

Fig. 3.28 The experimental setup. A flexible cantilever beam with random excitations at the tip. The beam is divided into seven segments. Three laser vibrometers are mounted to measure the acceleration at three different locations.

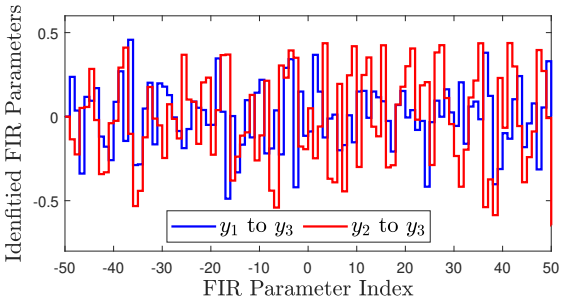

Fig. 3.29 Experimental Results: Identified parameters of the operator $\mathscr{T}$ under healthy conditions with $r = d = 50$.

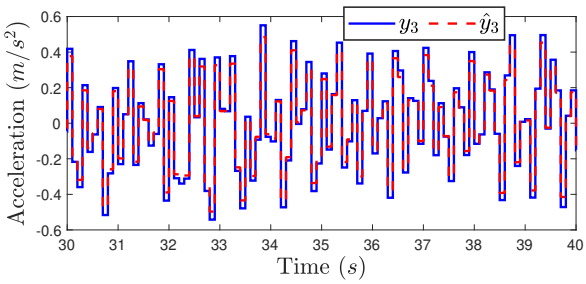

Fig. 3.30 Experimental Results: Comparison between the measured and estimated outputs of the third sensor under healthy conditions. This Figure validates the identified parameters of the transmissibility operator $\mathscr{T}$ plotted in Figure 3.29.

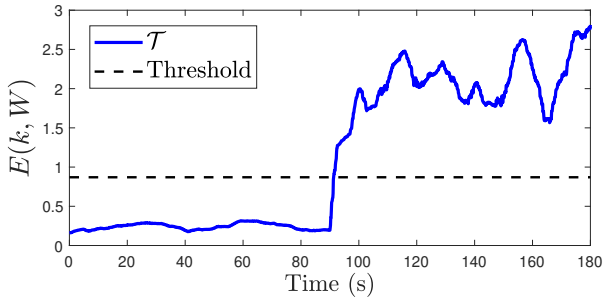

Fig. 3.31 Experimental Results: Norm of residual over a sliding window of the estimation of transmissibility operator $\mathscr{T}$. The experimental faulty was emulated at the third segment around time $t = 100$ seconds.

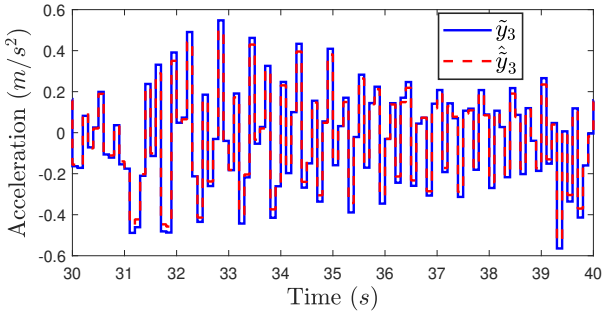

Fig. 3.32 Experimental Results: Comparison between the measured and estimated outputs of the third sensor while the third segment is faulty. This Figure validates the ability of the operator $\tilde{\mathscr{T}}_3$ to accurately estimate the faulty measurements if the actual fault location matches the fault location that $\tilde{\mathscr{T}}_3$ was constructed on.

the same segment that the transmissibility operator was identified on. The right upper part of Figure 3.33 shows the norm of residual of all faulty operators $\tilde{\mathscr{T}}_1, \ldots, \tilde{\mathscr{T}}_7$ over a testing time of 100 seconds. It can be observed that only the transmissibility operator that corresponds to the faulty segment will be able to estimate the faulty measurements $\tilde{y}_3$. Thus, we conclude that the fault is in the third segment. The same test was conducted by emulating the fault at the first, fifth, and seventh segments separately. All the norm of residuals is plotted in Figure 3.27.

3.6 Experiment 4: Actuator Fault Detection

3.6.1 Numerical Example

The parameters shown in Table A.2 are used to construct the system (A.10), (A.11) in Figure A.3 with $n = 12$ actuators to characterize the reticle stage with multi-piezoelectric

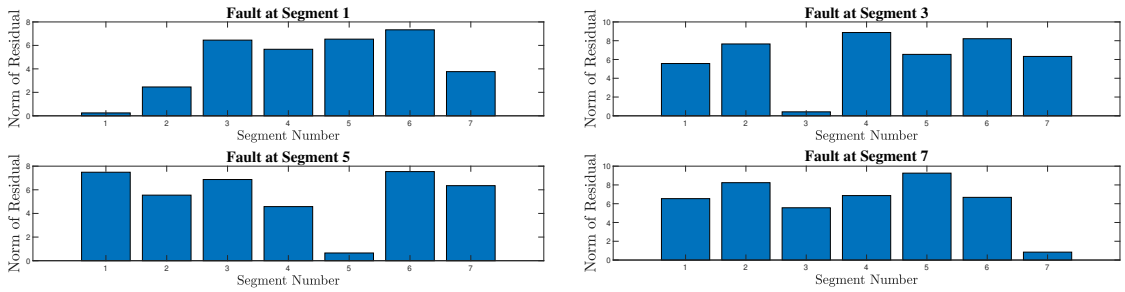

Fig. 3.33 Experimental Results: Norms of residual of the operators $\tilde{\mathscr{T}}_1,\ldots,\tilde{\mathscr{T}}_7$ for four separate experiments. The experimental fault was emulated at a different location during each experiment.

actuators. We consider a square rigid middle stage as the reticle stage with length $l = 0.132$ m and 3 actuators on each side of the middle stage, that is, $m_x = 3, n_x = 6$, and $m_y = 9$. We consider actuators #1,#3,#4,#6,#7,#9,#10,#12 to be on the stage corners and actuators #2,#5,#8,#11 to be aligned with the stage's center of mass, that is, $\alpha_1 = 45^o, \alpha_2 = 0^o, \alpha_3 = 315^o, \alpha_4 = 135^o, \alpha_5 = 180^o, \alpha_6 = 225^o, \alpha_7 = 45^o, \alpha_8 = 90^o, \alpha_9 = 135^o, \alpha_{10} = 315^o, \alpha_{11} = 270^o, \alpha_{12} = 225^o$. Moreover, $l_1 = l_3 = l_4 = l_6 = l_7 = l_9 = l_{10} = l_{12} = 0.0934$ m, and $l_2 = l_5 = l_8 = l_{11} = 0.066$ m. Furthermore, we set $\alpha_a = 180^o, \alpha_b = 45^o, l_a = 0.06$ m, and $l_b = 0.09$ m.

We consider the first two transmissibility operators, $\mathscr{T}_{b_x,a_x|4}$ that relates a_x with b_x while actuator #4 is active, and $\mathscr{T}_{b_y,a_y|9}$ that relates a_y with b_y while actuator #9 is active. The active actuator excitation signal is set to Gaussian white noise with zero mean and unit variance while considering the healthy conditions of the system.

Then, we use the least squares with a noncausal FIR model with $r = 25$ and $d = 25$ to identify the transmissibilities $\mathscr{T}_{b_x,a_x|4}$ and $\mathscr{T}_{b_y,a_y|9}$. Figure 3.34 shows the identified Markov parameters of the transmissibilities $\mathscr{T}_{b_x,a_x|4}$ and $\mathscr{T}_{b_y,a_y|9}$ obtained under healthy conditions. For validation, Figures 3.35 and 3.36 show the simulated displacement and the predicted displacement of b_x and b_y, respectively, where the predicted displacements are obtained using the identified transmissibility operators $\mathscr{T}_{b_x,a_x|4}$ and $\mathscr{T}_{b_y,a_y|9}$, respectively, along with the measurements of a_x and a_y.

We then obtain the transmissibility operators $\mathscr{T}_{b_x,a_x|5}$ from a_x to b_x while actuator #5 is active, $\mathscr{T}_{b_y,a_y|7}$ from a_y to b_y while actuator #7 is active, $\mathscr{T}_{b_x,a_x|1}$ from a_x to b_x while actuator #1 is active, and $\mathscr{T}_{b_y,a_y|12}$ from a_y to b_y while actuator #12 is active. Three transmissibility operators, $\mathscr{T}_{b_x,a_x|4}, \mathscr{T}_{b_x,a_x|5}$, and $\mathscr{T}_{b_x,a_x|1}$ are used to obtain three independent estimations of $\hat{b}_x$ based on the measurements of a_x. Similarly, the operators $\mathscr{T}_{b_y,a_y|9}, \mathscr{T}_{b_y,a_y|7}$, and $\mathscr{T}_{b_x,a_x|12}$ are used to obtain three independent estimations of $\hat{b}_y$ based on the measurements of a_y. Six residuals are then computed for the six estimations by comparing them with the measured b_x and b_y. The norm of residuals over a sliding window for the six residuals are then computed

using (5.30) with window width $w = 100$ steps ($t = 10$ seconds). The threshold limits for the six residuals are computed using (5.31).

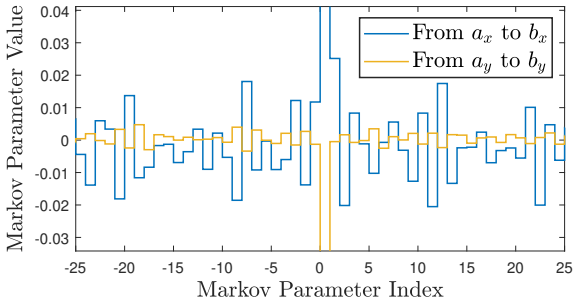

Fig. 3.34 Estimated Markov parameters of the operators $\mathscr{T}_{b_x,a_x|4}$ and $\mathscr{T}_{b_y,a_y|9}$. The estimated Markov parameters are obtained using the least squares with a noncausal FIR model with $r = 25$ and $d = 25$.

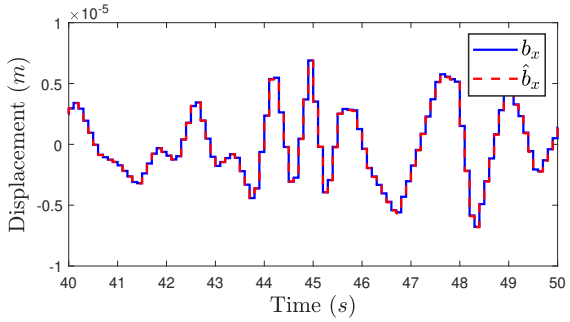

Fig. 3.35 Simulated output and predicted output b_x where the predicted output is obtained using the identified transmissibility operator $\mathscr{T}_{b_x,a_x|4}$ along with the measurements of a_x.

Next, we apply both faults introduced in section B.1 to the six actuators that the transmissibility operators are constructed when they were active. We then use transmissibilities

Table 3.4 Simulation parameters for the multi-actuator system in (A.10)-(A.11).

Parameter	Description	Value
M_p	Middle stage mass	$2.45kg$
J	Middle stage moment of inertia	$0.0997kg.m^2$
l	Middle stage length	$0.132m$
$M_{a,i}$	Actuator mass	$0.028kg$
$k_{a,i}$	Actuator stiffness	$100 \times 10^6 N/m$
$C_{a,i}$	Actuator damping	$2681.13N.s/m$
$k_{h,i}$	Hinge stiffness	$2 \times 10^4 N/m$
$C_{h,i}$	Hinge damping	$500N.s/m$

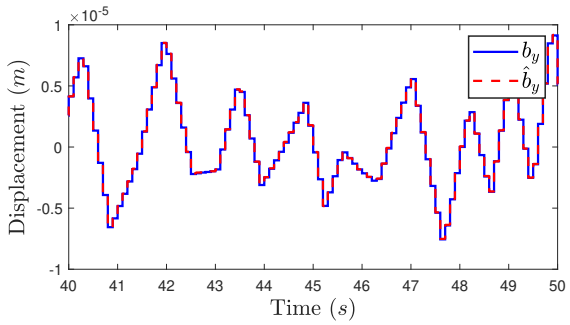

Fig. 3.36 Simulated output and predicted output b_y obtained using the identified transmissibility operator $\mathscr{T}_{b_y,a_y|9}$ along with the measurements of a_y.

to detect these faults without the need to know the excitation signal or the system dynamics. To emulate the loss of effectiveness fault, we increase the actuator hinge stiffness to $k_{h,i,\text{creep}} = 2.6 \times 10^4 N/m$. For the fatigue crack, we set the hinge stiffness to $k_{h,i,\text{crack}} = 1.33 \times 10^4 N/m$ while the crack is open, and keep it $k_{h,i,\text{crack}} = 2 \times 10^4 N/m$ while the crack is closed. We run the system by setting actuators #4 and #9 to band-limited white Gaussian noise. The system was kept healthy for the first 100 seconds. Figure 5.10 shows the norm of residuals of the identified transmissibility operators for each fault computed using (5.30) with $w = 100$ steps. The faults are then emulated individually, one at each run at time $t = 100$ seconds. Note that these figures are computed using a sliding window with width $w = 100$, where the sampling time is 0.1 second. This means the value computed at time t seconds uses all the residual values within the time period from t to $(t + 10)$ seconds. For example, in Figure 5.10, the x-Fatigue fault occurred at time $t = 100$ seconds. The norm of residual started increasing at time $t = 90$ seconds as all values from time $t = 90$ to $t = 100$ seconds are used to compute E at time $t = 90$ seconds. The fault was detected at almost $t = 92$, which is two seconds after the fault actually occurred. The 2 seconds delay in detecting the fault is in fact related to the assumed threshold limit to eliminate false alarms.

Similar to testing $\mathscr{T}_{b_x,a_x|4}$ and $\mathscr{T}_{b_y,a_y|9}$, we test the transmissibility operators $\mathscr{T}_{b_x,a_x|5}$, $\mathscr{T}_{b_x,a_x|7}$, $\mathscr{T}_{b_x,a_x|1}$, and $\mathscr{T}_{b_x,a_x|12}$ with the active actuator #5, #7, #1, and #12, respectively. We apply the faults introduced in B.1 to the active actuator in each transmissibility operator separately. Figure 3.38 shows the norm of residuals of the identified transmissibility operators $\mathscr{T}_{b_x,a_x|5}$ and $\mathscr{T}_{b_x,a_x|7}$ for each fault computed using (5.30) with $w = 100$ steps, where the faults occur at $t = 100$ seconds in each case. Figure 3.39 shows the norm of residuals of the identified transmissibility operators $\mathscr{T}_{b_x,a_x|1}$ and $\mathscr{T}_{b_x,a_x|12}$ for each fault computed using (5.30) with $w = 100$ steps, where the faults occur at $t = 100$ seconds in each case. Note from Figures 5.10, 3.38, and 3.39 that the faults are detected in each case effectively.

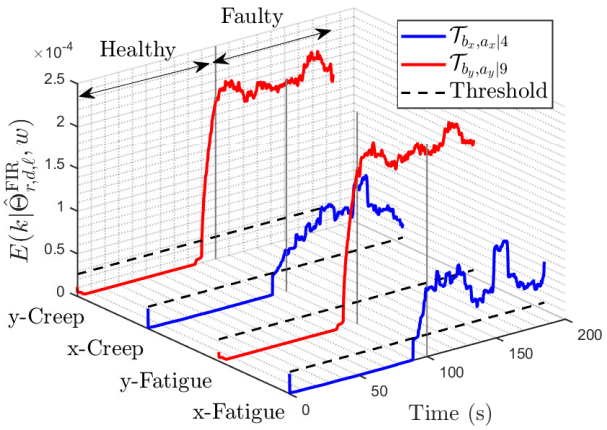

Fig. 3.37 Norm of the residuals of the transmissibilities $\mathcal{T}_{b_x,a_x|4}$ and $\mathcal{T}_{b_y,a_y|9}$ shown in Figure 3.34 computed using (5.30) with $w = 100$ steps. Note that at $t = 100$ seconds the level of the norm of the residual change, and thus we conclude that the active actuator is faulty.

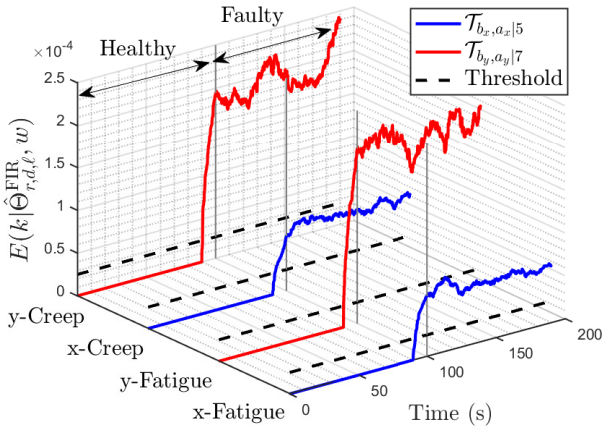

Fig. 3.38 Norm of the residuals of the transmissibilities $\mathcal{T}_{b_x,a_x|5}$ and $\mathcal{T}_{b_y,a_y|7}$ computed using (5.30) with $w = 100$ steps. Note that at $t = 100$ seconds the level of the norm of the residual change, and thus we conclude that the active actuator is faulty.

3.6.2 Experimental Test

We consider the experimental setup shown in Figure 7.7 consisting of twelve actuators to move the middle stage parallel to the ground in the X-Y plane. Each actuator has an internal spring and a rigid link connected to the middle stage with two screws. Every actuator operates by pulling the link attached to it. Two 2-axis accelerometers, a and b, are attached to the middle stage. The setup is mounted on an anti-vibration table to minimize the noise. The

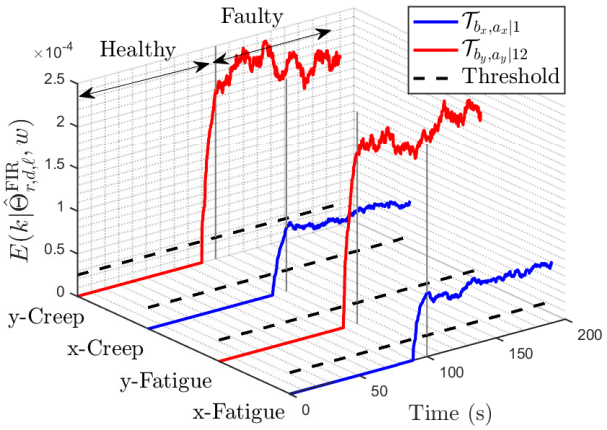

Fig. 3.39 Norm of the residuals of the transmissibilities $\mathcal{T}_{b_x,a_x|1}$ and $\mathcal{T}_{b_y,a_y|12}$ computed using (5.30) with $w = 100$ steps. Note that at $t = 100$ seconds the level of the norm of the residual change, and thus we conclude that the active actuator is faulty.

maximum rotation angle of the middle stage is 10 degrees, and thus the coupling effect is neglected.

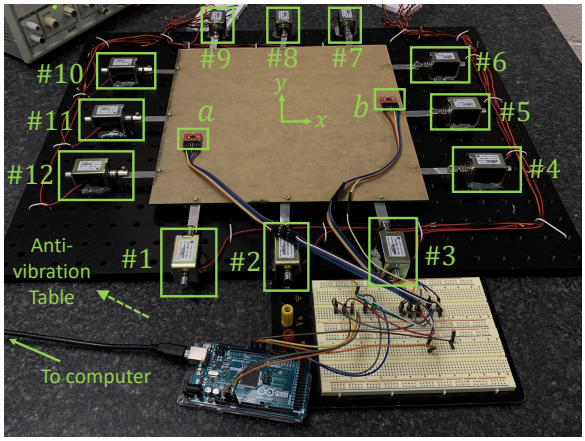

Fig. 3.40 The experimental setup consists of twelve actuators to move the middle stage. Two two-axis accelerometers, a and b, are attached on the middle stage.

Then, we use least squares with a noncausal FIR model with $r = 100$ and $d = 100$ to identify the transmissibilities $\mathcal{T}_{b_x,a_x|i}$ or $\mathcal{T}_{b_y,a_y|i}$, where x and y denote the direction of motion and $i \in \{1,\ldots,12\}$ is the active actuator. The input voltage applied to the active actuator is a random signal that varies between $9-12$ volts tuned by hand. Figure 3.41 shows the estimated Markov parameters of the transmissibilities $\mathcal{T}_{b_y,a_y|1}$, $\mathcal{T}_{b_x,a_x|4}$, $\mathcal{T}_{b_y,a_y|8}$, and $\mathcal{T}_{b_x,a_x|12}$. For validation, Figure 3.42 shows the measured acceleration and the predicted acceleration of

b_y, where the predicted acceleration is obtained using the identified transmissibility operator $\mathscr{T}_{b_y,a_y|1}$ and the measurement of a_y.

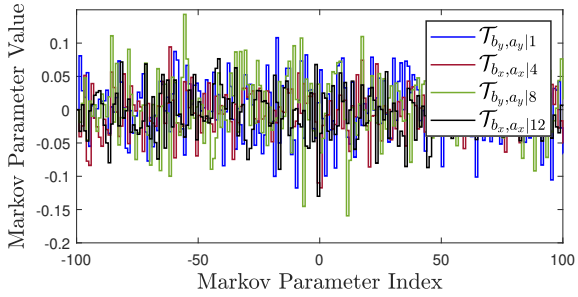

Fig. 3.41 Estimated Markov parameters from the pseudo input a to the pseudo output b, where in each operator the active actuator is $1, 4, 8$, or 12. The estimated Markov parameters are obtained using the least squares with a noncausal FIR model with $r = 100$ and $d = 100$.

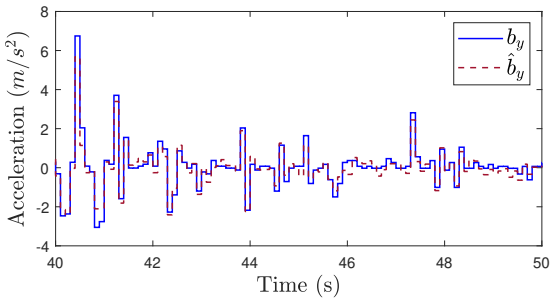

Fig. 3.42 Simulated output and predicted output of b_y, where the predicted output is obtained using the identified transmissibility operator $\mathscr{T}_{b_y,a_y|1}$ and the measurement of a_y.

Loss of Effectiveness (Creep Fault)

All screws in the setup are relativity loosen so that the middle stage can move freely in both directions. To implement this fault, we fasten the screws on the actuators #4 and #9 so that they become harder to move. We run the setup by applying a random input voltage to actuators #4 and #9 separately. The loss of effectiveness fault is introduced in both actuators at time 80 seconds. Figure 3.43 shows the norm of residual for the operators $\mathscr{T}_{a_x,b_x|4}$ and $\mathscr{T}_{a_x,b_x|9}$. Note from Figure 3.43 that at $t = 80$ seconds the level of the norm of the residuals of $\mathscr{T}_{a_x,b_x|4}$ and $\mathscr{T}_{a_x,b_x|9}$ changes, and thus we conclude that the fourth and ninth actuators are faulty. Similarly, the loss of effectiveness fault is applied to actuators #5, #7, #12 and #1, and the norm of residuals are shown in Figures 3.44 and 3.45.

Fatigue Crack

Fatigue cracks are difficult to implement in the experimental work without making permanent defects. In this experiment, we consider the fatigue crack as a change in the stiffness only. We fasten the spring rings with each others in actuators #4 and #9 so that the tension stiffness increases and the compression stiffness remains the same. We run the setup by applying a random input voltage to actuators #4 and #9 separately. Moreover, the fatigue crack fault is introduced in both actuators at time 80 seconds. Figure 3.43 shows the norm of residual for the operators $\mathscr{T}_{a_x,b_x|4}$ and $\mathscr{T}_{a_x,b_x|9}$. Note from Figure 3.43 that at $t = 80$ seconds the level of the norm of the residuals of $\mathscr{T}_{a_x,b_x|4}$ and $\mathscr{T}_{a_x,b_x|9}$ changes, and thus we conclude that the fourth and ninth actuators are faulty. Similarly, the fatigue crack is applied to the actuators #5, #7, #12 and #1, and the norm of residuals are shown in Figures 3.44 and 3.45.

Actuator Delay

For further validation of the proposed method, we consider testing actuator delay faults [77]. Actuator delay faults can be represented as an increase in the equivalent damping coefficient $C_{a,i}$ in the actuator dynamics, which results in a higher settling time of the actuator response [77]. This fault is emulated experimentally by adding a viscous fluid (wet glue) to the actuator rod, which leads to a higher friction. We run the setup by applying a random input voltage to actuators #4 and #9 separately, and the actuator delay fault is introduced in both actuators at time 80 seconds. Figure 3.46 shows the norm of the residuals for the operators $\mathscr{T}_{a_x,b_x|4}$ and $\mathscr{T}_{a_x,b_x|9}$. Note from Figure 3.46 that at $t = 80$ seconds the level of the norm of the residuals of $\mathscr{T}_{a_x,b_x|4}$ and $\mathscr{T}_{a_x,b_x|9}$ changes, and thus we conclude that the fourth and ninth actuators are faulty.

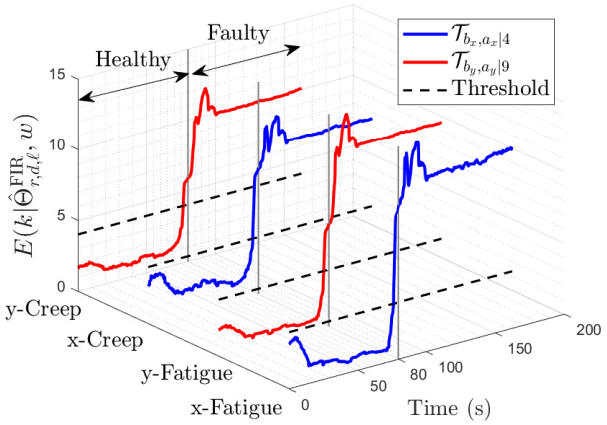

Fig. 3.43 Norm of the residuals of the transmissibilities $\mathcal{T}_{b_x,a_x|4}$ and $\mathcal{T}_{b_y,a_y|9}$ of the experimental setup computed using (5.30) with $w = 100$ steps. Note that at $t = 80$ seconds the level of the norm of the residual change, and thus we conclude that the active actuator is faulty.

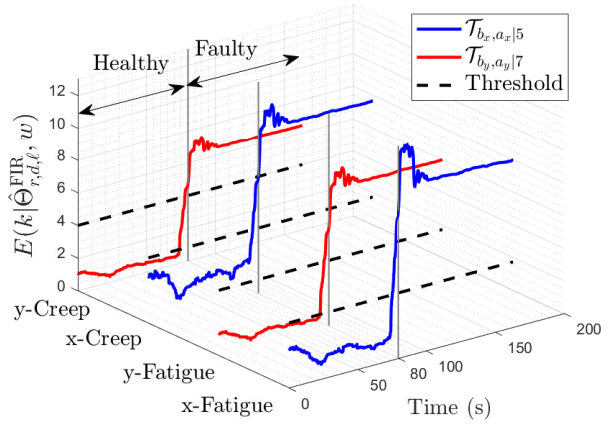

Fig. 3.44 Norm of the residuals of the transmissibilities $\mathcal{T}_{b_x,a_x|5}$ and $\mathcal{T}_{b_y,a_y|7}$ of the experimental setup computed using (5.30) with $w = 100$ steps. Note that at $t = 80$ seconds the level of the norm of the residual change, and thus we conclude that the active actuator is faulty.

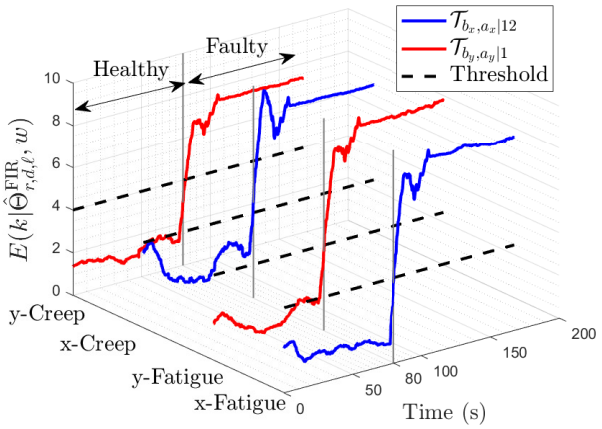

Fig. 3.45 Norm of the residuals of the transmissibilities $\mathcal{T}_{b_x,a_x|12}$ and $\mathcal{T}_{b_y,a_y|1}$ of the experimental setup computed using (5.30) with $w = 100$ steps. Note that at $t = 80$ seconds the level of the norm of the residual change, and thus we conclude that the active actuator is faulty.

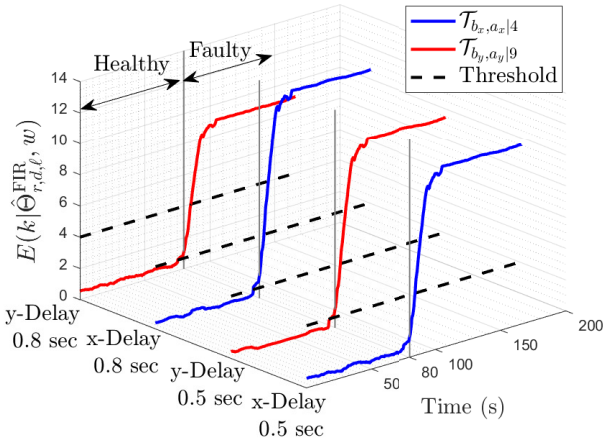

Fig. 3.46 Norm of the residuals of the transmissibilities $\mathcal{T}_{b_x,a_x|4}$ and $\mathcal{T}_{b_y,a_y|9}$ of the experimental setup with actuator delay fault. Note that at $t = 80$ seconds the level of the norm of the residual change, and thus we conclude that the active actuator is faulty.

Chapter 4

Transmissibility-based Sliding Mode Control

4.1 Controller Design

Consider a fault in the system (3.1)-(3.2) that diverge the measured output y_{o} from the estimated output $\hat{y}_{\mathrm{o}}$. This causes an increase in the norm of residual to a level higher. Assume that the system operates in a healthy manner for the first M steps, where $M \geq w$, and let η be the signal-to-noise ratio, then define the threshold

$$\mu(\hat{\Theta}, w, M) \triangleq \frac{\eta}{M+1} \sum_{i=0}^{M} E(i, w). \tag{4.1}$$

If the norm of residual exceeds the threshold limit the system is considered to be faulty. The proposed control technique then mitigates the fault effects and derive the residual back to zero. Let the following represents the discrete form of the system model in (3.1)-(3.2)

$$x(k+1) = \mathscr{A}x(k) + \mathscr{B}u(k), \tag{4.2}$$

$$y_{\mathrm{i}}(k) \triangleq C_{\mathrm{i}}x(k) + D_{\mathrm{i}}u(k), \tag{4.3}$$

$$y_{\mathrm{o}}(k) \triangleq C_{\mathrm{o}}x(k) + D_{\mathrm{o}}u(k), \tag{4.4}$$

where $\mathscr{A}$ and $\mathscr{B}$ are the equivalent state and input matrices in the discrete time. The controlled system model can then be described by

$$x(k+1) = \mathscr{A}x(k) + \mathscr{B}(u(k) - \vartheta(k)), \tag{4.5}$$

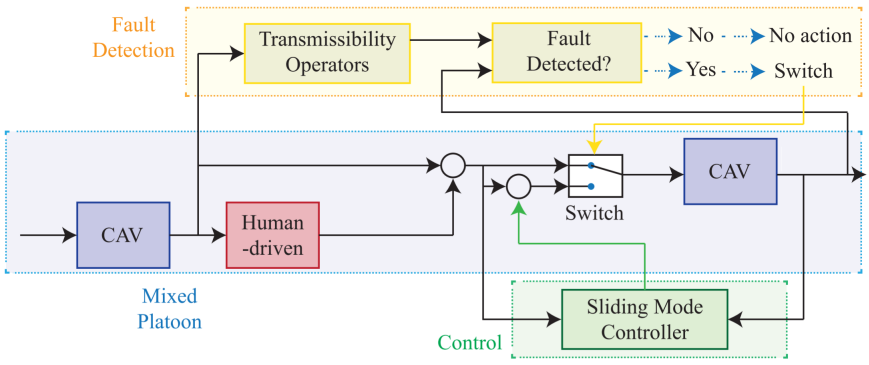

Fig. 4.1 An example of the implementation of sliding mode controller on Connected Autonomous Vehicle (CAV) platoons.

where ϑ is the control signal. The control signal is designed to force the residual e to go into the sliding band, which is a quasi-sliding mode. To align with the sliding mode control literature such as, the condition $e(k)\Delta e(k) < 0$ has to be satisfied, where $\Delta e(k) = e(k+1) - e(k)$. To satisfy the condition $e(k)\Delta e(k) < 0$, the control law ϑ should be defined as

$$\vartheta(k) = \begin{cases} \vartheta^{+}(k), & e(k) > 0, \\ \vartheta^{-}(k), & e(k) < 0, \end{cases} \tag{4.6}$$

where ϑ^{+} is a control law that ensures $\Delta e < 0$, and similarly ϑ^{-} is a control law that ensures $\Delta e > 0$. A super-twisting sliding mode control to recover the performance of the system is considered. The super-twisting sliding mode control allows to deal with perturbations growing linearly in e. For all $k > 0, E \geq \mu$, i.e. system is faulty, the control signal is defined as

$$\vartheta(k) = \text{sat}\Big[- \mathscr{P} |e(k)|^{\frac{1}{2}} \text{sgn}(e(k)) - \frac{1}{2} \mathscr{M} \sum_{i=0}^{k} \text{sgn}(e(i)) \Big], \tag{4.7}$$

where $\mathscr{M}$ and $\mathscr{P}$ are constants that indicate how the states will go into the sliding band. The control signal ϑ is saturated to eliminate the chattering effect. The stability analysis will further be discussed in the final thesis. Figure 4.1 shows an example of applying the sliding mode controller on a platoon of mixed Connected Autonomous Vehicle (CAV) and human-driven vehicles.

4.2 Stability

This section investigates stability after the actuator faults are mitigated using the control signal in (6.43) as explained in the following proposition.

Proposition 1. Consider the system (A.10)-(A.11) with Hurwitz A, and assume that Assumption 2 holds. Then, under bounded actuator faults and the faults being mitigated using the control law in (6.43), the designed control system always holds stability.

Proposition 1 Proof. Define the relationship from the active actuator input f_i to the output a_x

$$\mathscr{G}(\mathbf{p}) = C_{a_x}(\mathbf{p}I - A)^{-1}\bar{B}_i. \tag{4.8}$$

Note that $\mathscr{G}$ is stable since A is Hurwitz. The actuator input f_i can be obtained from the output a_x by discretizing the inverse of $\mathscr{G}$, that is, $f_i(k) = \mathscr{G}^{-1}(\mathbf{q})a_x(k)$. The relationship from the output a_x to the output subset b can be represented as

$$\hat{x}(k+1) = \mathscr{A}\hat{x}(k) + \mathscr{B}(\mathscr{G}^{-1}(\mathbf{q})a_x(k)), \tag{4.9}$$

$$\hat{b}(k) \triangleq C_b\hat{x}(k). \tag{4.10}$$

Note that (4.9), (4.10) is a representation of the transmissibilty from a_x to b. Thus, using Assumption 2, (4.9), (4.10) is stable and thus $\hat{b}$ is bounded.

Subtracting (4.9) from (6.42) yields the error model

$$\varepsilon(k+1) = \mathscr{A}\varepsilon(k) - \mathscr{B}\vartheta(k), \tag{4.11}$$

where $\varepsilon(k) = \begin{bmatrix} \varepsilon_1(k) & \dots & \varepsilon_s(k) \end{bmatrix}^{\mathrm{T}}$, and for all $j \in \{1,\dots,s\}$, ε_j is the error in the jth state. The plant stability can be directly be investigated from (4.11) since the system is linear. From the right-hand-side of the error model in (4.11), $\mathscr{A}$ is stable since the system holds stability by the design of the Hurwitz state matrix A in (A.10), and thus $\mathscr{A}\varepsilon$ is bounded. Moreover, the control signal ϑ is bounded since it is saturated to eliminate the chattering effect, and thus, the term $\mathscr{B}\vartheta$ is bounded. Therefore, the estimation residual e can be represented as

$$\begin{aligned} e(k) &\triangleq b(k) - \hat{b}(k) \\ &\triangleq C_b[x(k) - \hat{x}(k)] = C_b\varepsilon(k), \end{aligned} \tag{4.12}$$

which indicates the linear relation between ε and e, i.e. e is stable as long as ε is stable. □

It was shown and proved in [29, 40] based on Lyapunov stability analysis that the super-twisting algorithm in (6.43) will force the states to go into the sliding band as long as the system attain the plant stability. That is, the residual will exponentially decay to zero in finite time.

4.3 Experiment 1: CAV Platoons Fault-tolerant Control

4.3.1 Numerical Example

To test the proposed approach numerically, we construct a platoon with five vehicles where the third $i_{\mathrm{H}} = 3$ is human-driven, and the rest are CAVs. We consider all CAVs to follow the bond graph model shown in Figure A.1 along with the parameters in Table A.2. The unknown human-driver behavior is emulated by considering the IDM model in Appendix A.1.2. The desired velocity of the platoon was set to band-limited white noise with zero mean and unit variance, and an initial condition of $5m/s$ for all vehicles. For $j \in \{3,4,5\}$ let $\mathscr{T}_j$ denote the transmissibility operator with the pseudo inputs v_{j-2}, v_{j-1} and the pseudo output v_j. Note that v_j occurs in a timely-manner after v_{j-1} and v_{j-2}, thus we can consider $\mathscr{T}_j$ causal. Figure 4.2 shows the estimated Markov parameters of the operator $\mathscr{T}_4$ identified with $r = 50$ and $d = 0$. The operator $\mathscr{T}_4$ is then implemented along with the measurements of v_2 and v_3 to obtain an estimation of the velocity v_4 under healthy conditions as shown in Figure 4.3. Note from Figure 4.2 that the simulated output velocity of the identified causal transmissibility is accurate, which confirms that the noncausal part of the model can be neglected.

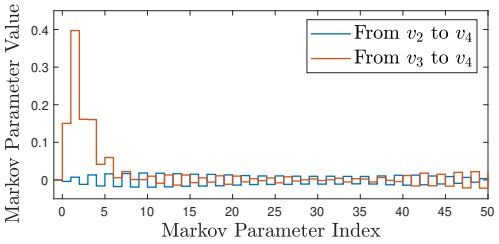

Fig. 4.2 Simulation results: Estimated Markov parameters of the transmissibility operator $\mathscr{T}_4$ obtained using least squares with a causal FIR model with $r = 50$ and $d = 0$.

We introduce next the three fault examples from Appendix B.1 to the system separately. The sensor fault by setting $\delta_{s,i_{\mathrm{H}}}$ to a pulse signal with random amplitude and sampling time T_s with $t^* = 70$ and the constants in Table A.2. In a similar way, we emulated the burst transmission and DoS attacks in the communication link between the second and fourth vehicles. The burst transmission was emulated by setting $\tilde{s}_2$ to band-limited white noise,

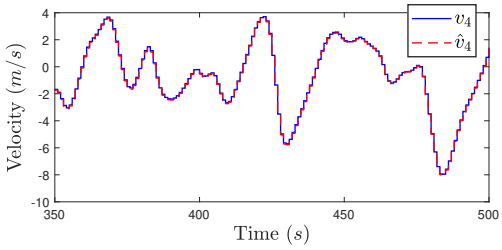

Fig. 4.3 Simulation results: The simulated output velocity v_4 and the predicted output velocity $\hat{v}_4$. The predicted velocity is obtained using the identified transmissibility operator $\mathscr{T}_4$ with the estimated Markov parameters shown in Figure4.2 and measurements of v_2 and v_3.

$\varepsilon_1 = \varepsilon_2 = 1$, $\zeta_1 = 0$, and $\zeta_2 = 1$. The DoS attack was emulated by setting $\tau_{v,2} = 2$ seconds. All faults are introduced separately at time $t = 70$ seconds. The presence of faults in the platoon leads to higher estimation error as shown in the top part of Figure 4.18. Notice the jump in the cost function Figure 4.18 around time 70 when the the faults occurred. The cost then drops down to zero as the faults are being mitigated. Figure 4.19 shows the norm of the residuals of the transmissibilities $\mathscr{T}_4$ and $\mathscr{T}_5$ computed using (5.30) with $w = 100$ steps. Note that at approximately $t = 75$ seconds, the norm of the residuals exceeds the threshold limit, which activates the sliding mode controller. At time $t = 70$ seconds, the norm of the residuals of the operators drops below the threshold limit due to using the sliding mode control.

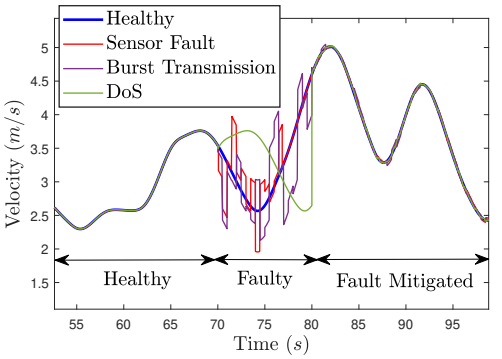

Fig. 4.4 Simulation results: Measured and predicted values of v_4. At $t = 70$ seconds the fault scenarios are introduced, which led to the deviation from the healthy signal. At time $t = 75$ seconds, the sliding mode controller is activated which forced the faulty responses to slide along the healthy prediction.

4.3.2 Experimental Test

We consider the experimental setup shown in Figure 7.7 consisting of three autonomous Quanser QBot2e robots. Each robot consists of two coaxial wheels (driven by DC motors).

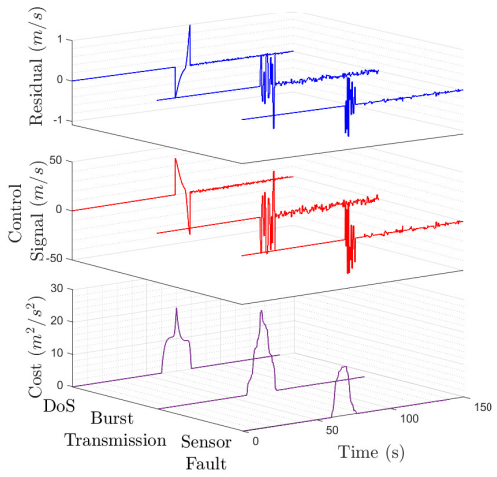

Fig. 4.5 Simulation results: Prediction residuals and the fault mitigation control signals. At $t = 70$ seconds the faults were introduced separately, which led to the shown prediction residuals. At time $t = 75$ seconds, the sliding mode controller is activated and the shown control signals are produced. Notice the jump in the cost function of around time 70 when the faults occurred. The cost then drops down to zero as the faults are being mitigated.

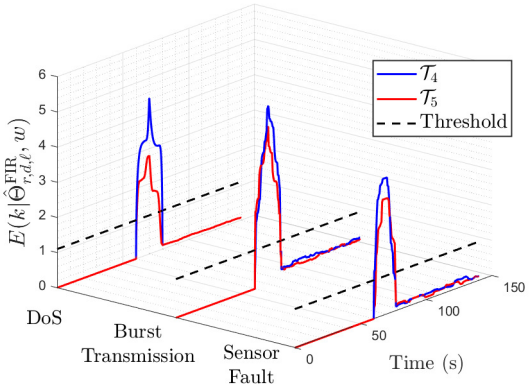

Fig. 4.6 Simulation results: Norm of the residuals of the transmissibilities $\mathscr{T}_4$ and $\mathscr{T}_5$ computed using (5.30) with $w = 100$ steps. Note that at approximately $t = 55$ seconds, the norms of the residuals of $\mathscr{T}_4$ and $\mathscr{T}_5$ exceed the threshold limit, which activates the sliding mode controller. Moreover, note that after activating the sliding mode controller the norm of the residual drops below the threshold value.

The variance between the wheels' velocities gives angular velocity for the robot. The first robot receives the excitation signal from a computer through a wireless connection. The second robot is human-driven through a wireless controller. The third robot receives the first robot velocity v_1 via V2V communication and measures the second robot velocity v_2 using an onboard depth sensor.

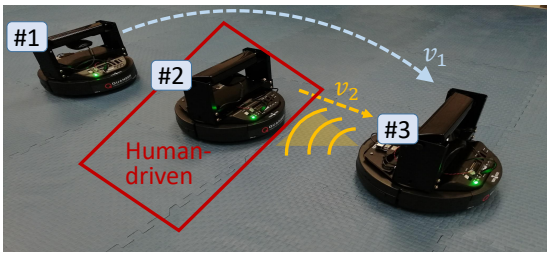

Fig. 4.7 Experimental setup: The first robot receives the excitation signal from a computer through a wireless connection. The second robot is human-driven through a computer keyboard. The third robot receives the first robot velocity v_1 via V2V communication and measures the second robot velocity v_2 using an onboard depth sensor.

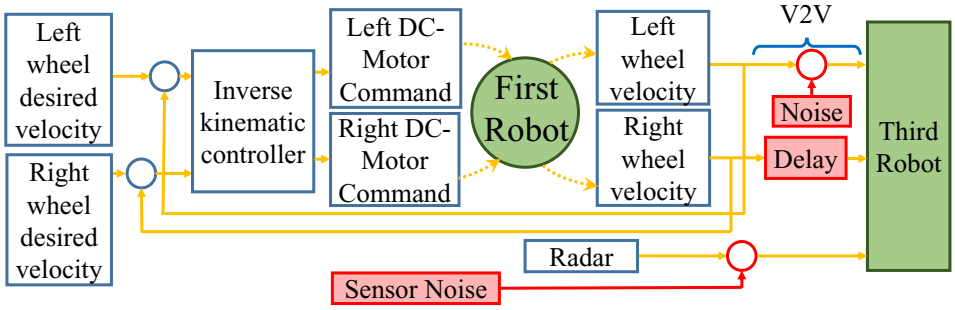

Fig. 4.8 Experimental emulation of the platoon faults. Three faults are introduced individually, as represented by the red blocks. The sensor noise is a physical fault that is represented by adding disturbances to the measured human-driven velocity. The cyber faults are represented by injecting noise and delay to the information packet in the V2V communication link that is recieved by the third robot.

For health monitoring, we consider a one-dimensional motion for the platoon. We first run the setup by sending a zero-mean, unit variance, Gaussian random excitation signal to the first robot. Note that using a noncausal FIR model of the transmissibility results in a delay in the predicted output of the transmissibility. Therefore, to avoid delays in the closed-loop system due to using a noncausal model of the transmissibility, we use causal FIR models to identify the transmissibilities. We use least squares with a causal FIR model with $r = 50$ and $d = 0$ to identify the transmissibility operator $\mathscr{T}_3$, which is the transmissibility from robots 1 and 2 to robot 3. The estimated Markov parameters for the transmissibility operator $\mathscr{T}_3$ are shown in Figure 4.9. Then, the estimated transmissibility is used along with the measurements of v_1 and v_2 to obtain an estimate of the velocity v_3 as shown in Figure 4.10.

Sensor fault

We consider injecting the band-limited white noise signal shown in Figure 4.11 in the depth sensor (radar) of the third robot as shown in Figure 4.8. Next, the estimated transmissibilities

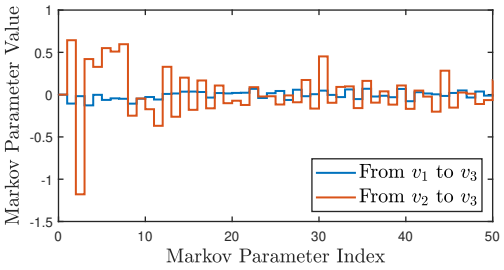

Fig. 4.9 Experimental results: Estimated Markov parameters for the transmissibility operator $\mathscr{T}_3$ obtained using least squares with a causal FIR model with $r = 50$ and $d = 0$.

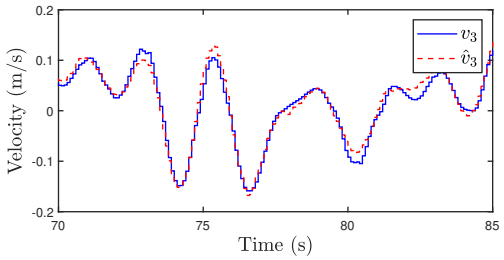

Fig. 4.10 Experimental results: The measured output velocity of the third robot v_3 and the predicted output velocity $\hat{v}_3$, where the predicted velocity is obtained using the identified transmissibility operator $\mathscr{T}_4$ whose Markov parameters are shown in Figure 4.9 and measurements of v_1 and v_2.

are used with the measurements of v_1 and v_2 to obtain an estimate of the velocity v_3 as shown in Figure 4.12 before $t = 50$ seconds. At $t = 50$ seconds, the noise is injected, which results in the residual shown in the first part of Figure 4.13. At $t = 53$ seconds, the cumulative error exceeds the threshold limit as shown in Figure 4.15. This activates the sliding mode controller, which produces the control signal shown in the second part of Figure 4.13. Note that after $t = 53$ seconds, the controller is activated and the measured velocity is close to the predicted velocity.

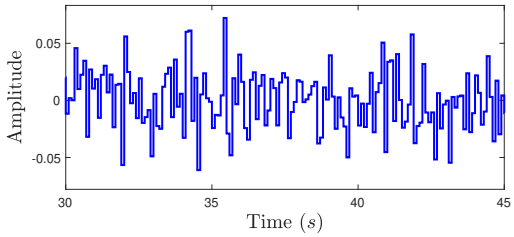

Fig. 4.11 A noise signal that is used to emulate the sensor fault experimentally. This noise signal is injected in the radar measurements and the V2V noise in Figure 4.8.

Cyberattack and time-delay faults

Similar results can be obtained for the cyberattack and time-delay faults, which we apply individually. For the cyberattack, a noise signal is injected into the communication link between robot 1 and robot 3 as shown in Figure 4.8. For the time-delay fault, we consider the case of 2 seconds of time delay applied to the communication link. Next, the estimated transmissibility is used with the measurements of v_1 and v_2 to obtain an estimate of the velocity v_3 as shown in the first part of Figure 4.12 for $t < 50$ seconds. At $t = 50$ seconds, the cyberattack and time delay faults are introduced, which leads to the prediction error shown in the first part of Figure 4.13. At $t = 53$ seconds, the cumulative errors for the cyber-attack and time delay exceed the threshold limits as shown in Figure 4.15. This activates the sliding mode controller, which produces the control signals shown in the second part of Figure 4.13. Note that after $t = 53$ seconds, the controller is activated and the measured velocity is close to the predicted velocity. Figure 4.14 shows the cost function of the experimental residuals under the three proposed faults. We can see that the cost function before time 50 seconds when the setup was healthy had a low level. After introducing the system faults 50 seconds, the three costs jumped to a high level. The sliding mode controller is then activated, and forced to cost to slide back to zero.

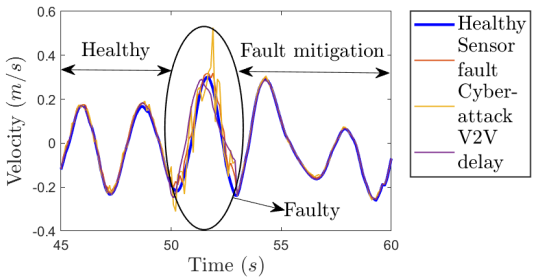

Fig. 4.12 Experimental results: Measured and predicted values of v_3. At $t = 50$ seconds the fault scenarios are introduced, which led to the deviation from the healthy signal. At time $t = 53$ seconds, the sliding mode controller is activated, which recovers the healthy performance of the vehicle.

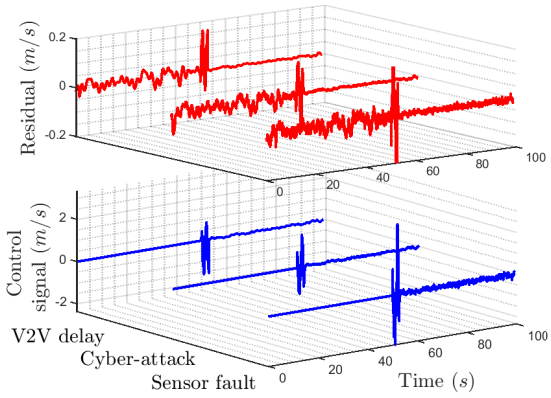

Fig. 4.13 Experimental results: Prediction residuals and the fault mitigation control signals. At $t = 50$ seconds the faults were introduced individually, which led to the jump in the shown prediction residuals. At time $t = 53$ seconds, the sliding mode controller is activated and the shown control signals are produced.

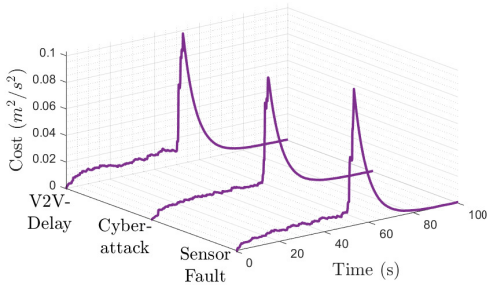

Fig. 4.14 Experimental results: Cost function of the experimental residuals under the three proposed faults. The cost function levels are low before time 50 seconds while the setup is healthy. The faults at time 50 seconds led to jumps in the costs. The sliding mode controller is then activated and forced the cost to slide back to zero.

4.4 Experiment 2: Application on Multi-Actuator Systems, Numerical Example

4.4.1 System Model and Transmissibility Construction

The parameters shown in Table A.2 are used to construct the system (A.10), (A.11) in Figure A.3 with $n = 12$ actuators to characterize the reticle stage with multi-piezoelectric actuators. We consider a square rigid middle stage as the reticle stage with length $l = 0.132$ m and 3 actuators on each side of the middle stage, that is, $m_x = 3, n_x = 6$, and $m_y = 9$. We consider actuators #1, #3, #4, #6, #7, #9, #10, #12 to be on the stage corners and actuators #2, #5, #8, #11 to be aligned with the stage's center of mass, that is, $\alpha_1 = 45^o, \alpha_2 = 0^o, \alpha_3 =$

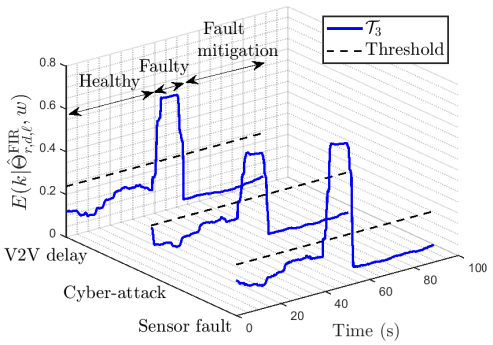

Fig. 4.15 Experimental results: Norm of the transmissibility residuals of $\mathcal{T}_3$ computed using (5.30) with $w = 100$ steps. Note that at approximately $t = 50$ seconds, the norm exceeds the threshold limit, which activates the sliding mode controller. The figure shows that after activating the sliding mode controller the norm drops below the threshold value.

$315^o, \alpha_4 = 135^o, \alpha_5 = 180^o, \alpha_6 = 225^o, \alpha_7 = 45^o, \alpha_8 = 90^o, \alpha_9 = 135^o, \alpha_{10} = 315^o, \alpha_{11} = 270^o, \alpha_{12} = 225^o$. Moreover, $l_1 = l_3 = l_4 = l_6 = l_7 = l_9 = l_{10} = l_{12} = 0.0934$ m, and $l_2 = l_5 = l_8 = l_{11} = 0.066$ m. Furthermore, we set $\alpha_a = 180^o, \alpha_b = 45^o, l_a = 0.06$ m, and $l_b = 0.09$ m.

We start by identifying the transmissibility operator, $\mathcal{T}_{b,a|3}$ which is the transmissibility operator from point b to point a with $r = 25$. Note that the model (A.10)-(A.11) along with the parameters in Table A.2 satisfies Assumption 1, and thus the causal transmissibility is valid. Figure 5.11 shows the Markov parameters of the causal transmissibility operator $\mathcal{T}_{b,a|3}$. To validate the accuracy of the identified parameters of the transmissibility operator $\mathcal{T}_{b,a|3}$, Figure 4.16(b) shows the measured and estimated displacements of point b. Notice that the identified transmissibility operator $\mathcal{T}_{b,a|3}$ along with the measured displacement at point a results in a good estimation of $\hat{b}$.

Table 4.1 Simulation parameters for the multi-actuator system in (A.10)-(A.11).

Parameter	Description	Value
M_p	Middle stage mass	$2.45kg$
J	Middle stage moment of inertia	$0.0997kg.m^2$
l	Middle stage length	$0.132m$
$m_{a,i}$	Actuator mass	$0.028kg$
$k_{a,i}$	Actuator stiffness	$100 \times 10^6 N/m$
$C_{a,i}$	Actuator damping	$2681.13N.s/m$
$k_{h,i}$	Hinge stiffness	$2 \times 10^4 N/m$
$C_{h,i}$	Hinge damping	$500N.s/m$

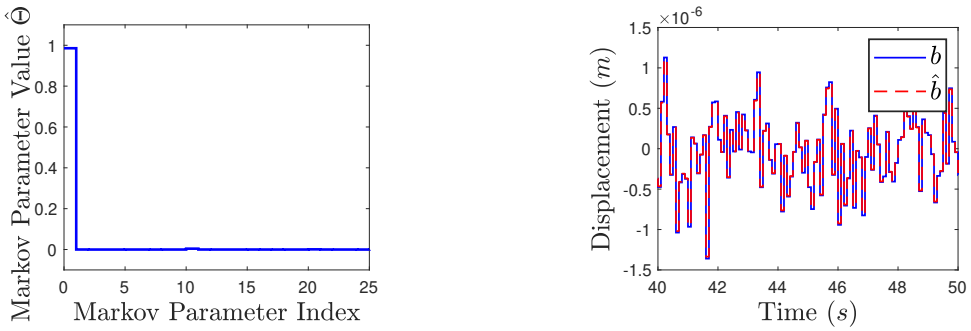

((a)) ((b))

Fig. 4.16 Simulation results: (a) Estimated Markov parameters from the pseudo input b to the pseudo output a used for fault mitigation. The estimated Markov parameters were identified using noncausal FIR model with $r = 25$. (b) Measurements of b and its transmissiblity-based estimation under healthy conditions to validate the identification of $\mathscr{T}_{b,a|3}$.

4.4.2 Health Monitoring

Next, the estimated transmissibility is used along with the displacement measurements at the point b to obtain an estimate of the displacement at a as shown in Figure 4.17. At $t = 100$ seconds, the loss of effectiveness was introduced, which led to the prediction error shown in the upper part of Figure 4.18. Figure 4.19 shows the norm of residual E of the posteriori error (after the fault is mitigated) over a moving window with width $w = 100$. Note that, the time in Figure 4.19 is delayed by 100 steps (10 seconds) due to the moving window. As shown in Figure 4.19, at $t = 103$ seconds the error norm exceeded the threshold limit and thus the sliding mode controller was activated. The controller parameters $\mathscr{P} = 77000$ and $\mathscr{M} = 12$ were tuned such that the controller has a sufficient convergence rate to the sliding surface and the control signal is within the actuator capability. The sliding mode controller injected the control signal shown in the lower part of Figure 4.18, which led to the drop in the error norm below the threshold limit.

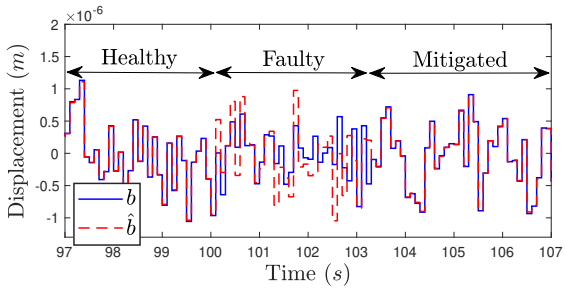

Fig. 4.17 Simulated output displacement and predicted output displacement at point a. At time $t = 100$ seconds the loss of effectiveness was emulated and this led to the error e shown in Figure 4.18. At time $t = 103$ seconds, the sliding mode controller is activated and the control signal ϑ shown in Figure 4.18 is produced.

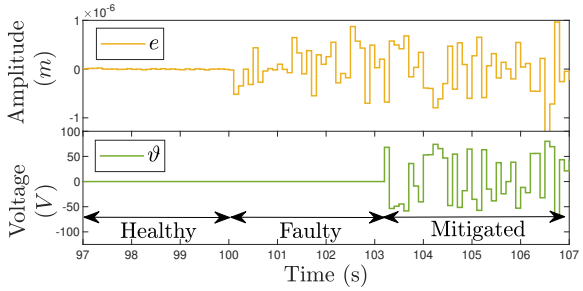

Fig. 4.18 The prediction error e and the control signal ϑ produced from the sliding mode controller. A loss of effectiveness fault is emulated in actuator 3 at time $t = 100$ seconds. The prediction error reached the threshold limit at time 103 seconds, which activated the sliding mode controller and produced the control signal ϑ.

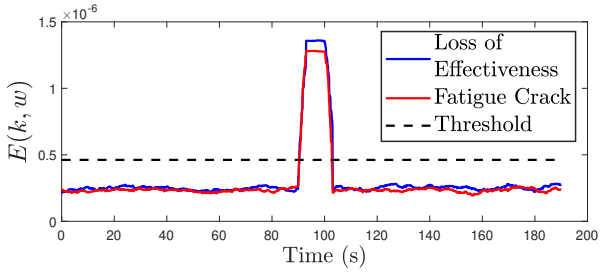

Fig. 4.19 Norm of the residuals of the transmissibility $\mathscr{T}_{a,b|3}$ computed using (5.30) with $w = 100$ steps for the simulations of loss of effectiveness and fatigue crack in actuator 3. Note that at approximately $t = 100$ seconds, the norm of residual of both reached the threshold limit, which activates the sliding mode controller. Moreover, note that after activating the sliding mode controller, the norm of the residual dropped below the threshold value for both faults.

Chapter 5

Time-variant Transmissibility

5.1 Time-variant Transmissibility Operators

Consider the following time-varying state space model

$$\dot{x}(t) = A(t)x(t) + B_u(t)u(t) + B_f(t)f(t,x), \tag{5.1}$$
$$y(t) = C(t)x(t) + D_u(t)u(t) + D_h(t)h(t,x), \tag{5.2}$$

where $A(t) \in \mathbb{R}^{n\times n}$ is Hurwitz, $B_u(t) \in \mathbb{R}^{n\times(m-2)}, B_f(t) \in \mathbb{R}^{n\times 1}, C(t) \in \mathbb{R}^{p\times n}$, $D_u(t) \in \mathbb{R}^{p\times(m-2)}, D_h(t) \in \mathbb{R}^{p\times 1}, n$ is the system order, m is the number of excitation signals, and $p > m$ is the number of measured outputs. All nonlinearities and unmodeled dynamics are pushed to the unknown bounded functions $f(\cdot,\cdot)$ and $h(\cdot,\cdot)$. Let $B(t) = [B_u(t) \;\; B_f(t) \;\; 0]^{\mathrm{T}}$, and $D(t) = [D_u(t) \;\; 0 \;\; D_h(t)]^{\mathrm{T}}$, then define the two independent output subsets

$$y_{\mathrm{i}}(t) = C_{\mathrm{i}}(t)x(t) + D_{\mathrm{i}}(t)\bar{u}(t,x), \tag{5.3}$$
$$y_{\mathrm{o}}(t) = C_{\mathrm{o}}(t)x(t) + D_{\mathrm{o}}(t)\bar{u}(t,x), \tag{5.4}$$

where $\bar{u}(t,x) = [u(t) \;\; f(t,x) \;\; h(t,x)]^{\mathrm{T}}$,

$$y(t) = \begin{bmatrix} y_{\mathrm{i}}(t) \\ y_{\mathrm{o}}(t) \end{bmatrix}, C(t) = \begin{bmatrix} C_{\mathrm{i}}(t) \\ C_{\mathrm{o}}(t) \end{bmatrix}, D(t) = \begin{bmatrix} D_{\mathrm{i}}(t) \\ D_{\mathrm{o}}(t) \end{bmatrix},$$

and $C_{\mathrm{i}}(t) \in \mathbb{R}^{m\times n}, C_{\mathrm{o}}(t) \in \mathbb{R}^{(p-m)\times n}, D_{\mathrm{i}}(t) \in \mathbb{R}^{m\times m}$, and $D_{\mathrm{o}}(t) \in \mathbb{R}^{(p-m)\times m}$. Note that the definitions of B, D_{i}, and D_{o} here consider the functions $f(\cdot,\cdot)$ and $h(\cdot,\cdot)$ as independent excitation signals that act on the system. This renders the transmissibility operator independent of the input signal u and the unmodeled dynamics $f(\cdot,\cdot), h(\cdot,\cdot)$.

Assumption. The parameter variation in equations (7.1)-(5.2) is assumed to vary randomly within known lower and upper limits.

This assumption is most likely to be satisfied in most systems. For example, consider a robot arm that picks objects with different mass values. The robot arm in this case will have a maximum allowable mass due to the structural design of the arm, the material of the arm, and the limited actuator effectiveness.

In [8], frequency domain transmissibilities were shown to depend on the input signal u in case of non-zero initial conditions. On the other hand, time-domain transmissibilities were obtained in [8] by replacing the Laplace variable s with the differentiation operator $\mathbf{p}$, and were shown to be independent of the input signal u and the initial conditions. Following [8], we consider time-varying transmissibility operators in the $\mathbf{p}$ domain. Define,

$$\Gamma_{\mathrm{i}}(t,\mathbf{p}) \triangleq C_{\mathrm{i}}(t)\mathrm{adj}(\mathbf{p}I - A(t))B(t) + D_{\mathrm{i}}(t)\delta(t,\mathbf{p}), \tag{5.5}$$

$$\Gamma_{\mathrm{o}}(t,\mathbf{p}) \triangleq C_{\mathrm{o}}(t)\mathrm{adj}(\mathbf{p}I - A(t))B(t) + D_{\mathrm{o}}(t)\delta(t,\mathbf{p}), \tag{5.6}$$

$$\delta(t,\mathbf{p}) \triangleq \det[\mathbf{p}I - A(t)]. \tag{5.7}$$

Γ_{i} and Γ_{o} are two matrices of polynomials of $\mathbf{p}$ whose zeros are zeros of the two output channels y_{i} and y_{o}, respectively. δ is the characteristics equation in terms of $\mathbf{p}$, whose zeros are the poles of the original system (7.1)-(5.2). Then the transmissibility operator from y_{i} to y_{o} satisfies [8]

$$y_{\mathrm{o}}(t) = \mathscr{T}(t,\mathbf{p})y_{\mathrm{i}}(t), \tag{5.8}$$

where

$$\mathscr{T}(t,\mathbf{p}) \triangleq \Gamma_{\mathrm{o}}(t,\mathbf{p})\Gamma_{\mathrm{i}}^{-1}(t,\mathbf{p}).$$

Note that $\mathscr{T}$ is independent of the input signal u and the unmodeled dynamics f,h. This renders the proposed approach robust against any effects that can be included in f or h such as system nonlinearities, system noise, or external disturbances. However, the uncertainties that can be included in f and h are limited to the number of available independent output measurements in y_{i}. The total number of signals that the proposed approach can be robust against is the same as the number of signals included in y_{i}. That is, the number of signals in u, f, and h combined should equal the number of signals in y_{i}. This is required to ensure the invertability of Γ_{i}. The number of rows in Γ_{i} is the same as the number of signals in y_{i}, while the number of columns in Γ_{i} is the same as the number of signals in u, f, and h combined.

This indicates that the more available sensor measurements in the system, the more robust the developed approach is.

If the variation in the underlying system's parameters is small, then a time-invariant model of the transmissibility operator in (5.8) can give an acceptable approximation of $\mathscr{T}$ since $\mathscr{T}$ is robust against f,h. However, for significant changes in the underlying system's parameters, a time-varying model of the transmissibility operator in (5.8) is required.

Since sensor measurements are obtained in discrete time, we consider discrete-time transmissibility operators in the forward-shift operator $\mathbf{q}$, that is, we replace $\mathbf{p}$ in (5.8) by the forward shift operator $\mathbf{q}$ [89]. Replacing $\mathbf{p}$ in (5.8) with $\mathbf{q}$ yields, for all $k \geq 0$,

$$y_{\mathrm{o}}(k) = \mathscr{T}(k,\mathbf{q})y_{\mathrm{i}}(k), \tag{5.9}$$

where

$$\mathscr{T}(k,\mathbf{q}) = \Gamma_{\mathrm{o}}(k,\mathbf{q})\Gamma_{\mathrm{i}}^{-1}(k,\mathbf{q}) \tag{5.10}$$

$$= \frac{1}{\det\Gamma_{\mathrm{i}}(k,\mathbf{q})}\Gamma_{\mathrm{o}}(k,\mathbf{q})\mathrm{adj}\Gamma_{\mathrm{i}}(k,\mathbf{q}). \tag{5.11}$$

Note that if the transmissibility output channel has more zeros than the transmissibility input channel, then $\mathscr{T}(k,\mathbf{q})$ is noncausal. Moreover, if the transmissibility output channel has a non-minimum phase zero (unstable zero), then $\mathscr{T}(k,\mathbf{q})$ is unstable. Furthermore, in most cases, the variation in the system's parameters A,B,C,D is unknown. To this end and following [6], we consider identifying the transmissibility operator $\mathscr{T}(k,\mathbf{q})$ using noncausal FIR models. A noncausal FIR model of $\mathscr{T}$ is a truncation of the Laurent expansion of $\mathscr{T}$ in an analytic annulus that contains the unit circle. Noncausal FIR models are always stable, independent of the system order, and can simulate unstable and noncausal transmissibilities. In the next section, we extend the least-squares identification introduced in [6] to recursive least squares to count for the unknown varying parameters in A,B,C,D.

5.2 Transmissibilities Recursive Least Squares Identification

The time-varying noncausal FIR model can be given for all $k \geq 0$ by

$$\mathscr{T}(k,\mathbf{q}) = \sum_{i=-d}^{r} H_i(k)\mathbf{q}^{-i}, \tag{5.12}$$

where r, d denote the order of the causal and noncausal parts of the FIR model of $\mathscr{T}$, respectively, and are further explained in Section 5.2.1. $H_i(k) \in \mathbb{R}^{(p-m)\times m}$ is the i-th coefficient of the Laurent expansion of $\mathscr{T}$ in the annulus that contains the unit circle. H_i can be derived from $\Gamma_{\mathrm{i}}, \Gamma_{\mathrm{o}}$ that are obtained from the system coefficients A, B, C, D. However, the variation in the system parameters is unknown. Accordingly, the variation in $\Gamma_{\mathrm{i}}, \Gamma_{\mathrm{o}}$ is unknown, and thus the coefficients H_i are unknown. $\mathbf{q}$ is forward shifting operator, which is the discrete form of $\mathbf{p}$. $\mathbf{q}$ is equivalent to the discrete complex frequency variable z when all initial conditions are zero. The forward shifting operator can be directly substituted when multiplied by any discrete time signals, such that $\mathbf{q}^{-i} y_{\mathrm{i}}(k) = y_{\mathrm{i}}(k-i)$.

5.2.1 FIR Model Order Selection

It is evident that increasing the FIR model order allows the ability to capture more system dynamics. Unlike the typical implementation of the FIR models where the input-output of the FIR are the same as the system's input-output, both the input and output of the FIR model are outputs of the underlying system in the proposed approach. That is, the FIR model is used to represent the relationship from an output y_{i} to another output y_{o}. Due to the unknown change in the system parameters A, B, C, D, the relationship between y_{i} and y_{o} is unknown. The relationship from y_{i} to y_{o} might be noncausal. The physical interpretation of this noncausality is that y_{i} might occur before or after y_{o}. If y_{i} occurs after y_{o}, then the input of the used FIR model occurs after the output of the FIR model. Accordingly, the estimation of y_{o} at the current time step k, depends on the future measurements of y_{i}.

Noncausal FIR models consist of two high-order terms, the typical causal order that is denoted by r and the noncausal order that is denoted by d. The casual order r refers to how many previous steps of y_{i} are included in the estimation of y_{o}, while the noncausal order d refers to how many future measurements of y_{i} are included in the estimation of y_{o}. This results in a time-delay in the estimation of y_{o} till the required future measurements of y_{i} are available. Increasing the noncausal FIR order captures more dynamics, however, will result in a higher time-delay in the estimation of y_{o}. Therefore, the orders of the FIR model are selected according to the application such that the FIR captures enough dynamics while the estimation time-delay is negligible.

5.2.2 RLS Identification

An estimate of y_{o} can be obtained from y_{i} using

$$\hat{y}_{\mathrm{o}}(k) \triangleq \sum_{i=-d}^{r} H_i(k) y_{\mathrm{i}}(k-i). \tag{5.13}$$

Define the estimation residual

$$\begin{aligned} e(k|\Theta_{r,d}^{\mathrm{FIR}}(k)) &\triangleq y_{\mathrm{o}}(k) - \hat{y}_{\mathrm{o}}(k), \\ &\triangleq y_{\mathrm{o}}(k) - \sum_{i=-d}^{r} H_i(k) y_{\mathrm{i}}(k-i), \end{aligned} \tag{5.14}$$

where

$$\Theta_{r,d}^{\mathrm{FIR}}(k) \triangleq [H_{-d}(k), \ldots, H_r(k)] \in \mathbb{R}^{[p-m]\times[m(r+d+1)]}.$$

$\Theta_{r,d}^{\mathrm{FIR}}$ is called Markov parameters of the transmissibility operator $\mathscr{T}$.

Note that (5.14) can be interpreted as

$$y_{\mathrm{o}}(k) = \Theta_{r,d}^{\mathrm{FIR}}(k) v(k) + e(k|\Theta_{r,d}^{\mathrm{FIR}}(k)), \tag{5.15}$$

where

$$v(k)[y_{\mathrm{i}}(k+d), \ldots, y_{\mathrm{i}}(k-r)]^{\mathrm{T}} \in \mathbb{R}^{m(r+d+1)\times 1}.$$

Remark. The variation in $\Theta_{r,d}^{\mathrm{FIR}}$ is unknown due to unknown variation in A, B, C, D.

Since the variation in $\Theta_{r,d}^{\mathrm{FIR}}$ is unknown, $\Theta_{r,d}^{\mathrm{FIR}}$ needs to be identified overtime. The following theorem shows how to recursively estimate the transmissibility parameter $\hat{\Theta}_{r,d}^{\mathrm{FIR}}$ in the FIR format. The recursive estimation of $\Theta_{r,d}^{\mathrm{FIR}}$ estimates the evolution in the system parameters between the last and current steps. This is rather than re-identifying $\Theta_{r,d}^{\mathrm{FIR}}$ since the beginning at each time step, which is intense and might not be possible as $k \longrightarrow \infty$.

The following Lemma, which is used in the proof of Theorem 1, is an indirect implementation of the Woodbury matrix identity [103].

Lemma 1. Let $F \in \mathbb{R}^{c\times c}$ be nonsingular and let $G \in \mathbb{R}^{c\times 1}$ and $\ell \in \mathbb{R}$, then

$$\begin{aligned} &(F + \ell G G^{\mathrm{T}})^{-1} = \\ &\quad F^{-1} - F^{-1}\ell G(1 + G^{\mathrm{T}} F^{-1} \ell G)^{-1} G^{\mathrm{T}} F^{-1}, \end{aligned} \tag{5.16}$$

Lemma 1 Proof. Define $L(1+G^{\mathrm{T}}F^{-1}\ell G)$, then multiply

$$\begin{aligned}
&(F+\ell GG^{\mathrm{T}})(F^{-1}-F^{-1}\ell GL^{-1}G^{\mathrm{T}}F^{-1})\\
&\quad=\mathbf{I}+\ell GG^{\mathrm{T}}F^{-1}-\ell GL^{-1}G^{\mathrm{T}}F^{-1}\\
&\qquad-\ell GG^{\mathrm{T}}F^{-1}\ell GL^{-1}G^{\mathrm{T}}F^{-1}\\
&\quad=\mathbf{I}+\ell GG^{\mathrm{T}}F^{-1}\\
&\qquad-\ell G(1+G^{\mathrm{T}}F^{-1}\ell G)L^{-1}G^{\mathrm{T}}F^{-1}\\
&\quad=\mathbf{I}+\ell GG^{\mathrm{T}}F^{-1}-\ell GLL^{-1}G^{\mathrm{T}}F^{-1}\\
&\quad=\mathbf{I}. \qquad \square
\end{aligned}$$

Theorem 1. For the transmissibility operator $\mathscr{T}$ that relates y_{i} to y_{o} in (7.1)-(5.4), an estimation of the transmissibility parameters $\hat{\Theta}^{\mathrm{FIR}}_{r,d}$ can be recursively estimated at time step k from

$$\hat{\Theta}^{\mathrm{FIR}}_{r,d}(k)=\hat{\Theta}^{\mathrm{FIR}}_{r,d}(k-1)+e(k|\hat{\Theta}^{\mathrm{FIR}}_{r,d}(k-1))\kappa^{\mathrm{T}}(k), \tag{5.17}$$

where

$$\begin{aligned}
\kappa(k)&=\lambda(k)\mathbf{V}(k-1)v(k)\left(1+\lambda(k)v^{\mathrm{T}}(k)\mathbf{V}(k-1)v(k)\right)^{-1},\\
\mathbf{V}(k)&=\mathbf{V}(k-1)-\kappa(k)v^{\mathrm{T}}(k)\mathbf{V}(k-1),\\
e(k|\hat{\Theta}^{\mathrm{FIR}}_{r,d}(k-1))&\stackrel{\Delta}{=}y_{\mathrm{o}}(k)-\hat{\Theta}^{\mathrm{FIR}}_{r,d}(k-1)v(k),
\end{aligned}$$

and $\lambda\in(0,1]$ is the forgetting factor.

Theorem 1 Proof. Define the cost function

$$\mathscr{C}(k|\hat{\Theta}^{\mathrm{FIR}}_{r,d})\sum_{j=0}^{k}\lambda(j)||e(j|\hat{\Theta}^{\mathrm{FIR}}_{r,d}(k))||^2. \tag{5.18}$$

Substituting $e(j|\hat{\Theta}^{\text{FIR}}_{r,d})$ from (5.15) yields

$$\begin{aligned}\mathscr{C}(k|\hat{\Theta}^{\text{FIR}}_{r,d}) \sum_{j=0}^{k} \lambda(j) \Big[& y_{\text{o}}(j) y_{\text{o}}^{\text{T}}(j) \\ & - \hat{\Theta}^{\text{FIR}}_{r,d}(k) v(j) y_{\text{o}}^{\text{T}}(j) \\ & - y_{\text{o}}(j) v^{\text{T}}(j) (\hat{\Theta}^{\text{FIR}}_{r,d}(k))^{\text{T}} \\ & + \hat{\Theta}^{\text{FIR}}_{r,d}(k) v(j) v^{\text{T}}(j) (\hat{\Theta}^{\text{FIR}}_{r,d}(k))^{\text{T}} \Big].\end{aligned} \tag{5.19}$$

Next, taking the derivative of (5.19) with respect to $\hat{\Theta}^{\text{FIR}}_{r,d}$ and setting the obtained expression to zero yields,

$$-\sum_{j=0}^{k} \lambda(j) \left[v(j) y_{\text{o}}^{\text{T}}(j) - v(j) v^{\text{T}}(j) (\hat{\Theta}^{\text{FIR}}_{r,d}(k))^{\text{T}} \right] = 0. \tag{5.20}$$

Solving (5.20) for $\hat{\Theta}^{\text{FIR}}_{r,d}(k)$ yields

$$\hat{\Theta}^{\text{FIR}}_{r,d}(k) = (\Phi^{-1}(k) \Psi(k))^{\text{T}}, \tag{5.21}$$

where $\Phi(k)$ is the weighted sample covariance matrix for $y_{\text{i}}(k)$, and $\Psi(k)$ is the equivalent estimate for the cross-covariance between y_{i} and y_{o}, that is, $\Phi(k)$ and $\Psi(k)$ are given by

$$\begin{aligned}\Phi(k) &= \sum_{j=0}^{k} \lambda(j) v(j) v^{\text{T}}(j) \in \mathbb{R}^{[m(r+d+1)] \times [m(r+d+1)]}, \\ \Psi(k) &= \sum_{j=0}^{k} \lambda(j) v(j) y_{\text{o}}^{\text{T}}(j) \in \mathbb{R}^{[m(r+d+1)] \times [p-m]}.\end{aligned}$$

Estimating the transmissibility parameters at time k from (5.21) might seem possible, however, computing (5.21) at each time step is intense and might not be possible as $k \longrightarrow \infty$. Therefore, we consider determining the transition from $\hat{\Theta}^{\text{FIR}}_{r,d}(k-1)$ to $\hat{\Theta}^{\text{FIR}}_{r,d}(k)$. Define

$$\hat{\Theta}^{\text{FIR}}_{r,d}(k) = \hat{\Theta}^{\text{FIR}}_{r,d}(k-1) + \Delta \hat{\Theta}^{\text{FIR}}_{r,d}(k-1), \tag{5.22}$$

where $\Delta\hat{\Theta}^{\text{FIR}}_{r,d}(k-1)$ is the evolution in the transmissibility parameters from time step $k-1$ to k. Reformulating $\Phi(k)$ in terms of $\Phi(k-1)$ yields

$$\begin{aligned}\Phi(k) &= \sum_{j=0}^{k-1} \lambda(j)v(j)v^{\mathrm{T}}(j) + \lambda(k)v(k)v^{\mathrm{T}}(k) \\ &= \Phi(k-1) + \lambda(k)v(k)v^{\mathrm{T}}(k),\end{aligned} \tag{5.23}$$

and similarly

$$\Psi(k) = \Psi(k-1) + \lambda(k)v(k)y_{\mathrm{o}}^{\mathrm{T}}(k). \tag{5.24}$$

Using **Lemma 1**, $\Phi^{-1}(k)$ can be written as

$$\begin{aligned}&\Phi^{-1}(k) = \Phi^{-1}(k-1) - \Phi^{-1}(k-1)\lambda(k)v(k) \\ &(1 + v^{\mathrm{T}}(k)\Phi^{-1}(k-1)\lambda(k)v(k))^{-1}v^{\mathrm{T}}(k)\Phi^{-1}(k-1).\end{aligned} \tag{5.25}$$

For convenience, let $\mathbf{V}(k) = \Phi^{-1}(k)$ and recall the definition of $\kappa(k)$ defined in the Theorem, then (5.25) becomes

$$\mathbf{V}(k) = \mathbf{V}(k-1) - \kappa(k)v^{\mathrm{T}}(k)\mathbf{V}(k-1), \tag{5.26}$$

which is the definition of $\mathbf{V}(k)$ in the Theorem. From the definition of κ in the theorem we can write

$$\kappa(k)[1 + \lambda(k)v^{\mathrm{T}}(k)\mathbf{V}(k-1)v(k)] = \lambda(k)\mathbf{V}(k-1)v(k),$$

which can be interpreted as

$$\kappa(k) = \lambda(k)[\mathbf{V}(k-1) - \kappa(k)v^{\mathrm{T}}(k)\mathbf{V}(k-1)]v(k),$$

moreover, substitute (5.26) yields

$$\kappa(k) = \lambda(k)\mathbf{V}(k)v(k). \tag{5.27}$$

Substitute (5.24) in (5.21) yields

$$\hat{\Theta}^{\text{FIR}}_{r,d}(k) = [\mathbf{V}(k)\Psi(k-1) + \lambda(k)\mathbf{V}(k)v(k)y_{\mathrm{o}}^{\mathrm{T}}(k)]^{\mathrm{T}}. \tag{5.28}$$

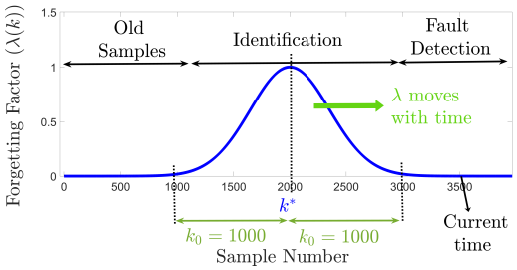

Fig. 5.1 An example on constructing the forgetting factor λ with $k^* = 2000$ samples, $k_0 = 1000$ samples, and the current time step is 3500. The defined forgetting factor gives enough time to detect faults first, then activate the identification algorithm in case no faults are detected.

Next, substitute (5.26) and (5.27) in (5.28)

$$\hat{\Theta}_{r,d}^{\mathrm{FIR}}(k) = \Big[\mathbf{V}(k-1)\Psi(k-1) + \boldsymbol{\kappa}(k)y_{\mathrm{o}}^{\mathrm{T}}(k) - \boldsymbol{\kappa}(k)v^{\mathrm{T}}(k)\mathbf{V}(k-1)\Psi(k-1)\Big]^{\mathrm{T}},$$

note that $\hat{\Theta}_{r,d}^{\mathrm{FIR}}(k-1) = (\mathbf{V}(\mathbf{k-1})\Psi(k-1))^{\mathrm{T}}$, then

$$\hat{\Theta}_{r,d}^{\mathrm{FIR}}(k) = \hat{\Theta}_{r,d}^{\mathrm{FIR}}(k-1) + e(k|\hat{\Theta}_{r,d}^{\mathrm{FIR}}(k-1))\boldsymbol{\kappa}^{\mathrm{T}}(k). \quad \square$$

5.3 Application on Fault Detection

The main challenge in using the residual computed in (5.14) for the purpose of fault detection is to distinguish if the changes in e are due to parameter change or system faults. The recursive identification in (5.17) is not urgent at each time step. Then we consider detecting the faults first, then updating the transmissibility parameters if no faults are detected. For this purpose, we define the forgetting factor λ around a time step k^* to be $\lambda(k^*) \approx 1$ where the system is known to be healthy for k_0 steps and the variant parameters reached the upper and lower bounds, such as

$$\lambda(k) = \exp\left(\frac{-(k-k^*)^2}{(0.5k_0)^2}\right). \tag{5.29}$$

Note that k_0 is picked to guarantee that (5.17) has enough time to optimize $\hat{\Theta}_{r,d}^{\mathrm{FIR}}$.

Remark 2. The forgetting factor λ is designed to detect faults first, and then update the estimated transmissibility parameters $\hat{\Theta}_{r,d}^{\mathrm{FIR}}$ if no faults are detected.

The system is considered to start operating in a healthy manner, and the variant system parameters oscillate between the upper and lower bounds for k_0 steps. The initial value for k^* is set to $k^* = 0$. As explained in the last paragraph of Section 5.2, the parameters $\hat{\Theta}^{\text{FIR}}_{r,d}(k_0)$ need to be updated overtime. However, after a period of time the forgetting factor $\lambda \approx 0$. The update is here done by updating the constant k^* overtime. Let $\bar{k}^*$ be a time step after k^*, assume that no faults are detected between k^* and $\bar{k}^*$, and the variant system parameters are known to reach the upper and lower bounds within this time interval. Then k^* can be updated to $\bar{k}^*$, which will set the forgetting value to $\lambda(\bar{k}^*) \approx 1$, and thus activating the RLS algorithm around the time step $\bar{k}^*$.

It is worth mentioning here that if the fault happens before the time step k_0 while k^* is still $k^* = 0$, the fault might be detected. This is because of the exponential formula of the forgetting factor λ. When $k = k^* = 0, \lambda(k) = 1$, the RLS will force the transmissibility parameters to adapt to the dynamics change whether it's due to parameters change or system fault and the fault will not be detected. However, as $k \longrightarrow k_0, \lambda(k) \longrightarrow 0$, the RLS algorithm becomes less sensitive to the parameter change, and the likelihood to detect faults increases. In the next two sections, we present two different experiments, one with faults that occur after k_0, and one with the fault that occurs before k_0. Figure 5.1 shows an example on constructing the forgetting factor λ with $k^* = 2000$ samples, $k_0 = 1000$ samples, and the current time step is 3500. The defined forgetting factor gives enough time to detect faults first, then activate the identification algorithm in case no faults are detected.

The faults are assumed to be within different parameters than the variant parameters in the system. For the level of the residual e to be more obvious and readable, we define for all $k \geq 0$

$$E(k|\hat{\Theta}^{\text{FIR}}_{r,d}, w) \triangleq \sqrt{\sum_{i=k}^{w+k} \|e(i|\hat{\Theta}^{\text{FIR}}_{r,d}(i))\|}, \tag{5.30}$$

which represents the norm of residual over a sliding window with width w steps. Let η be the signal-to-noise ratio, then define the threshold [135]

$$\mu(\hat{\Theta}^{\text{FIR}}_{r,d,\ell}, w, k^*) \frac{\eta}{k_0 + 1} \sum_{i=(k^*-k_0)}^{(k^*)} E(i|\hat{\Theta}^{\text{FIR}}_{r,d,\ell}, w), \tag{5.31}$$

where for $k < 0$ (before running the system), $E(k|\hat{\Theta}^{\text{FIR}}_{r,d,\ell}, w) = 0$.

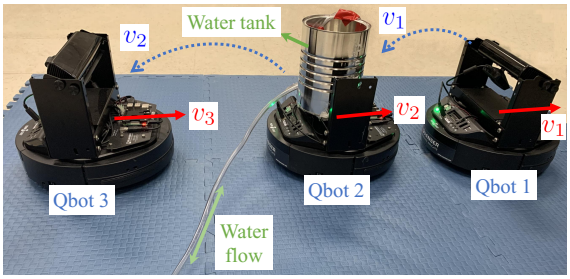

Fig. 5.2 Experiment 1 setup: Three connected autonomous robots in a longitudinal platoon formulation. Two varying parameters in the system, which are the mass of Qbot2 due to the water flow, and the friction coefficient which depends on where the robot is moving (i.e. on the blue mats or the floor).

5.4 Experiment 1: Connected Autonomous Robots

This experiment considers a connected autonomous robotic system with two variable parameters in the state matrix A. The faults are emulated after the time step k_0. Three different common faults are considered in this experiment.

5.4.1 Experimental Setup

The experimental setup shown in Figure 5.2 consists of three Quanser autonomous differential robots called Qbots 2e. Each Qbot consists of two coaxial wheels, where each wheel is driven by a DC motor that is controlled using a closed-loop inverse kinematic controller. The robots are connected with V2V communication links to emulate Connected Autonomous Vehicle (CAV) platoons. The velocity of both wheels in each robot is set to be equal to have longitudinal motion only. Qbot1 receives the excitation signal from a computer through wireless communication, and Qbot2 velocity tracks Qbot1 velocity v_1. Similarly, Qbot3 is connected with Qbot2 via a V2V communication channel, and Qbot3 velocity v_3 tracks Qbot2 velocity v_2. Two parameters are considered to vary over time within the setup. The first parameter is the second robot's mass, where a water tank is attached to the robot body and the water flows randomly in and out the tank during the entire experiment. That is, the variation in the water level of the tank is unknown. The second variant parameter is the ground friction, where all robots move randomly on the soft blue mats shown in Figure 5.2 and the ground during the entire experiment.

5.4.2 RLS Transmissibility Identification

We start the setup by sending band-limited white noise with zero mean and unit variance to the first robot as the desired velocity of the platoon. The transmissibility inputs are defined as $y_{\mathrm{i}}(k) = [v_1(k)\ v_2(k)]^{\mathrm{T}}$, and the transmissibility output is defined as $y_{\mathrm{o}}(k) = v_3(k)$. We set

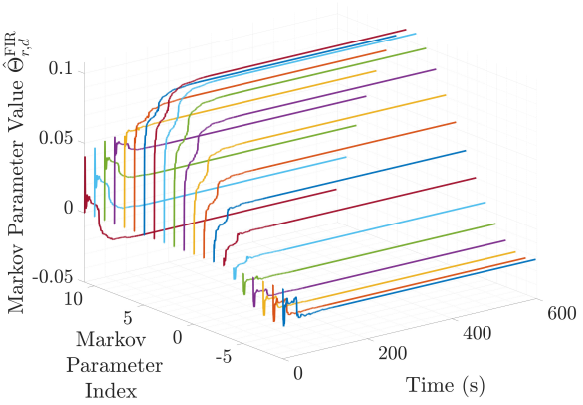

Fig. 5.3 First experiment results: The identified Markov parameters $\hat{\Theta}^{\text{FIR}}_{r,d}$ and their variance over time. The identified parameters are optimized approximately at time $t = 60$ seconds. The z-axis is the Figure's legend where the ith Markov parameter is H_i.

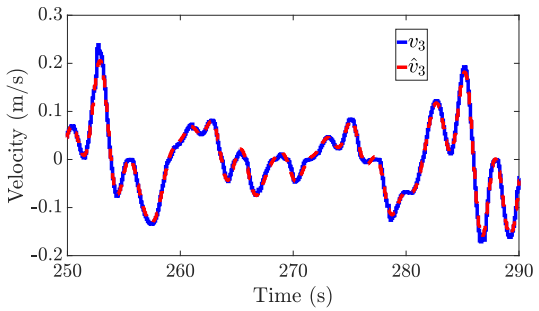

Fig. 5.4 First experiment results: Comparison between the measured and estimated velocities of Qbot3 using the Markov parameters in Figure 5.3. Note that measured and estimated are close to each other after the Markov parameters are optimized at time $t = 60$ seconds.

$k^* = 0$ for the entire experiment, and k_0 is set to be $k_0 = 1000$ steps where the sampling time is 0.1 second. The RLS algorithm in (5.17) starts at $k = 0$ with the FIR orders $r = d = 10$. Figure 5.3 shows the identified Markov parameters $\hat{\Theta}^{\text{FIR}}_{r,d}$ and its variation with time. The z-axis (Markov Parameter Index) is the legend of this Figure. Such that, the ith Markov parameter is the parameter H_i defined in Equation (5.12). From Figure 5.3 we can see that all the transmissibility parameters started settling on specific values at approximately $k = 600$ steps (at time $t = 60$ seconds). Figure 5.4 shows the measured and estimated velocities of the third robot between time steps $k = 2500$ and $k = 2900$ (i.e from $t = 250$ to $t = 290$ seconds), which is a time interval after the RLS has optimized the transmissibility parameters and before emulating the faults. We can see from Figure 5.4 that while the system parameters varies randomly and the system is under random excitation u, the measured and estimated signals of the third robot are close to each other.

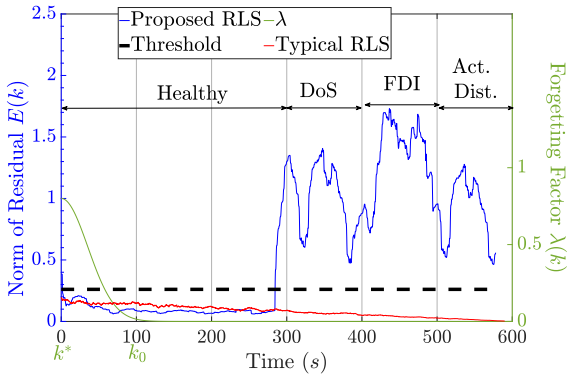

Fig. 5.5 First experiment results: Norm of residual over a sliding window with width $w = 100$ steps, where this experiment considers faults after the time step k_0. Three different faults occurred individually, which resulted in increasing the norm of residual over the threshold limit, and the faults are then detected.

5.4.3 Faults Emulation and Fault Detection

Next, at time step $k = 3000$ ($t = 300$ seconds) the first fault was emulated. The first fault is represented in 1 second communication time delay between the second and third robots. At time step $k = 4000$ ($t = 400$ seconds) the delay fault was removed, and the second fault was emulated. The second fault is False Data Injection (FDI), which is represented as injecting bounded noise to the velocity signal v_2 that is transmitted through the wireless communication channel. At time step $k = 5000$ ($t = 500$ seconds) the FDI fault was removed, and the third fault was emulated. The third fault is actuator disturbances, which is represented in injecting bounded noise to the left wheel control signal of Qbot2 to result in 2D motion. The norm of residual defined in (5.30) is then computed for all $0 \leq k \leq 6000$ with width $w = 100$ steps as shown in Figure 5.5. We can see from Figure 5.5 that between $k = 1000$ and $k = 3000$ ($t = 100$ - $t = 300$ seconds) even while the system parameters are varying, the residual e was minimized. At time step $k = 3000$ ($t = 300$), the level of the norm of residual increased with emulating the first fault. The level of the norm of residual stayed high for the second and third faults as well. Note that in Figure 5.5 the level increase started at time step $k = 2900$ ($t = 290$ seconds) as computing the norm of residual in (5.30) uses the front $w = 100$ steps to compute E at step $k = 2900$. Figure (5.30) compares the proposed technique with the typical RLS identification. Notice that in the typical RLS as $k \longrightarrow \infty$, the identification becomes more aggressive and forces the residual always to converge to zero regardless if its a fault or parameter variance. Therefore, the faults were not detected using the typical RLS.

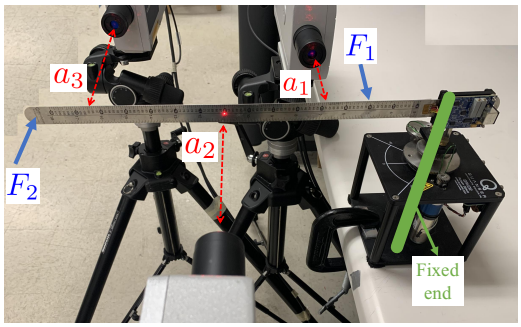

Fig. 5.6 Experiment 2 setup: Quanser's flexible link structured as a cantilever flexible beam under random excitation with variant location. The excitation location changes randomly between F_1 and F_2. Three laser vibrometers are mounted to measure the acceleration at $a_1, \ldots, a_3$.

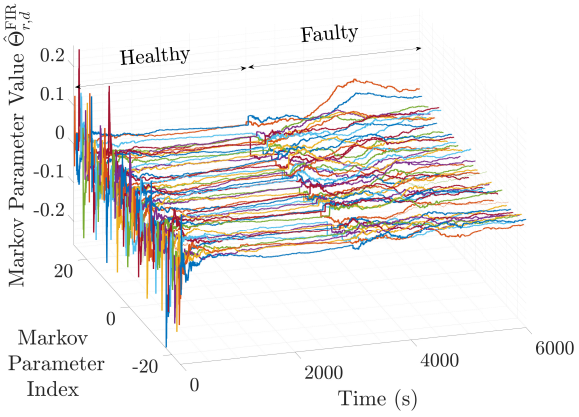

Fig. 5.7 Second experiment results: the identified Markov parameters $\hat{\Theta}^{\text{FIR}}_{r,d}$ and their variance over time. The identified parameters are optimized approximately at time $t = 1100$ seconds, however, the fault occured before k_0 at time $t = 3000$ seconds where the RLS identification is still active.The z-axis is the Figure's legend where the ith Markov parameter is H_i.

5.5 Experiment 2: Flexible Beams

This experiment considers random excitations on a class of flexible structures with the variable parameter being the excitation location in the input matrix B. The fault is emulated in this experiment before the time step k_0. Transmissibility-based fault detection in time-invariant flexible beams was tested successfully in [65, 67].

5.5.1 Experimental Setup

This experiment uses Quanser's flexible link setup shown in Figure 5.6, which consists of a flexible beam with one end fixed and the rest of the beam is free to oscillate (cantilever beam).

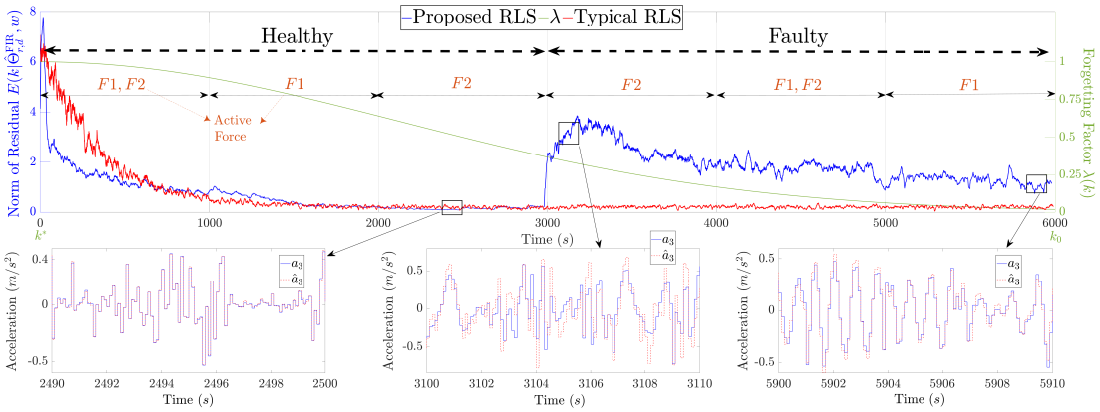

Fig. 5.8 Second experiment results: Norm of residual over a sliding window with width $w = 100$ steps, where this experiment considers a fault before the time step k_0. The forgetting factor λ is plotted to show how active the identification is. Three comparisons between the measured and estimated accelerations are plotted at three different time intervals.

Three Polytech IVS-500 laser vibrometers are mounted and adjusted perpendicularly to the beam at stationary. The laser vibrometers measure the acceleration in the laser direction at three different locations $a_1(k), \ldots, a_3(k)$. Two random forces generated by hand are acting on the beam, F_1 at approximately $8cm$ from the fixed end, and F_2 at the free end. The beam bending angle was $< 5^o$ for the entire experiment to avoid any nonlinearities due to the beam deflection, and be able to observe the parameters change. The variant parameters in this experiment are related to the input matrix B by changing the input location, such that changing the excitations from F_1 to F_2 will change the states that the excitation is injected to.

5.5.2 RLS Transmissibility Identification

The transmissibility inputs are defined as $y_i(k) = \begin{bmatrix} a_1(k) & a_2(k) \end{bmatrix}^T$, and the transmissibility output is defined as $y_o(k) = a_3(k)$. k^* is set to $k^* = 0$ for the entire experiment, and k_0 is pushed too high $k_0 = 60000$ steps where the sampling time is 0.1 second, to investigate faults before k_0 while $k^* = 0$. We start the setup by setting both F_1 and F_2 to random forces by hand within the range of the maximum forces we wish to apply (bounded noise). The RLS algorithm in (5.17) starts at $k = 0$ with the FIR orders $r = d = 25$. The active forces switch randomly every 1000 seconds between F_1, F_2, or both F_1, F_2 are active at the same time. Figure 5.7 shows the identified Markov parameters $\hat{\Theta}^{\text{FIR}}_{r,d}$ and its variation with time. The z-axis (Markov Parameter Index) is the legend of this Figure. Such that, the ith Markov parameter is the parameter H_i defined in Equation (5.12). From Figure 5.3 we can see that all the transmissibility parameters started settling at approximately $k = 11000$ steps (at time $t = 1100$ seconds). Note that the variation in $\hat{\Theta}^{\text{FIR}}_{r,d}$ after time $t = 3000$ seconds is due to the

system fault while the identification is still active, as will be explained further in the next subsection.

5.5.3 Faults Emulation and Fault Detection

The fault was emulated by attaching a rigid body between a_2 and a_3. This fault is related to a change in the mass and stiffness of the beam portion that the rigid body was attached to. The rigid body was attached at time step $k = 30000$ ($t = 3000$) seconds, while the setup is still running to avoid any initial conditions effect. The norm of residual defined in (5.30) is then computed for all $0 \leq k \leq 60000$ with width $w = 200$ steps as shown in Figure 5.8.

The norm of residual starts high at $k = 0$ and drops gradually with time. For the first 1000 seconds both forces are active to satisfy the assumption of reaching both upper and lower bounds in B around $k^* = 0$. We can see from Figure 5.8 that at time $t = 1000$ and $t = 2000$ seconds switching the forces didn't result in increasing the level of residual. This is because the transmissibility parameters were already adapted with both forces during the first 1000 seconds of the experiment. The bottom-left plot of Figure 5.8 shows a comparison between the measured and estimated acceleration at the third location a_3, which are very close to each other. After applying the fault at time $t = 3000$ seconds, the change in the system dynamics led to increasing the level of the norm of residual. Since the transmissibility parameters are known to adapt with all possible variant parameters before approximately $t = 1500$ seconds, the increase in the level of residual at time $t = 3000$ can be regarded as a system fault. Note that switching the active forces after $t = 3000$ doesn't result in increasing E. This is because the change in parameters (switching the forces) is still within the boundaries that the transmissibility adapted with during the first 1000 seconds. Figure (5.8) compares the proposed technique with the typical RLS identification. Notice that in the typical RLS as $k \longrightarrow \infty$, the identification becomes more aggressive and forces the residual always to converge to zero regardless if its a fault or parameter variance. Therefore, the faults were not detected using the typical RLS.

Another important observation from Figure 5.8 is the relation between the norm of residual E and the forgetting factor λ. At the time $t = 0$, the forgetting factor was at maximum $\lambda = 1$, which means the RLS works completely to identify the transmissibilities and drop down the high level of E. Since λ decreases exponentially, it becomes more difficult to adapt with the dynamics change as $t \longrightarrow 6000$. The bottom-middle and bottom-right plots of Figure 5.8 show comparisons between the measured and estimated accelerations after the fault happened and around $\lambda \approx 0$, respectively. This explains why it was difficult for the RLS to adapt to the system fault at $t = 3000$. Note that if the fault happened in the first 500

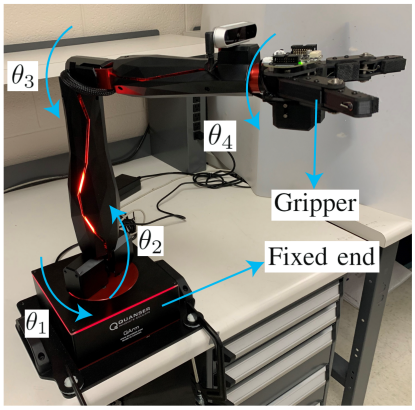

Fig. 5.9 Experiment 3 setup: Quanser's Robotic arm (QArm) with four joints and a gripper. Four DC motors control the four joints. The arm is considered to move randomly and pick random masses.

seconds, it will be difficult to detect it and the fault effect will disappear quickly. However, the closer the fault occurs to k_0, the higher likelihood to detect it.

5.6 Experiment 3: Robotic Manipulators

5.6.1 Experimental Setup

For this experiment, we consider Quanser's robotic arm (QArm) shown in Figure 7.7 consists of a robotic arm with fixed base and four joints. The rotation range of the first and fourth joints is 360 degrees, and the second and third joints are 180 degrees. Four DC motors control the four joints. A gripper with five contact points is attached to the free end of the arm. The gripper is controlled through the computer's keyboard to two positions, hold or release. Six different objects are picked separately, one at a time, with maximum mass of $500g$. A random operation of the arm is considered to emulate the unknown input on the system. The desired angular velocity of the first joint θ_1^* is set to white Gaussian noise with zero mean and unit variance. The second joint's desired angular velocity is set to track the velocity of the first joint $\theta_2^* = \theta_1$, and similarly, the third to track the second $\theta_3^* = \theta_2$, and the fourth to track the third $\theta_4^* = \theta_3$. Notice that this technique is applicable regardless of what Euler-Lagrange dynamical structure the manipulator is following due to the robustness against unknown nonlinearities. Throughout the operation, the picked mass was changed manually while the arm is moving every approximately 40 seconds.

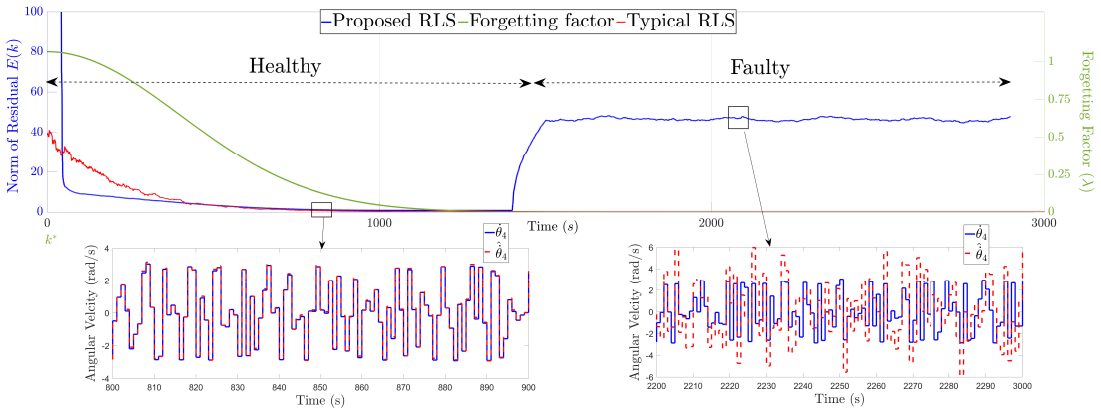

Fig. 5.10 Third experiment results: Norm of residual over a sliding window with width $w = 100$ steps. The forgetting factor λ is plotted to show how active the identification is. Two comparisons between the measured and estimated angular velocities are plotted at two different time intervals before and after the fault.

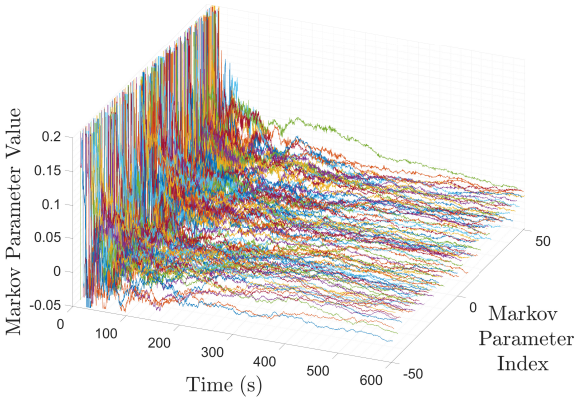

Fig. 5.11 Third experiment results: the identified Markov parameters $\hat{\Theta}^{\text{FIR}}_{r,d}$ and their variance over time. The identified parameters are optimized approximately at time $t = 300$ seconds. The z-axis is the Figure's legend where the ith Markov parameter is H_i.

5.6.2 RLS Transmissibility Identification

The transmissibility inputs are defined as $y_{\text{i}}(k) = \begin{bmatrix} \dot{\theta}_1(k) & \dot{\theta}_2(k) & \dot{\theta}_3(k) \end{bmatrix}^{\text{T}}$, and the transmissibility output is defined as $y_{\text{o}}(k) = \dot{\theta}_4(k)$. k^* is set to $k^* = 0$ for the entire experiment, and k_0 is pushed too high $k_0 = 1000$ steps where the sampling time is 1 second. The RLS algorithm in (5.17) starts at $k = 0$ with the FIR orders $r = d = 50$. We manually switch the picked mass every 40 seconds to another one of the six masses. The six masses are $180g, 260g, 290g, 380g, 430g$, and $500g$. Figure 5.11 shows the identified Markov parameters $\hat{\Theta}^{\text{FIR}}_{r,d}$ and its variation with time. The z-axis (Markov Parameter Index) is the legend of this Figure. Such that, the ith Markov parameter is the parameter H_i defined in Equation

(5.12). From Figure 5.11 we can see that all the transmissibility parameters started settling at approximately $t = 300$ seconds.

5.6.3 Faults Emulation and Fault Detection

The fault was emulated by attaching rubber bands on the third joint. This fault is related to change in the stiffness of the third joint. The fault was emulated at time $t = 1500$ ($t = 1500$) seconds, while the setup is still running to avoid any initial conditions effect. The norm of residual defined in (5.30) is then computed for all $0 \leq k \leq 3000$ with width $w = 100$ steps as shown in Figure 5.10.

The norm of residual starts high at $k = 0$ and drops gradually with time. For the first 300 seconds all masses were picked to satisfy the assumption of reaching both upper and lower bounds. We can see from Figure 5.10 that switching the picked mass didn't result in increasing the level of residual. This is because the transmissibility parameters were already adapted with all masses during the first 300 seconds of the experiment. The bottom-left plot of Figure 5.10 shows a comparison between the measured and estimated angular velocities of the fourth joint $\dot{\theta}_4$, which are very close to each other. After applying the fault at time $t = 1500$ seconds, the change in the system dynamics led to increasing the level of the norm of residual. Since the transmissibility parameters are known to adapt with all possible variant parameters before approximately $t = 300$ seconds, the increase in the level of residual at time $t = 1500$ can be regarded as a system fault. Note that switching the picked mass after $t = 1500$ doesn't result in increasing E. This is because the change in parameters (switching masses) is still within the boundaries that the transmissibility adapted with during the first 300 seconds. Figure (5.10) compares the proposed technique with the typical RLS identification. Notice that in the typical RLS as $k \longrightarrow \infty$, the identification becomes more aggressive and forces the residual always to converge to zero regardless if its a fault or parameter variance. Therefore, the faults were not detected using the typical RLS.

Another important observation from Figure 5.10 is the relation between the norm of residual E and the forgetting factor λ. At the time $t = 0$, the forgetting factor was at maximum $\lambda = 1$, which means the RLS works completely to identify the transmissibilities and drop the high level of E. Since λ decreases exponentially, it becomes more difficult to adapt with the dynamics change as $t \longrightarrow 1000$. The identification after time $t = 1000$ seconds is inactive, and k^* wasn't updated since a fault was detected. The bottom-right plot of Figure 5.10 shows a comparison between the measured and estimated angular velocities of the fourth joint after the fault happened $\lambda \approx 0$, respectively. This explains why the RLS didn't adapt to the system fault at $t = 1500$. Note that if the fault happened in the first 800 seconds, it will be difficult

to detect it and the fault effect will disappear quickly. However, the closer the fault occurs to k_0, the higher likelihood to detect it.

5.7 Discussion of the Superiority of the Claimed Contributions

The first contribution is related to count for unknown nonlinearities while the system parameters are varying. In the first experiment, the system was mostly linear with some nonlinearities due to the robots' communications, while the second robot's mass and the ground friction vary. Similarly, the flexible beam in the second experiment was mostly linear with some nonlinearities due to the deflection. In both experiments, setting the transmissibility input y_{i} to two sensor measurements gave enough robustness against the unmodeled nonlinearities while the systems are healthy since the systems are mostly linear. This can be seen from Figures 5.4 and the bottom left plot of Figure 5.8. However, in the third experiment the level of nonlinearities was higher than in the first two experiments due to the 3D motion and many degrees of freedom of the system. Therefore, y_{i} was set to three sensor measurements to give robustness against the system nonlinearities.

Regarding the second contribution, the transmissibility parameters are updated recursively overtime in the three experiments as shown in Figures 5.3, 5.7, and 5.11. Accordingly, the norm of residual at the beginning of the experiments in Figures 5.5, 5.8, and 5.10 converges to zero under healthy conditions over time regardless of the parameter variations. The third contribution can also be claimed in the three experiments. Different cyber and physical faults were emulated in the three experiments while the system parameters vary. All faults were detected as can be seen in Figures 5.5, 5.8, and 5.10.

Chapter 6

High-gain Transmissibility (HGT)

6.1 Problem Formulation

Consider the following nonlinear state space model

$$\dot{x}(t) = Ax(t) + Bf(t,x,u), \tag{6.1}$$

$$y(t) = Cx(t), \tag{6.2}$$

where $A \in \mathbb{R}^{n\times n}$ is Hurwitz, $B \in \mathbb{R}^{n\times m}$, $C \in \mathbb{R}^{p\times n}$, n is the system order, m is the number inputs, $p \geq m$ is the number of measured outputs, and $f : \mathbb{R}^n \to \mathbb{R}^m$ is a bounded nonlinear function.

We consider the following assumptions:
Assumption A1) All zeros of (A.10), (A.11) are minimum phase.
Assumption A2) All uncertainties in (A.10) are included in the nonlinear function f.
Assumption A3) C is known and the pair (A,C) is observable.

Considering Assumptions A1)–A3), the objective of this work is to asymptotically estimate the state x of the system (A.10), (A.11) only using measurements of y.

Notice that a high-gain observer cannot be directly applied to the realization (A.10), (A.11) since the it is not in a canonical form, and cannot be transformed to a canonical form since f is unknown [69]. In addition, it is challenging for high-gain observers to use noisy output measurements for state estimation as high-gain observers are sensitive to measurement noise.

The technique proposed in this work assumes a virtual set of signals to establish a set of pseudo states, in which the system states x are computed from after. The virtual set of signals will take the shape of a set of outputs. The mathematical relationship between the

virtual set of signals and y is called transmissibility. The measurements of y are fed into the transmissibility in a high-gain form to robustly estimate the pseudo states, then the system states x are computed from the pseudo states. Further developments of this direction this carry out similar effects as high-gain observers such as peaking phenomenon.

For clarification, the following motivating example demonstrates the proposed methodology for the case of $m = 1$, that is, the nonlinear function f is a scalar. Section 6.4 generalizes the proposed approach to the case of $m > 1$.

6.2 Motivating Example

Define the following virtual design signal to be any function of the system states x and the nonlinear dynamics f

$$v(t) = C_{\mathrm{v}} x(t) + D_{\mathrm{v}} f(t,x,u) \in \mathbb{R}, \tag{6.3}$$

where $C_{\mathrm{v}}, D_{\mathrm{v}}$ are unknown matrices with appropriate dimensions. This signal will only be used to mathematically design our estimator, but will not appear at the final estimator equations.

6.2.1 Time-domain Transmissibility

Consider the model (A.10), (A.11) with $m = 1$. The transmissibility operator from v to y is given by [4]

$$y(t) = \mathscr{T}(\mathbf{p}) v(t), \tag{6.4}$$

where $\mathbf{p} = \frac{\mathbf{d}}{\mathbf{d}t}$ is the differentiation operator,

$$\mathscr{T}(\mathbf{p}) \triangleq \Gamma_{\mathrm{y}}(\mathbf{p}) \Gamma_{\mathrm{v}}^{-1}(\mathbf{p}), \tag{6.5}$$

$$\Gamma_{\mathrm{v}}(\mathbf{p}) \triangleq C_{\mathrm{v}} \mathrm{adj}(\mathbf{p}I - A) B + D_{\mathrm{v}} \delta(\mathbf{p}), \tag{6.6}$$

$$\Gamma_{\mathrm{y}}(\mathbf{p}) \triangleq C \mathrm{adj}(\mathbf{p}I - A) B, \tag{6.7}$$

$$\delta(\mathbf{p}) \triangleq \det(\mathbf{p}I - A). \tag{6.8}$$

The use of the differentiation operator in [4] came to count for non-zero initial conditions. Since v is designed with the feed-forward term $D_{\mathrm{v}} f(t,x,u)$, the order of Γ_{v} equals to the system order n. On the other hand, the order of Γ_{y} is always less than n. This ensures the

operator $\mathscr{T}$ to always be causal. Notice that since $m = 1$, Γ_{v} and Γ_{y} are two polynomials of $\mathbf{p}$. The transmissibility operator $\mathscr{T}$ here is independent on the nonlinear function f in (A.10)-(A.11).

High-gain observers showed great robustness against uncertain dynamics as shown in [69]. Thus, we extend the transmissibility operator from the form in (6.4) to the form of high-gain transmissibility. To align with the high-gain observers literature, this section formulates the transmissibility operator $\mathscr{T}$ in the state-space format, and then relates y to the system states x.

State Space Representation of Transmissibilities

By substituting (6.5) in (6.4), the operator $\mathscr{T}$ can be interpreted as

$$\frac{1}{\Gamma_{\mathrm{y}}}(\mathbf{p})y(t) = \frac{1}{\Gamma_{\mathrm{v}}}(\mathbf{p})v(t). \tag{6.9}$$

Note that Γ_{v} and Γ_{y} are polynomials of $\mathbf{p}$, thus (6.9) can be written as

$$\frac{1}{b_{n-1}\mathbf{p}^{n-1} + \cdots + b_0}y(t) = \frac{1}{a_n\mathbf{p}^n + \cdots + a_1\mathbf{p} + a_0}v(t), \tag{6.10}$$

where $a_0, \ldots, a_n$ and $b_0, \ldots, b_n$ are the parameters of Γ_{v} and Γ_{y}, respectively. Note that the left hand side of (6.10) is certain by the definition of y in (A.11). The right hand side of (6.10) represents unknown virtual dynamics (uncertain). This motivates splitting the certain dynamics of $\mathscr{T}$ from the uncertain dynamics. To this end, define

$$\bar{y}(t) = \frac{1}{b_n\mathbf{p}^n + \cdots + b_0}y(t). \tag{6.11}$$

Assumption 1 guarantees that the relation from y to $\bar{y}$ is always stable. Substituting (6.11) in (6.10) yields

$$\bar{y}(t) = \frac{1}{a_n\mathbf{p}^n + \cdots + a_1\mathbf{p} + a_0}v(t), \tag{6.12}$$

which represents the uncertain dynamics. The polynomial $a_n\mathbf{p}^n + \cdots + a_0$ plays a crucial role here as it represents the characteristics equation of $\mathscr{T}$ and must be robustly obtained. Inspired by the high-gain observer theory, we represent (6.12) as a chain of integrators. This allows for the use of high gain in a way that makes the transmissibility operator a differentiator [69].

Towards this goal, reformulate equation (6.12) as

$$\mathbf{p}^n \bar{y}(t) = \frac{-1}{a_n} \sum_{j=0}^{n-1} a_j \mathbf{p}^j \bar{y}(t) + \frac{1}{a_n} v(t). \tag{6.13}$$

Note that v is not available. For all $i \in \{1,\dots,n\}$, let $z_i = \mathbf{p}^{i-1}\bar{y}$ and substitute the differentiation operator $\mathbf{p}$ as the first derivative yields the chain of integrators

$$\dot{z}_i(t) = z_{i+1}(t), \;\; i \in \{1,\dots,n-1\}, \tag{6.14}$$

$$\dot{z}_n(t) = \Phi(t,z,v), \tag{6.15}$$

$$\bar{y}(t) = z_1(t). \tag{6.16}$$

where

$$\Phi(t,z,v) = \frac{-1}{a_n} \sum_{j=1}^{n} a_{j-1} z_j(t) + \frac{1}{a_n} v(t),$$

which collects the uncertain dynamics in (6.12). Note that Φ is linear, and therefore can be considered to be always continuous. Note that the output $\bar{y}$ in (6.16) comes from (6.11) that is directly measured. The transmissibility states z are called *pseudo states*. The chain of integrators in (6.14)-(6.16) follows the common canonical form in the literature of high-gain observers, such that all uncertain dynamics are collected in the last state z_n and the measured certain output is the first state z_1. The following section estimates the pseudo states z while Φ is uncertain.

Output-State Relationships

Let, for all $j \in \{1,\dots,n\}$, x_j denote the jth state of the system in (A.10), then define x_j as an independent output of the system

$$x_j(t) = \underbrace{\begin{bmatrix} 0 & \dots & 1 & \dots & 0 \end{bmatrix}}_{C_{x_j}} x(t), \tag{6.17}$$

where the cell with number 1 is the jth index. Following the transmissibility definition in [4] and similar to (6.4), the relationship from the output v to the output x_j can be given as

$$x_j(t) = \mathscr{T}_{x_j}(\mathbf{p}) v(t), \tag{6.18}$$

where

$$\mathscr{T}_{x_j}(\mathbf{p}) = \Gamma_{x_j}(\mathbf{p})\Gamma_{\mathrm{v}}^{-1}(\mathbf{p}), \tag{6.19}$$

$$\Gamma_{x_j}(\mathbf{p}) \stackrel{\Delta}{=} C_{x_j}\mathrm{adj}(\mathbf{p}I - A)B, \tag{6.20}$$

and Γ_{v} is as defined in (6.6). Note that Γ_{x_j} is also a polynomial of $\mathbf{p}$.

Similar to the interpretation of $\mathscr{T}$ in (6.10), substitute (6.19) in (6.18), and then $\mathscr{T}_{x_j}$ from (6.18) can be interpreted as

$$x_j(t) = \frac{c_{j,n-1}\mathbf{p}^{n-1} + \cdots + c_{j,1}\mathbf{p} + c_{j,0}}{a_n\mathbf{p}^n + \cdots + a_1\mathbf{p} + a_0}v(t). \tag{6.21}$$

Notice that (6.12) and (6.21) have the same characteristic equation since both have the same pseudo input v. Therefore, both (6.12) and (6.21) should share the same pseudo state vector z. Substitute (6.12) in (6.21) yields

$$x_j(t) = \Gamma_{x_j}(\mathbf{p})\bar{y}(t) = \left[c_{j,n-1}\mathbf{p}^{n-1} + \cdots + c_{j,1}\mathbf{p} + c_{j,0}\right]\bar{y}(t). \tag{6.22}$$

Recall the definition of the pseudo states z as $z_i = \mathbf{p}^{i-1}\bar{y}$ for all $i \in \{1,\ldots,n\}$, thus interpreting (6.21) in terms of z yields

$$x_j(t) = c_{j,0}z_1(t) + \cdots + c_{j,n-1}z_n(t). \tag{6.23}$$

Therefore, the complete transmissibility relationship between v, y, and x can be written as

$$\dot{z}_i(t) = z_{i+1}(t), \;\; i \in \{1,\ldots,n-1\}, \tag{6.24}$$

$$\dot{z}_n(t) = \Phi(t,z,v), \tag{6.25}$$

$$\bar{y}(t) = z_1(t), \tag{6.26}$$

$$x_j(t) = \bar{C}_j z(t), \;\; j \in \{1,\ldots,n\}, \tag{6.27}$$

where

$$\bar{C}_j = \begin{bmatrix} c_{j,0} & \ldots & c_{j,n-1} \end{bmatrix}. \tag{6.28}$$

6.2.2 High-gain Transmissibility

The aim of HGT is to obtain an accurate estimation of the pseudo state vector z based on real-time measurements of y. Therefore, we add a high-gain term to the state-space model

(6.24)-(6.27) such as

$$\dot{\hat{z}}_i(t) = \hat{z}_{i+1}(t) + \frac{\alpha_i}{\varepsilon^i}(\bar{y} - \hat{z}_1), \tag{6.29}$$

$$\dot{\hat{z}}_n(t) = \frac{\alpha_n}{\varepsilon^n}(\bar{y} - \hat{z}_1), \tag{6.30}$$

$$\hat{x}_j(t) = \bar{C}_j \hat{z}(t), \tag{6.31}$$

where ε is sufficiently small, and $\alpha_1, \ldots, \alpha_n$ are chosen such that the polynomial

$$\mathbf{p}^n + \alpha_1 \mathbf{p}^{n-1} + \cdots + \alpha_{n-1}\mathbf{p} + \alpha_n, \tag{6.32}$$

is Hurwitz. The variable $\dot{\hat{z}}_n$ in (6.31) is computed as the first derivative of the estimation of $\hat{z}_n$ not directly from (6.30). The boundedness of the estimation error of the pseudo states $\hat{z}$, and accordingly, the boundedness of the estimation error of the states $\hat{x}$ are investigated within the general statement in Section 6.4.

6.2.3 Illustration Example

Consider the system in (A.10)-(A.11) with $n = 2, m = 1$, and the parameters

$$A = \begin{bmatrix} 1 & 2 \\ -2 & -3 \end{bmatrix}, \quad B = \begin{bmatrix} 2 \\ 1 \end{bmatrix}, \quad C = \begin{bmatrix} 2 & 1.5 \end{bmatrix}. \tag{6.33}$$

Such that, A is Hurwitz, B to let f act on all states, and C does not measure any states directly. The system has one real zero -1.55. Next, to design the HGT in (6.29)-(6.31) we need to obtain $\bar{y}$ from y, and compute the coefficients $\bar{C}_j$ for $j \in \{1,2\}$. To compute $\bar{y}$, Γ_y can be obtained from (6.7) as $\Gamma_y(\mathbf{p}) = 5.5\mathbf{p} + 8.5$. Notice that the zeros of Γ_y are the same as the original system zeros. Then $\bar{y}$ can be computed from (6.11) as

$$\bar{y}(t) = \frac{1}{5.5\mathbf{p} + 8.5} y(t). \tag{6.34}$$

Next, the coefficients $\bar{C}_j$ can be computed by computing Γ_{x_j} from (6.20) for all $j \in \{1,2\}$. Define $C_{x_1} = \begin{bmatrix} 1 & 0 \end{bmatrix}$, and $C_{x_2} = \begin{bmatrix} 0 & 1 \end{bmatrix}$. Then from (6.20) $\Gamma_{x_1}(\mathbf{p}) = 2\mathbf{p} + 8$ and $\Gamma_{x_2}(\mathbf{p}) = \mathbf{p} - 5$. Thus, $\bar{C}_1 = \begin{bmatrix} 8 & 2 \end{bmatrix}$ and $\bar{C}_2 = \begin{bmatrix} -5 & 1 \end{bmatrix}$. Setting $\alpha_1 = \alpha_2 = 1$ satisfies (6.32). Then

the designed HGT can be given as

$$\dot{\hat{z}}_1(t) = \hat{z}_2(t) + \frac{1}{\varepsilon}(\bar{y} - \hat{z}_1), \tag{6.35}$$

$$\dot{\hat{z}}_2(t) = \frac{1}{\varepsilon^2}(\bar{y} - \hat{z}_1), \tag{6.36}$$

$$\hat{x}_1(t) = \begin{bmatrix} 8 & 2 \end{bmatrix} \hat{z}(t), \tag{6.37}$$

$$\hat{x}_2(t) = \begin{bmatrix} -5 & 1 \end{bmatrix} \hat{z}(t). \tag{6.38}$$

6.3 High-gain Observers - Special Case

This section illustrates the relationship between HGT and High-gain Observers (HGO). We assume a linear system where both HGT and HGO are applicable, then shows how the same HGO can be obtained using HGT. Assume the following linear chain of integrator that follows the canonical form, all states being uncertain, and high-gain observers are applied directly

$$\dot{x}_i = x_{i+1}, \tag{6.39}$$

$$\dot{x}_n = \sum_{j=1}^{n} a_{j-1} x_j + u, \tag{6.40}$$

$$y = x_1. \tag{6.41}$$

Design a high-gain observer

$$\dot{\hat{x}}_i = \hat{x}_{i+1} + \frac{\alpha_i}{\varepsilon^i}\left[\hat{x}_1 - x_1\right], \tag{6.42}$$

$$\dot{\hat{x}}_n = \frac{\alpha_n}{\varepsilon^n}\left[\hat{x}_1 - x_1\right]. \tag{6.43}$$

Next, design a HGT for the same system (6.39)-(6.41). Define the system's state space matrices such that

$$A = \begin{bmatrix} 0 & 1 & \dots & 0 \\ \vdots & \ddots & \ddots & \vdots \\ 0 & \dots & 0 & 1 \\ a_0 & a_1 & \dots & a_{n-1} \end{bmatrix}, \tag{6.44}$$

$$B = \begin{bmatrix} 0 & \dots & 0 & 1 \end{bmatrix}^{\mathrm{T}}, \tag{6.45}$$

$$C = \begin{bmatrix} 1 & 0 & \dots & 0 \end{bmatrix}. \tag{6.46}$$

Define the virtual signal v to match the observer input u such as

$$v = \underbrace{\begin{bmatrix} 0 & \dots & 0 \end{bmatrix}}_{C_{\mathrm{v}}} x + \underbrace{\begin{bmatrix} 1 \end{bmatrix}}_{D_{\mathrm{v}}} u. \tag{6.47}$$

A question might arise here for the reader since v was mentioned earlier not to be required in the proposed method. The definition of v in this section is to illustrate the connection between HGT and HGO, and v will not be used in the final design of HGT. Following (6.6) and (6.7) obtain

$$\Gamma_{\mathrm{v}}(\mathbf{p}) = \mathbf{p}^n + a_{n-1}\mathbf{p}^{n-1} + \cdots + a_0, \tag{6.48}$$

$$\Gamma_{\mathrm{y}}(\mathbf{p}) = 1. \tag{6.49}$$

Using the certain dynamics define the certain output as in (6.11)

$$\bar{y} = \frac{1}{\Gamma_{\mathrm{y}}(\mathbf{p})} y = y. \tag{6.50}$$

Then the transmissibility operator from v to y can be written as

$$\bar{y} = y = \frac{1}{\Gamma_{\mathrm{v}}(\mathbf{p})} v = \frac{1}{\mathbf{p}^n + a_{n-1}\mathbf{p}^{n-1} + \cdots + a_0} v, \tag{6.51}$$

which can be interpreted to the chain of integrators

$$\dot{z}_i = z_{i+1}, \tag{6.52}$$

$$\dot{z}_n = \sum_{j=1}^{n} a_{j-1} z_i + v, \tag{6.53}$$

$$\bar{y} = y = z_1. \tag{6.54}$$

Design the HGT

$$\dot{\hat{z}}_i = \hat{z}_{i+1} + \frac{\alpha_i}{\varepsilon^i}\left[\hat{z}_1 - z_1\right], \tag{6.55}$$

$$\dot{\hat{z}}_n = \frac{\alpha_n}{\varepsilon^n}\left[\hat{z}_1 - z_1\right]. \tag{6.56}$$

Recall the states definition as independent outputs

$$x_j = \underbrace{\begin{bmatrix} 0 & \dots & 1 & \dots & 0 \end{bmatrix}}_{C_{x_j}} x. \tag{6.57}$$

For all $j \in \{1, \dots, n\}$, define Γ_{x_j} from (6.19)

$$\Gamma_{x_j}(\mathbf{p}) = \mathbf{p}^{j-1}. \tag{6.58}$$

Substitute (6.58) and (6.54) in (6.22) yields

$$x_j = \mathbf{p}^{j-1} z_1, \tag{6.59}$$

which indicates that $x_j = z_j$ for all $j \in \{1, \dots, n\}$. Another way to obtain the relationship between x and z for the system (6.39)-(6.41) is directly from (6.57) such as

$$x_1 = \begin{bmatrix} 1 & 0 & \dots & 0 \end{bmatrix} x = y = z_1, \tag{6.60}$$

$$x_2 = \begin{bmatrix} 0 & 1 & \dots & 0 \end{bmatrix} x = \mathbf{p} z_1 = z_2, \tag{6.61}$$

$$\vdots \tag{6.62}$$

$$x_n = \begin{bmatrix} 0 & 0 & \dots & 1 \end{bmatrix} x = \mathbf{p}^{n-1} z_1 = z_n. \tag{6.63}$$

Substitute $z = x$ and $v = u$ in the designed HGT in (6.55)-(6.56) yields

$$\hat{\dot{x}}_i = \hat{x}_{i+1} + \frac{\alpha_i}{\varepsilon^i}\left[\hat{x}_1 - x_1\right], \tag{6.64}$$

$$\hat{\dot{x}}_n = \frac{\alpha_n}{\varepsilon^n}\left[\hat{x}_1 - x_1\right], \tag{6.65}$$

which matches the HGO designed in (6.42)-(6.43). Notice that even the uncertain part that is eliminated due to the high gain matches. The previous conclusion indicates that if HGOs are applicable, the virtual design signal is set as the observer input, then both HGT and HGO are identical.

6.4 General Statement

This section generalizes HGT on the system (A.10)-(A.11) with multiple nonlinearities acting on the system at the same time, that is, $f \in \mathbb{R}^m$ where $m \geq 2$. Recall the transmissibility relation in (6.4)

$$y(t) = \mathscr{T}(\mathbf{p})v(t), \tag{6.66}$$

where

$$v(t) = \begin{bmatrix} v_1(t) & \dots & v_m(t) \end{bmatrix}^{\mathrm{T}} \in \mathbb{R}^m, \tag{6.67}$$

$$y(t) = \begin{bmatrix} y_1(t) & \dots & y_m(t) \end{bmatrix}^{\mathrm{T}} \in \mathbb{R}^m, \tag{6.68}$$

$$\mathscr{T}(\mathbf{p}) = \Gamma_{\mathrm{y}}(\mathbf{p})\Gamma_{\mathrm{v}}^{-1}(\mathbf{p}), \tag{6.69}$$

$$\Gamma_{\mathrm{v}}(\mathbf{p}) \triangleq C_{\mathrm{v}}\mathrm{adj}(\mathbf{p}I - A)B + D_{\mathrm{v}}\delta(\mathbf{p}) \in \mathbb{R}^{m\times m}[\mathbf{p}], \tag{6.70}$$

$$\Gamma_{\mathrm{y}}(\mathbf{p}) \triangleq C\mathrm{adj}(\mathbf{p}I - A)B \in \mathbb{R}^{m\times m}[\mathbf{p}], \tag{6.71}$$

$$\delta(\mathbf{p}) \triangleq \det(\mathbf{p}I - A). \tag{6.72}$$

Note that Γ_{v} and Γ_{y} are square matrices with dimension m.

6.4.1 State Space Representation of Transmissibilities

By substituting (6.69) in (6.4), the operator $\mathscr{T}$ can be interpreted as

$$\Gamma_{\mathrm{y}}^{-1}(\mathbf{p})y(t) = \Gamma_{\mathrm{v}}^{-1}(\mathbf{p})v(t). \tag{6.73}$$

Define

$$\underbrace{\begin{bmatrix} \bar{y}_1(t) \\ \vdots \\ \bar{y}_m(t) \end{bmatrix}}_{\bar{y}(t)} = \underbrace{\begin{bmatrix} \Gamma_{\mathrm{y},1,1} & \dots & \Gamma_{\mathrm{y},1,m} \\ \vdots & \ddots & \vdots \\ \Gamma_{\mathrm{y},m,1} & \dots & \Gamma_{\mathrm{y},m,m} \end{bmatrix}^{-1}}_{\Gamma_{\mathrm{y}}^{-1}(\mathbf{p})} \underbrace{\begin{bmatrix} y_1(t) \\ \vdots \\ y_m(t) \end{bmatrix}}_{y(t)}. \tag{6.74}$$

Assumption 1 guarantees that the relation from y to $\bar{y}$ is always stable. Substitute (6.74) in (6.73) to get

$$\underbrace{\begin{bmatrix} \bar{y}_1(t) \\ \vdots \\ \bar{y}_m(t) \end{bmatrix}}_{\bar{y}(t)} = \underbrace{\begin{bmatrix} \Gamma_{\mathrm{v},11} & \dots & \Gamma_{\mathrm{v},1,m} \\ \vdots & \ddots & \vdots \\ \Gamma_{\mathrm{v},m,1} & \dots & \Gamma_{\mathrm{v},m,m} \end{bmatrix}^{-1}}_{\Gamma_{\mathrm{v}}^{-1}(\mathbf{p})} \underbrace{\begin{bmatrix} v_1(t) \\ \vdots \\ v_m(t) \end{bmatrix}}_{v(t)} \tag{6.75}$$

which represents the uncertain dynamics.

6.4.2 Output-State Relationships

Recall the definition of the states in (6.17) as independent outputs of the system (A.10) for all $j \in \{1,\dots,n\}$, similar to (6.66), the relationship from the virtual output v to the output x_j can be given as

$$x_j(t) = \mathscr{T}_{x_j}(\mathbf{p})v(t), \tag{6.76}$$

where

$$\mathscr{T}_{x_j}(\mathbf{p}) = \Gamma_{x_j}(\mathbf{p})\Gamma_{\mathrm{v}}^{-1}(\mathbf{p}), \tag{6.77}$$

$$\begin{aligned} \Gamma_{x_j}(\mathbf{p}) &\stackrel{\Delta}{=} C_{x_j}\mathrm{adj}(\mathbf{p}I - A)B \in \mathbb{R}^{1\times m}[\mathbf{p}] \\ &= \begin{bmatrix} \Gamma_{x_j,1}(\mathbf{p}) & \dots & \Gamma_{x_j,m}(\mathbf{p}) \end{bmatrix}, \end{aligned} \tag{6.78}$$

Γ_{v} is as defined in (6.70), and C_{x_j} is as defined in (6.17) where the cell with number 1 is the jth index. Thus for all $j \in \{1,\dots,n\}$, the relationship from v to x_j

$$x_j(t) = \Gamma_{x_j}(\mathbf{p})\Gamma_{\mathrm{v}}^{-1}(\mathbf{p})v(t). \tag{6.79}$$

Substitute (6.75) in (6.79) yields for all $j \in \{1,\ldots,n\}$

$$x_j(t) = \begin{bmatrix} \Gamma_{x_j,1}(\mathbf{p}) & \ldots & \Gamma_{x_j,m}(\mathbf{p}) \end{bmatrix} \begin{bmatrix} \bar{y}_1(t) \\ \vdots \\ \bar{y}_m(t) \end{bmatrix}, \tag{6.80}$$

which can be interpreted as

$$x_j(t) = \sum_{\ell=1}^{m} \left[c_{j,\ell,n-1}\mathbf{p}^{n-1} + \cdots + c_{j,\ell,1}\mathbf{p} + c_{j,\ell,0} \right] \bar{y}(t). \tag{6.81}$$

Recall the definition of the pseudo states z as $z_{\ell,i} = \mathbf{p}^{i-1}\bar{y}_\ell$ for all $i \in \{1,\ldots,n\}$ and $\ell \in \{1,\ldots,m\}$, thus interpreting (6.81) in terms of z yields

$$x_j(t) = \sum_{\ell=1}^{m} \left[c_{j,\ell,0}z_{\ell,1}(t) + \cdots + c_{j,\ell,n-2}z_{\ell,n-1}(t) \right]. \tag{6.82}$$

Therefore, the complete transmissibility relationship between v, y, and x can be written as the following series of chains of integrators for all $\ell \in \{1,\ldots,m\}$

$$\dot{z}_{\ell,i}(t) = z_{\ell,i+1}(t), \;\; i \in \{1,\ldots,n-1\}, \tag{6.83}$$

$$\dot{z}_{\ell,n}(t) = \Phi(t, z_\ell, v_\ell), \tag{6.84}$$

$$\bar{y}_\ell(t) = z_{\ell,1}(t), \tag{6.85}$$

$$x_j(t) = \sum_{\ell=1}^{m} \bar{C}_{j,\ell} z_\ell(t), \;\; j \in \{1,\ldots,n\}, \tag{6.86}$$

where Φ is as defined under (6.16),

$$z_\ell = \begin{bmatrix} z_{\ell,1} & \ldots & z_{\ell,n} \end{bmatrix}, \tag{6.87}$$

$$\bar{C}_{j,\ell} = \begin{bmatrix} c_{j,\ell,0} & \ldots & c_{j,\ell,n-1} \end{bmatrix}. \tag{6.88}$$

6.4.3 High-gain Transmissibility

Adding high-gain terms to the state-space model (6.83)-(6.84) such as

$$\dot{\hat{z}}_{\ell,i}(t) = \hat{z}_{\ell,i+1}(t) + \frac{\alpha_{\ell,i}}{\varepsilon^i}[\bar{y}_\ell - \hat{z}_{\ell,1}], \;\; i \in \{1,\ldots,n-1\}, \tag{6.89}$$

$$\dot{\hat{z}}_{\ell,n}(t) = \frac{\alpha_{\ell,n}}{\varepsilon^n}[\bar{y}_\ell - \hat{z}_{\ell,1}], \tag{6.90}$$

$$\hat{x}_j(t) = \sum_{\ell=1}^{m} \bar{C}_{j,\ell}\hat{z}_\ell(t), \;\; j \in \{1,\ldots,n\}, \tag{6.91}$$

where ε is sufficiently small, and for all $\ell \in \{1,\ldots,m\}$ $\alpha_{\ell,1},\ldots,\alpha_{\ell,n}$ are chosen such that the polynomial

$$\mathbf{p}^n + \alpha_{\ell,1}\mathbf{p}^{n-1} + \cdots + \alpha_{\ell,n-1}\mathbf{p} + \alpha_n, \tag{6.92}$$

is Hurwitz. The next theorem investigates the boundedness of the estimation error of the states $\hat{x}$.

Theorem 2. There exists ε^* such that for $0 < \varepsilon \leq \varepsilon^*$ the estimation error $\tilde{z}_i^\ell = z_i^\ell - \hat{z}_i^\ell$, for all $1 \leq i \leq n$ and $\ell \in \{1,\ldots,m\}$, satisfies the bound

$$|\tilde{z}_{\ell,i}| \leq \max\left\{\frac{b}{\varepsilon^{i-1}}||\tilde{z}(0)||e^{-at/\varepsilon}, \varepsilon^{n-i+1}cM_{\max}\right\}, \tag{6.93}$$

for some positive a,b,c and $M_{\max} = \max\{M_1,\ldots,M_m\}$.

Theorem 2 Proof: Define the scaled estimation errors for all $i \in \{1,\ldots,n\}$ and $\ell \in \{1,\ldots,m\}$

$$\eta_{\ell,i} = \frac{z_{\ell,i} - \hat{z}_{\ell,i}}{\varepsilon^{n-i}}. \tag{6.94}$$

Subtract (6.29)-(6.30) from (6.24)-(6.25) yields

$$\varepsilon^{n-i}\dot{\eta}_{\ell,i} = \varepsilon^{n-i-1}\eta_{\ell,i+1} - \frac{\alpha_{\ell,i}}{\varepsilon^i}\varepsilon^{n-1}\eta_{\ell,1}, \tag{6.95}$$

$$\dot{\eta}_{\ell,n} = \Phi(t,z_\ell,v_\ell) - \frac{\alpha_{\ell,n}}{\varepsilon^n}\varepsilon^{n-1}\eta_{\ell,1}. \tag{6.96}$$

The error dynamics for the ℓth chain of integrators can then be written as

$$\varepsilon\dot{\eta}_\ell = E_\ell\eta_\ell + \varepsilon F_\ell\Phi(t,z_\ell,v_\ell), \tag{6.97}$$

where

$$\eta_\ell = \begin{bmatrix} \eta_{\ell,1} & \dots & \eta_{\ell,n} \end{bmatrix}^{\mathrm{T}},$$

$$E_\ell = \begin{bmatrix} -\alpha_{\ell,1} & 1 & 0 & \dots & 0 \\ -\alpha_{\ell,2} & 0 & 1 & \dots & 0 \\ \vdots & & \ddots & \ddots & \\ -\alpha_{\ell,n-1} & & & 0 & 1 \\ -\alpha_{\ell,n} & 0 & & \dots & 0 \end{bmatrix},$$

$$F_\ell = \begin{bmatrix} 0 & \dots & 0 & 1 \end{bmatrix}^{\mathrm{T}}.$$

Note that E_ℓ is Hurwitz by design based on the condition in (6.92). Assume Φ to be locally Lipschitz in its arguments and

$$|\Phi(t, z_\ell, v_\ell)| \leq L_\ell ||z_\ell - \hat{z}_\ell|| + M_\ell \leq L_\ell \sum_{\ell=1}^{m} ||\eta_\ell|| + M_\ell, \tag{6.98}$$

where for all $\ell \in \{1, \dots, m\}$ L_ℓ and M_ℓ are positive constants. Define the Lyapunov function

$$V = \sum_{\ell=1}^{m} \eta_\ell^{\mathrm{T}} P_\ell \eta_\ell, \tag{6.99}$$

where P_ℓ is the solution of the Layaponov equation

$$P_\ell E_\ell + E_\ell^{\mathrm{T}} P_\ell = -I. \tag{6.100}$$

Take the derivative of V

$$\varepsilon \dot{V} = \sum_{\ell=1}^{m} \left[-\eta_\ell^{\mathrm{T}} \eta_\ell + 2\varepsilon \eta_\ell^{\mathrm{T}} P_\ell F_\ell \Phi(t, z_\ell, v_\ell) \right]. \tag{6.101}$$

Then from (6.98) we obtain

$$\varepsilon \dot{V} \leq \sum_{\ell=1}^{m} \left[-||\eta_\ell||^2 + 2\varepsilon ||\eta_\ell|| \, ||P_\ell F_\ell|| \left(L_\ell \sum_{\ell=k}^{m} ||\eta_k|| + M_\ell \right) \right]. \tag{6.102}$$

Define

$$\psi = \begin{bmatrix} ||\eta_1|| & \dots & ||\eta_m|| \end{bmatrix}^{\mathrm{T}},$$
$$\theta = \begin{bmatrix} ||P_1F_1|| & \dots & ||P_mF_m|| \end{bmatrix}^{\mathrm{T}},$$

and the symmetric matrix N, where for all $k \in \{1,\dots,m\}, l \in \{1,\dots,m\}$ the (k,l) entry of N is defined as

$$N_{(k,l)} = ||P_kF_k||L_k + ||P_lF_l||L_l.$$

Then (6.101) can be written as

$$\varepsilon\dot{V} = -\psi^{\mathrm{T}}\psi + \varepsilon\psi^{\mathrm{T}}N\psi + 2\varepsilon M_{\max}\theta^{\mathrm{T}}\psi. \tag{6.103}$$

For $\varepsilon||N|| \leq \frac{1}{2}$

$$\varepsilon\dot{V} \leq -\frac{1}{2}||\psi||^2 + 2\varepsilon M_{\max}||\theta||\,||\psi||. \tag{6.104}$$

Let $\eta = \mathrm{col}(\eta_1,\dots,\eta_m)\}$ and notice that $||\psi|| = ||\eta||$, then

$$\varepsilon\dot{V} \leq -\frac{1}{2}||\eta||^2 + 2\varepsilon M_{\max}||\theta||\,||\eta||. \tag{6.105}$$

Therefore, $||\eta||$ is ultimately bounded by $\varepsilon c M_{\max}$ for $c > 0$, and

$$||\eta(t)|| \leq \max\left\{be^{-at/\varepsilon}||\eta(0)||, \varepsilon c M_{\max}\right\}, \tag{6.106}$$

for some positive constants a, b. From (6.94) we can see that $\tilde{z}_{\ell,i} = \varepsilon^{n-i}\eta_{\ell,i}$ and $||\eta(0)|| \leq ||z(0) - \hat{z}(0)||/\varepsilon^{n-1}$. Thus, (6.106) becomes

$$|\tilde{z}_{\ell,i}| \leq \max\left\{\frac{b}{\varepsilon^{i-1}}||\tilde{z}(0)||e^{-at/\varepsilon}, \varepsilon^{n-i+1}cM_{\max}\right\}. \quad \square \tag{6.107}$$

6.5 Numerical Example

This example simulates a two vehicles portion of a connected autonomous vehicles platoon shown in Figure 6.1 that is subjected to hysteresis nonlinearities as well as nonlinear ground friction. The two vehicle share kinematics information through a wireless communication link, which are used to control their velocities and spacing distance. The aim is to estimate

the vehicles' velocities (v_1, v_2) and spacing distances h_1, h_2 from outside the platoon. The outputs considered from outside are the average velocity of both vehicles and the second vehicle position p_2.

6.5.1 System Model

Let the index $\kappa \in \{1,2\}$ refer to the vehicle order, then vehicle κ can be modeled as

$$\dot{h}_\kappa(t) = v_{\kappa-1}(t, v^*) - v_\kappa(t), \tag{6.108}$$

$$\dot{v}_\kappa(t) = \zeta_\kappa h_\kappa(t) + \beta_\kappa v_\kappa(t) + \tau_\kappa v_{\kappa-1}(t) + \gamma_\kappa f_2(t, v), \tag{6.109}$$

where $h_\kappa = p_\kappa - p_{\kappa-1}$, p_κ is κth vehicle position, v^*_κ is the κth vehicle desired velocity, $p_0 = 0$ is a reference point, and $\zeta_\kappa, \beta_\kappa, \tau_\kappa, \gamma_\kappa$ are constants. v_0 is set as the desired velocity of the platoon such that $v_0 = f_1(t, v^*)$ that changes randomly. $f_2(\cdot,\cdot)$ is the friction force that is given as (Dahl friction)

$$\begin{aligned} f_2(t,v) = \int \sigma \,|1 - f_2(t,v)v(t)| \\ \operatorname{sgn}(1 - f_2(t,v)v(t))\, v(t).\mathbf{d}t, \end{aligned} \tag{6.110}$$

where $\sigma = 750$, and v is the average velocity of both vehicles. Note that f_2 is only defined here to generate it numerically, and is not used after to estimate the states. The overall system model then can be arranged by setting the state vector as $x(t) = \begin{bmatrix} h_1(t) & v_1(t) & h_2(t) & v_2(t) \end{bmatrix}^{\mathrm{T}}$ and the output vector to $y(t) = \begin{bmatrix} v(t) & p_2(t) \end{bmatrix}^{\mathrm{T}}$ as in (A.10)-(A.11) where

$$A = \begin{bmatrix} 0 & -1 & 0 & 0 \\ \zeta_1 & \beta_1 & 0 & 0 \\ 0 & 1 & 0 & -1 \\ 0 & \tau_2 & \zeta_2 & \beta_2 \end{bmatrix}, \tag{6.111}$$

$$B = \begin{bmatrix} 1 & \tau_1 & 0 & 0 \\ 0 & \gamma_1 & 0 & \gamma_2 \end{bmatrix}^{\mathrm{T}}, \tag{6.112}$$

$$C = \begin{bmatrix} 0 & 0.5 & 0 & 0.5 \\ 1 & 0 & 1 & 0 \end{bmatrix}, \tag{6.113}$$

$$f(t,x,v^*) = \begin{bmatrix} f_1(t,v^*) \\ f_2(t,v) \end{bmatrix}. \tag{6.114}$$

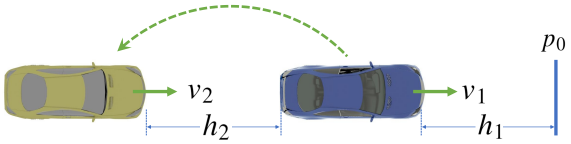

Fig. 6.1 Numerical Example: A two autonomous vehicles portion of a platoon. The average velocity and second vehicle's position are used to estimate the vehicles' velocities (v_1, v_2) and spacing distances (h_1, h_2).

The constants are set to $\zeta_1 = \zeta_2 = 0.33, \beta_1 = \beta_2 = -0.45, \tau_1 = \tau_2 = 0.25, \gamma_1 = 0.0008$, and $\gamma_2 = 0.0006$. For clarity, the notation of the states will be set as $x(t) = \begin{bmatrix} h_1(t) & v_1(t) & h_2(t) & v_2(t) \end{bmatrix}^{\mathrm{T}} = \begin{bmatrix} x_1(t) & \dots & x_4(t) \end{bmatrix}^{\mathrm{T}}$, and the outputs $y(t) = \begin{bmatrix} v(t) & p_2(t) \end{bmatrix}^{\mathrm{T}} = \begin{bmatrix} y_1(t) & y_2(t) \end{bmatrix}^{\mathrm{T}}$.

The system (6.111)-(6.114) satisfy the assumptions on the system (A.10)-(A.11) such that: the state matrix A is Hurwitz, the nonlinear functions in f are bounded and locally Lipschitz, the number of measured outputs y is equal or greater than the number of signals in f. Moreover, the system zeros are -0.35 ± 0.738, which satisfies Assumption 1.

6.5.2 State Estimation using HGT

The system has two nonlinear functions acting on it $m = 2$, thus the general statement in Section 6.4 will be used. To design the HGT in (6.89)-(6.91), we need to compute $\bar{y}_\ell$ from y_ℓ for all $\ell \in \{1,2\}$. Moreover, we need to compute the coefficients $\bar{C}_{j,\ell}$ for all for all $j \in \{1,\dots,4\}$ and $\ell \in \{1,2\}$.

To compute $\bar{y}_\ell$, we need to compute Γ_{y} from (6.71) and then implement (6.74). Using (6.111)-(6.113), Γ_{y} can be computed as

$$\Gamma_{\mathrm{y},1,1}(\mathbf{p}) = 0.125\mathbf{p}^3 + 0.25\mathbf{p}^2 + 0.2\mathbf{p} + 0.11, \tag{6.115}$$

$$\Gamma_{\mathrm{y},1,2}(\mathbf{p}) = 0.00073\mathbf{p}^3 + 0.00043\mathbf{p}^2 + 0.00038\mathbf{p}, \tag{6.116}$$

$$\Gamma_{\mathrm{y},2,1}(\mathbf{p}) = \mathbf{p}^3 + 0.9\mathbf{p}^2 + 0.81\mathbf{p} + 0.13, \tag{6.117}$$

$$\Gamma_{\mathrm{y},2,2}(\mathbf{p}) = -0.00063\mathbf{p}^2 - 0.00049\mathbf{p} - 0.00049. \tag{6.118}$$

Next, the coefficients of $\bar{C}_{j,\ell}$ are the same as the coefficients of Γ_{x_j} computed from (6.78) but with a flipped order. C_{x_j} is as defined in (6.17) where the cell with number 1 is the jth index.

Using A, B in (6.111)-(6.112) along with C_{x_j} for all $j \in \{1,\ldots,4\}$ we can obtain from (6.78)

$$\Gamma_{x_1,1}(\mathbf{p}) = \mathbf{p}^3 + 0.65\mathbf{p}^2 + 0.42\mathbf{p} + 0.067, \tag{6.119}$$
$$\Gamma_{x_1,2}(\mathbf{p}) = -0.00083\mathbf{p}^2 - 0.000375\mathbf{p} - 0.00028, \tag{6.120}$$
$$\Gamma_{x_2,1}(\mathbf{p}) = 0.25\mathbf{p}^3 + 0.45\mathbf{p}^2 + 0.23\mathbf{p} + 0.11, \tag{6.121}$$
$$\Gamma_{x_2,2}(\mathbf{p}) = 0.00083\mathbf{p}^3 + 0.000375\mathbf{p}^2 + 0.00028\mathbf{p}, \tag{6.122}$$
$$\Gamma_{x_3,1}(\mathbf{p}) = 0.25\mathbf{p}^2 + 0.38\mathbf{p} + 0.067, \tag{6.123}$$
$$\Gamma_{x_3,2}(\mathbf{p}) = 0.00021\mathbf{p}^2 - 0.00011\mathbf{p} - 0.00021, \tag{6.124}$$
$$\Gamma_{x_4,1}(\mathbf{p}) = 0.0625\mathbf{p}^2 + 0.17\mathbf{p} + 0.11, \tag{6.125}$$
$$\Gamma_{x_4,2}(\mathbf{p}) = 0.000625\mathbf{p}^3 + 0.00049\mathbf{p}^2 + 0.00049\mathbf{p}. \tag{6.126}$$

Then $\bar{C}_{j,\ell}$ is a vector of the coefficients of the polynomial $\Gamma_{x_j,\ell}$ but from right to left. For example, from (6.123) we can obtain $\bar{C}_{3,1} = \begin{bmatrix} 0.067 & 0.38 & 0.25 & 0 \end{bmatrix}$. Note that the order of $\bar{C}_{j,\ell}$ must equal the order of the original system n, thus a third order differential operator $\mathbf{p}$ is added with coefficient zero. The order of all polynomials in Γ_{y} and Γ_{x_j} have less order than the order of the system $n = 4$ due to the definition of the virtual signal v.

Next, we design the HGT in (6.89)-(6.91). Since $m = 2$, two chains of integrators are needed, that is, $\ell \in \{1,2\}$. The high-gain terms' coefficients are set according to the condition under (6.92) as $\alpha_{1,1} = \alpha_{2,1} = 4$, $\alpha_{1,2} = \alpha_{2,2} = 3$, $\alpha_{1,3} = \alpha_{2,3} = 2$, and $\alpha_{1,4} = \alpha_{2,4} = 1$. The sufficiently small coefficient is set to $\varepsilon = 0.001$ for the entire experiment.

We run the system by setting the desired velocity of the platoon $f_1(\cdot,\cdot)$ to the nonlinear function shown in upper part of Figure 6.2. The initial conditions of all states are set to 5. The lower part of Figure 6.2 shows the friction force $f_2(\cdot,\cdot)$ generated due to the vehicles movements. Figure 6.3 shows the actual and estimated states of the system, while the estimation errors on x are plotted in Figure 6.4. Notice from Figure 6.4 that the estimation error on all states decay to zero. Moreover, non of the nonlinear functions in f is used to estimated the states in Figure 6.3.

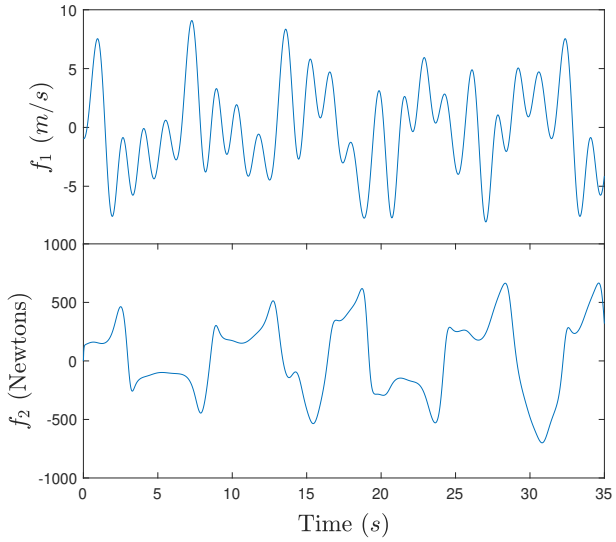

Fig. 6.2 Numerical Example: The nonlinear functions used to simulate the system. f_1 is the desired velocity of the platoon that is set to a random smooth signal, and f_2 is the unknown friction generated on each of the vehicles. f_1 acts on x_1, x_2, and f_2 acts on x_2, x_4 at the same time.

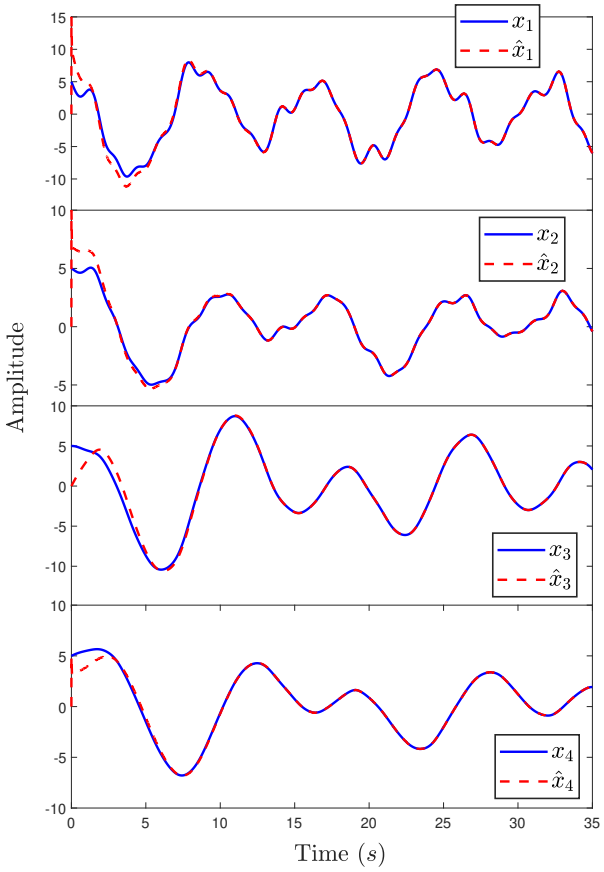

Fig. 6.3 Numerical Example: The actual states and their HGT-based estimations of the platoon shown in Figure 6.1. Note that the nonlinear functions in Figure 6.2 are not used to estimated any of the states.

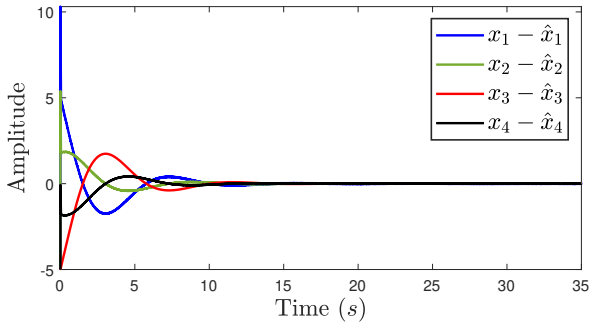

Fig. 6.4 Numerical Example: The estimation error on each of the states $x_1, \ldots, x_4$ estimated in Figure 6.3.

Chapter 7

Transmissibility-based Kalman Filter for Systems Under Non-Gaussian Process Noise

7.1 Problem Formulation

Consider the following smooth nonlinear system

$$x(k+1) = Ax(k) + B_f f(k,x,u) + B_w w(k), \tag{7.1}$$

$$y_{\mathrm{i}}(k) = C_{\mathrm{i}} x(k) + \delta_{\mathrm{i}}(k), \tag{7.2}$$

$$y_{\mathrm{o}}(k) = C_{\mathrm{o}} x(k) + \delta_{\mathrm{o}}(k), \tag{7.3}$$

where $A \in \mathbb{R}^{n\times n}$ is Hurwitz, $B_f \in \mathbb{R}^{n\times m_1}, B_w \in \mathbb{R}^{n\times m_2}$, $C_{\mathrm{i}} \in \mathbb{R}^{(m_1+m_2)\times n}, C_{\mathrm{o}} \in \mathbb{R}^{p\times n}$, $f(\cdot,\cdot,\cdot)$ is a vector of unknown bounded nonlinear functions where u is a set of unknown system inputs, and w is a vector of non-Gaussian process noise (external disturbances).

y_{i} and y_{o} are two independent sets of outputs that are subjected to Gaussian measurements noise $\delta_{\mathrm{i}} \in \mathbb{R}^{m_1+m_2}$ and $\delta_{\mathrm{o}} \in \mathbb{R}^{p}$, respectively. The aim of this work is to design a Kalman filter that minimizes the noise at the output of interest y_{o}. In this work, we consider the following conditions where the typical Kalman filter cannot be applied on the system (7.1)-(7.3)

- Unknown inputs u. The estimation of Kalman filter requires full knowledge of the system inputs.
- Unknown nonlinear dynamics in the system $f(\cdot,\cdot,\cdot)$. The nonlinear function f must be known and can be linearized to apply the extended Kalman filter.

- Non Gaussian external disturbances w. The computations of the estimation error covarinace matrix necessitate w to have Gaussian distribution.

Multi-agent systems are great examples on systems subjected to the above three conditions. The first condition might occur where each agent needs to adapt with it's surrounding, and thus internal controllers will feedback control signals within u. These control signals are known by the agent itself and might be shared with it's neighbours; however, it is most likely to be unknown for the rest of the agents. An example on the second condition above is where an agent is fully or partially controlled by a human driver. The human behaviour is unpredictable due to many reasons such as sudden change in decisions and different experience. Another example on the second condition above is the dynamics due to the parameter uncertainties in the modeled dynamics Ax. We push all such unknown dynamics to the unknown nonlinear function f. An example on the third condition above is where the system is driving on slippery grounds. This external disturbance will bias the friction coefficient with the road, and thus w will have a biased distribution. Define the noise-free outputs

$$y_{\mathrm{i},0}(k) = C_{\mathrm{i}}x(k), \tag{7.4}$$

$$y_{\mathrm{o},0}(k) = C_{\mathrm{o}}x(k). \tag{7.5}$$

In this work, we obtain a less noisy estimation of the output $y_{\mathrm{o},0}$ based on the output y_{i} only, and independent on the input signals u, unmodeled dynamics f, and the external disturbances w. It is evident from [63, 8] that if $y_{\mathrm{i},0}$ is available, then $y_{\mathrm{o},0}$ can be directly estimated. However, the measurements of $y_{\mathrm{i},0}$ is corrupted with the noise δ_{i}, and thus the estimation based on y_{i} will have a level noise. This approach proposes fusing the estimation based on y_{i} along with the measurements of y_{o} in the Kalman filter theme to obtain a less noisy estimation of the output y_{o}.

Assumption 1: All the measurements noise in δ_{i} and δ_{o} are assumed to have Gaussian distribution.

Assumption 2. All zeros in the output channel y_{i} are assumed to be inside the unity circle, and less than the number of zeros in any output channel in y_{o}.

Assumption 1 is is needed to compute the covariance matrices as will be explained after. Assumption 2 ensures that the relationship from y_{i} to y_{o} is always causal and stable. Assumption 2 is needed to emphasise the focus of this work. We leave the case of zeros outside the unity circle (unstable zeros) to a future work.

For clarification, the following section demonstrates the proposed approach on a simple system, and then the rest of the work generalizes the proposed approach on the class of

systems in (7.1)-(7.3). The example in the following section considers a linear stationary (no input) system $m_1 = 0$ with zero initial conditions and certain parameters, subjected to a scalar non-Gaussian process noise $m_2 = 1$, and the output of interest y_o being scalar $p = 1$.

7.2 Motivating Example

7.2.1 Transmissibility Operators

Given the simplified case with $m_1 = 0, m_2 = 1$, and $p = 1$, the system in (7.1)-(7.3) becomes a linear plant with single input w and two outputs y_i and y_o. Then the relationship between the process noise w and the noise-free outputs $y_{i,0}, y_{o,0}$ in the discrete frequency domain (z-domain) under zero initial conditions can be given as

$$\frac{Y_{i,0}(z)}{W(z)} = \frac{C_i \text{adj}(zI - A)B_w}{\det(zI - A)}, \tag{7.6}$$

$$\frac{Y_{o,0}(z)}{W(z)} = \frac{C_o \text{adj}(zI - A)B_w}{\det(zI - A)}, \tag{7.7}$$

where $Y_{i,0}, Y_{o,0}, W$ are $y_{i,0}, y_{o,0}, w$ in the frequency domain, respectively. Notice that since both outputs $Y_{i,0}, Y_{o,0}$ share the same input disturbances W, then both transfer functions (7.6)-(7.7) have the same denominator, which is the system's characteristics equation. Next, obtain the relationship from the output $Y_{i,0}$ to the output $Y_{o,0}$ by dividing (7.7) on (7.6)

$$\begin{aligned} \bar{\mathscr{T}}(z) = \frac{Y_{o,0}(z)}{Y_{i,0}(z)} &= \frac{C_o \text{adj}(zI - A)B_w}{C_i \text{adj}(zI - A)B_w} \\ &= \frac{a_{\rho-1}z^{\rho-1} + \cdots + a_1 z + a_0}{z^\rho + \cdots + b_1 z + b_0}. \end{aligned} \tag{7.8}$$

The operator $\bar{\mathscr{T}}(z)$ is called frequency-domain transmissibility. The main advantage of $\bar{\mathscr{T}}$ is the independency of non-Gaussian noise w. Please refer to [8] for more details about this independency. Notice that $\bar{\mathscr{T}}$ in the frequency-domain shapes like a transfer function, however, from one output to another. ρ is the number of zeros related to the output y_i, which is also the order of $\bar{\mathscr{T}}$. Assumption 2 guarantees that $\bar{\mathscr{T}}$ is causal and stable. Since the number of zeros associated with the output y_i are more than the number of zeros associated with the output y_o, then the denominator order of $\bar{\mathscr{T}}$ is higher than the numerator order, and thus $\bar{\mathscr{T}}$ is causal. Moreover, the stable zeros of the output y_i become stable poles of $\bar{\mathscr{T}}$, thus $\bar{\mathscr{T}}$ is also stable. By applying the forward shifting theorem on (7.8) such that $Y_{i,0}(k)z^{-j} = y_{i,0}(k-j)$ and similarly for $y_{o,0}$, $\bar{\mathscr{T}}$ can be interpreted in the discrete time state

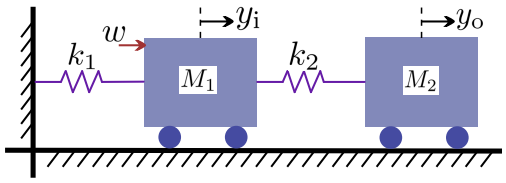

Fig. 7.1 Example 7.2.1: Two mass-spring systems connected in series. This example derives the transmissibility between the position of the first mass y_{i} to the second mass y_{o}.

space as

$$\bar{x}(k+1) = \bar{A}\bar{x}(k) + \bar{B}y_{\mathrm{i},0}(k), \tag{7.9}$$

$$y_{\mathrm{o},0}(k) = \bar{C}\bar{x}(k), \tag{7.10}$$

where $\bar{x}$ is the transmissibility state vector, which is also called the pseudo states. Moreover,

$$\bar{A} = \begin{bmatrix} -b_{\rho-1} & \dots & -b_1 & -b_0 \\ 1 & \dots & 0 & 0 \\ \vdots & \ddots & \vdots & \vdots \\ 0 & \dots & 1 & 0 \end{bmatrix} \in \mathbb{R}^{\rho\times\rho},$$

$$\bar{B} = \begin{bmatrix} 1 & 0 & \dots & 0 \end{bmatrix}^{\mathrm{T}} \in \mathbb{R}^{\rho},$$

$$\bar{C} = \begin{bmatrix} a_{\rho-1} & \dots & a_0 \end{bmatrix} \in \mathbb{R}^{1\times\rho}.$$

An estimation of $y_{\mathrm{o},0}$ can be directly obtained from (7.9)-(7.10) if $y_{\mathrm{i},0}$ is known. However, only the noisy output y_{i} is available. Replacing $y_{\mathrm{i},0}$ with y_{i} in the pseudo state equation (7.13) yields

$$\bar{x}(k+1) = \bar{A}\bar{x}(k) + \bar{B}\underbrace{\left[y_{\mathrm{i},0}(k) + \delta_{\mathrm{i}}(k)\right]}_{y_{\mathrm{i}}}. \tag{7.11}$$

Notice that the Gaussian measurement noise δ_{i} became process noise, and thus using (7.11) we can obtain an estimation of $y_{\mathrm{o},0}$ with Gaussian uncertainty distribution. Therefore, the estimation based on (7.11) along with the noisy measurements y_{o} can be used in the Kalman filter theme [62] to obtain a less noisy estimation of $y_{\mathrm{o},0}$.

Example 7.2.1 *In this example, we consider deriving the transmissibility operator between the displacements $y_{\mathrm{i},0}$ and $y_{\mathrm{o},0}$ of the system shown in Figure 7.1 that consists of two mass-spring systems connected in series with w being unknowns. Considering*

$k_1 = k_2 = M_1 = M_2 = 1$ *(springs and masses parameters), the system state space model follows* (7.1)-(7.3) *with the parameters*

$$A = \begin{bmatrix} 0 & 0 & 1 & 0 \\ 0 & 0 & 0 & 1 \\ -2 & 1 & 0 & 0 \\ 1 & -1 & 0 & 0 \end{bmatrix}, B_w = \begin{bmatrix} 0 \\ 0 \\ 1 \\ 0 \end{bmatrix},$$
$$C_{\mathrm{i}} = \begin{bmatrix} 1 & 0 & 0 & 0 \end{bmatrix}, C_{\mathrm{o}} = \begin{bmatrix} 0 & 1 & 0 & 0 \end{bmatrix}.$$

Then define

$$\bar{\mathscr{T}}(z) = \frac{Y_{\mathrm{o},0}(z)}{Y_{\mathrm{o,i}}(z)} = \frac{C_{\mathrm{o}}\mathrm{adj}(zI - A)B_w}{C_{\mathrm{i}}\mathrm{adj}(zI - A)B_w} = \frac{1}{z^2 + 1}. \tag{7.12}$$

Note that the transmissibility operator (7.12) *is independent of w. Moreover, only* (7.12) *and a measurement of* $y_{\mathrm{i},0}$ *are required to obtain an estimation of* $y_{\mathrm{o},0}$*. Transforming* $\mathscr{T}$ *in* (7.12) *to the state space form yields*

$$\bar{x}(k+1) = \begin{bmatrix} 0 & -1 \\ 1 & 0 \end{bmatrix} \bar{x}(k) + \begin{bmatrix} 1 \\ 0 \end{bmatrix} y_{\mathrm{i},0}(k), \tag{7.13}$$
$$y_{\mathrm{o},0}(k) = \begin{bmatrix} 0 & 1 \end{bmatrix} \bar{x}(k). \quad \square \tag{7.14}$$

A well known advantage of Kalman filter is that the estimation at time step k depends only on the estimation at time step $k-1$ and not earlier time steps. This property is known as recursive estimation. The recursive estimation works by alternating two phases, estimation and update.

7.2.2 Kalman Estimation

We first use the measurements of y_{i} to estimate $\bar{x}$ from

$$\hat{\bar{x}}(k+1|k) = \bar{A}\hat{\bar{x}}(k|k) + \bar{B}y_{\mathrm{i}}(k), \tag{7.15}$$

where $\hat{\bar{x}}(k+1|k)$ is the priori state estimation. Let $\mathbf{Q}$ be the covariance of the measurement noise δ_{i}, then the estimation covariance is computed from

$$\mathbf{P}(k+1|k) = \bar{A}\mathbf{P}(k|k)\bar{A}^{\mathrm{T}} + \mathbf{Q}, \tag{7.16}$$

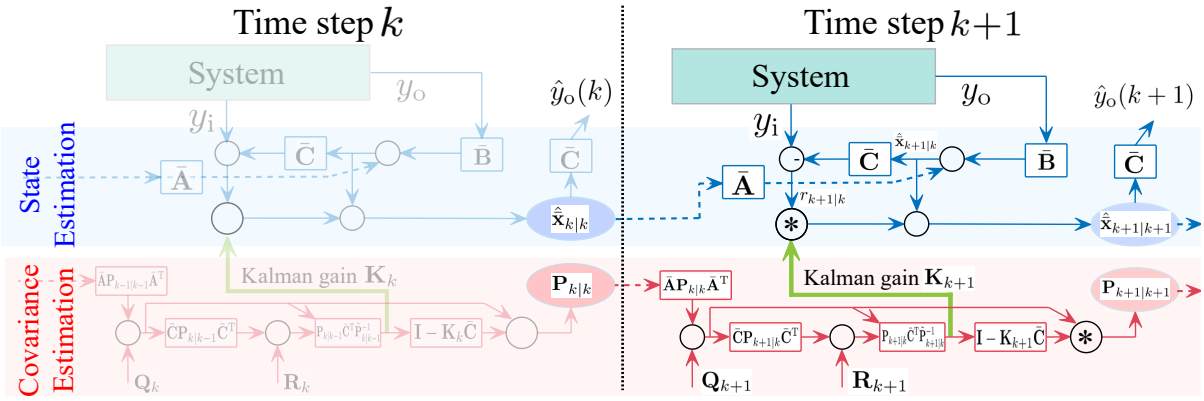

Fig. 7.2 Block diagram of the proposed approach that summarizes the transition of the platoon states and covariance from time step k to $k+1$.

where $\mathbf{P}$ is the estimate covariance matrix. The initial value of $\mathbf{P}$ can be set to the identity matrix.

7.2.3 Kalman Update

The update phase is represented in incorporating the Kalman estimation in (7.15)-(7.16) with the measurements of y_o. Define the measurements innovation (measurements priori residual)

$$\tilde{y}_o(k+1|k) = y_o(k+1) - \bar{C}\hat{\bar{x}}(k+1|k), \tag{7.17}$$

Next, define the covariance innovation (covariance priori residual)

$$\tilde{\mathbf{P}}(k+1|k) = \bar{C}\mathbf{P}(k+1|k)\bar{C}^{\mathrm{T}} + \mathbf{R}, \tag{7.18}$$

where $\mathbf{R}$ is the covariance of δ_o. The optimal Kalman gain is then updated as

$$\mathbf{K}(k+1) = \mathbf{P}(k+1|k)\bar{C}^{\mathrm{T}}\tilde{\mathbf{P}}^{-1}(k+1|k). \tag{7.19}$$

The convergence analysis on the optimal Kalman gain is investigated in Section 7.4. We then update the priori estimation of $\bar{x}$ as

$$\hat{\bar{x}}(k+1|k+1) = \hat{\bar{x}}(k+1|k) + \mathbf{K}(k+1)\tilde{y}_o(k+1|k), \tag{7.20}$$

where $\hat{\bar{x}}(k+1|k+1)$ is the posteriori state estimation. Next, update the priori estimate covariance as

$$\mathbf{P}(k+1|k+1) = (I - \mathbf{K}(k+1)\bar{C})\mathbf{P}(k+1|k), \tag{7.21}$$

where $\mathbf{P}(k+1|k+1)$ is the posteriori estimate covariance that will be derived and further investigated in Section 7.4. The filtered output y_{o} is then given by

$$\hat{y}_{\mathrm{o}}(k) = \bar{C}\hat{\bar{x}}(k+1|k+1). \tag{7.22}$$

The final residual on y_{o} after the update is then given by

$$\tilde{y}_{\mathrm{o}}(k+1|k+1) = y_{\mathrm{o}}(k+1) - \hat{y}_{\mathrm{o}}(k+1), \tag{7.23}$$

where $\tilde{y}_{\mathrm{o}}(k|k)$ is the posteriori residual that we aim to minimize. The transmissibility-based Kalman filter is from time step k to time step $k+1$ is shown in Figure 7.2.

Although, intense research studies have been introduced in the literature to estimate the noise covariances $\mathbf{Q}$ and $\mathbf{R}$ as in [41, 124], the estimation of $\mathbf{Q}$ and $\mathbf{R}$ remains a challenge. To focus on the proposed approach, we consider constant noise covariances $\mathbf{Q}$ and $\mathbf{R}$ in this work. The adaptive noise covariances will be assumed for future work. Following [48], we define $\mathbf{Q}$ and $\mathbf{R}$ based on the noise standard deviation as

$$\mathbf{Q} = T_s T_s^{\mathrm{T}} \sigma_{\mathrm{i}}^2 \in \mathbb{R}^{\rho \times \rho}, \tag{7.24}$$

$$T_s = \begin{bmatrix} \frac{1}{\rho!}t_s^{\rho} & \dots & \frac{1}{2}t_s^2 & t_s \end{bmatrix}^{\mathrm{T}}, \tag{7.25}$$

where t_s is the sampling time and σ_{i} is the standard deviation of δ_{i}. The measurements covariance is set to $\mathbf{R} = \sigma_{\mathrm{o}}^2$, where σ_{o} is the standard deviation of δ_{o}.

The aforementioned motivating example considered a linear case with only with the non-Gaussian process noise w and the output of interest y_{o} being scalars.

7.3 General Statement

This section extends the technique introduced in 7.2 to the class of systems (7.1)-(7.3). In the general sense, the system will be subjected to multiple independent nonlinearities and multiple process noises. That is, f and w in (7.1) are vectors ($m_1 \geq 2, m_2 \geq 2$). Moreover, the user might require to filter multiple outputs at the same time. That is, y_{o} is also a vector ($p \geq 2$). Same procedure can be followed; however, the transmissibility operator $\mathscr{T}$ will

be a MIMO mathematical model. Furthermore, the initial conditions in 7.2 were zero. To extend to systems with nonzero initial conditions, transmissibilities will be constructed in the feedforward shifting operator domain $\mathbf{q}$ instead of the discrete complex domain z. The advantage of using $\mathbf{q}$ instead of the complex variable z is that $\mathbf{q}$ is time-domain. In case of zero initial conditions, $\mathbf{q}$ can be replaced with the complex variable z directly $\mathbf{q} = z$.

Let $\bar{m} = m_1 + m_2$ be the total number of signals in f and w that are unknown and we wish to construct transmissibilities independent on them. Then for $y_{\mathrm{i},0} \in \mathbb{R}^{\bar{m}}, y_{\mathrm{o},0} \in \mathbb{R}^{p}, \bar{m} \geq 2, p \geq 2$, the transmissibility operator from the pseudo input $y_{\mathrm{i},0}$ to the estimation of the output $y_{\mathrm{o},0}$ in the discrete forward shifting operator domain $\mathbf{q}$ satisfies [8]

$$y_{\mathrm{o},0}(k) = \mathscr{T}(\mathbf{q}) y_{\mathrm{i},0}(k), \tag{7.26}$$

where

$$\begin{aligned}
\mathscr{T}(\mathbf{q}) &\triangleq \Gamma_{\mathrm{o}}(\mathbf{q}) \Gamma_{\mathrm{i}}^{-1}(\mathbf{q}), \\
\Gamma_{\mathrm{i}}(\mathbf{q}) &\triangleq C_{\mathrm{i}} \mathrm{adj}(\mathbf{q}I - A) B, \\
\Gamma_{\mathrm{o}}(\mathbf{q}) &\triangleq C_{\mathrm{o}} \mathrm{adj}(\mathbf{q}I - A) B, \\
B &= \begin{bmatrix} B_f & B_w \end{bmatrix}.
\end{aligned}$$

Note that, the transmissibility operator $\mathscr{T}$ is linear and independent on the input signals u, unmodeled dynamics f, and the non-Gaussian disturbances w [8]. Assumption 2 guarantees that $\mathscr{T}$ is always causal and stable. Define the elements of $y_{\mathrm{i},0}, y_{\mathrm{o},0}$, and $\mathscr{T}$ such as

$$\begin{aligned}
\mathscr{T}(\mathbf{q}) &= \begin{bmatrix} \mathscr{T}_{1,1}(\mathbf{q}) & \dots & \mathscr{T}_{1,\bar{m}}(\mathbf{q}) \\ \vdots & \ddots & \vdots \\ \mathscr{T}_{p,1}(\mathbf{q}) & \dots & \mathscr{T}_{p,\bar{m}}(\mathbf{q}) \end{bmatrix}, \\
y_{\mathrm{i},0}(k) &= \begin{bmatrix} y_{\mathrm{i},0}^{(1)}(k) & \dots & y_{\mathrm{i},0}^{(\bar{m})}(k) \end{bmatrix}^{\mathrm{T}}, \\
y_{\mathrm{o},0}(k) &= \begin{bmatrix} y_{\mathrm{o},0}^{(1)}(k) & \dots & y_{\mathrm{o},0}^{(p)}(k) \end{bmatrix}^{\mathrm{T}},
\end{aligned}$$

where for all $\ell \in \{1,\dots,p\}$ and $j \in \{1,\dots,\bar{m}\}$, $\mathscr{T}_{\ell,j}$ is the (ℓ,j) entry of $\mathscr{T}$, $y_{\mathrm{i},0}^{(j)}$ and $y_{\mathrm{o},0}^{(\ell)}$ are the jth entry of $y_{\mathrm{i},0}$ and the ℓth entry of $y_{\mathrm{o},0}$, respectively. Thus (7.26) can be interpreted as

$$y_{\mathrm{o},0}^{(1)}(k) = \mathscr{T}_{1,1}(\mathbf{q})y_{\mathrm{i},0}^{(1)}(k) + \cdots + \mathscr{T}_{1,\bar{m}}(\mathbf{q})y_{\mathrm{i},0}^{(\bar{m})}(k), \tag{7.27}$$

$$\vdots$$

$$y_{\mathrm{o},0}^{(p)}(k) = \mathscr{T}_{p,1}(\mathbf{q})y_{\mathrm{i},0}^{(1)}(k) + \cdots + \mathscr{T}_{p,\bar{m}}(\mathbf{q})y_{\mathrm{i},0}^{(\bar{m})}(k). \tag{7.28}$$

Note that each entry of $\mathscr{T}$ has the form of a transfer function in the $\mathbf{q}$ domain. Define $\mathscr{T}_{\ell,j}$ for all $\ell \in \{1,\dots,p\}$ and $j \in \{1,\dots,\bar{m}\}$ as

$$\mathscr{T}_{\ell,j}(\mathbf{q}) = \frac{a_{\rho-1}^{(\ell,j)}\mathbf{q}^{\rho-1} + \cdots + a_1^{(\ell,j)}\mathbf{q} + a_0^{(\ell,j)}}{\mathbf{q}^{\rho} + \cdots + b_1^{(\ell,j)}\mathbf{q} + b_0^{(\ell,j)}}. \tag{7.29}$$

Note that ρ is the highest order among all operators in $\mathscr{T}$. Similar to (7.8), substitute the forward shifting operator (i.e. $y(k)\mathbf{q} = y(k+1)$), then $\mathscr{T}_{\ell,j}$ can be interpreted as

$$\bar{x}_{\ell,j}(k+1) = \bar{A}_{\ell,j}\bar{x}_{\ell,j}(k) + \bar{B}_{\ell,j}y_{\mathrm{i},0}^{(j)}(k), \tag{7.30}$$

$$y_{\mathrm{o},0}^{(\ell)}(k) = \sum_{j=1}^{\bar{m}} \bar{C}_{\ell,j}\bar{x}_{\ell,j}(k), \tag{7.31}$$

where $\bar{x}_{\ell,j}$ is the pseudo state vector corresponding to the transmissibility operator $\mathscr{T}_{\ell,j}$. Moreover,

$$\bar{A}_{\ell,j} = \begin{bmatrix} -b_{\rho-1}^{(\ell,j)} & \dots & -b_1^{(\ell,j)} & -b_0^{(\ell,j)} \\ 1 & \dots & 0 & 0 \\ \vdots & \ddots & \vdots & \vdots \\ 0 & \dots & 1 & 0 \end{bmatrix} \in \mathbb{R}^{\rho\times\rho},$$

$$\bar{B}_{\ell,j} = \begin{bmatrix} 1 & 0 & \dots & 0 \end{bmatrix}^{\mathrm{T}} \in \mathbb{R}^{\rho},$$

$$\bar{C}_{\ell,j} = \begin{bmatrix} a_{\rho-1}^{(\ell,j)} & \dots & a_0^{(\ell,j)} \end{bmatrix} \in \mathbb{R}^{1\times\rho}.$$

By combining the transmissibility operators in (7.30)-(7.31) for all $\ell \in \{1,\dots,p\}$ and $j \in \{1,\dots,\bar{m}\}$, the overall transmissibility model $\mathscr{T}$ can be interpreted in the state space from in

(7.9)-(7.10) with order $\bar{\rho} = p\bar{m}\rho$, $y_{\mathrm{i},0} \in \mathbb{R}^{\bar{m}}$ and $y_{\mathrm{o},0} \in \mathbb{R}^{p}$ where

$$\bar{x}(k) = \begin{bmatrix} \bar{x}_1(k) & \dots & \bar{x}_p(k) \end{bmatrix}^{\mathrm{T}} \in \mathbb{R}^{\bar{\rho}}, \tag{7.32}$$

$$\bar{A} = \mathrm{diag}(\bar{A}_1, \dots, \bar{A}_p) \in \mathbb{R}^{\bar{\rho} \times \bar{\rho}}, \tag{7.33}$$

$$\bar{B} = \begin{bmatrix} \bar{B}_1 & \dots & \bar{B}_p \end{bmatrix}^{\mathrm{T}} \in \mathbb{R}^{\bar{\rho} \times \bar{m}}, \tag{7.34}$$

$$\bar{C} = \mathrm{diag}(\bar{C}_1, \dots, \bar{C}_p) \in \mathbb{R}^{p \times \bar{\rho}}, \tag{7.35}$$

where for all $\ell \in \{1, \dots, p\}$

$$\bar{x}_\ell(k) = \begin{bmatrix} \bar{x}_{\ell,1}(k) & \dots & \bar{x}_{\ell,\bar{m}}(k) \end{bmatrix}^{\mathrm{T}} \in \mathbb{R}^{\bar{m}\rho},$$
$$\bar{A}_\ell = \mathrm{diag}(\bar{A}_{\ell,1}, \dots, \bar{A}_{\ell,\bar{m}}) \in \mathbb{R}^{\bar{m}\rho \times \bar{m}\rho},$$
$$\bar{B}_\ell = \mathrm{diag}(\bar{B}_{(\ell,1)}, \dots, \bar{B}_{(\ell,\bar{m})}) \in \mathbb{R}^{\bar{m}\rho \times \bar{m}},$$
$$\bar{C}_\ell = \begin{bmatrix} \bar{C}_{(\ell,1)} & \dots & \bar{C}_{(\ell,\bar{m})} \end{bmatrix} \in \mathbb{R}^{1 \times \bar{m}\rho}.$$

After interpreting $\mathscr{T}$ into (7.9)-(7.10) the transmissibility-based Kalman filter introduced in equations (7.11)-(7.23) can be directly applied for the case where f, w, and y_{o} are vectors. The parameter matrices in (7.9)-(7.10) has to follow the definitions in (7.32)-(7.35) for the general case. Notice that replacing $y_{\mathrm{i},0}$ with the measured output subset y_{i} renders δ_{i} process noise for the general case as well.

Regarding the estimation of the noise covariance matrices, define the measurements noise in (7.2)-(7.3) as

$$\delta_{\mathrm{i}}(k) = \begin{bmatrix} \delta_{\mathrm{i},1}(k) & \dots & \delta_{\mathrm{i},\bar{m}}(k) \end{bmatrix}^{\mathrm{T}},$$
$$\delta_{\mathrm{o}}(k) = \begin{bmatrix} \delta_{\mathrm{o},1}(k) & \dots & \delta_{\mathrm{o},p}(k) \end{bmatrix}^{\mathrm{T}}.$$

For all $j \in \{1, \dots, \bar{m}\}$ let $\sigma_{\mathrm{i},j}$ be the standard deviation of the noise signal $\delta_{\mathrm{i},j}$, and similarly for all $\ell \in \{1, \dots, p\}$ let $\sigma_{\mathrm{o},\ell}$ be the standard deviation of the noise signal $\delta_{\mathrm{o},\ell}$. Then the process noise covariance can be defined as

$$\mathbf{Q} = \mathrm{diag}(\mathbf{Q}_1, \dots, \mathbf{Q}_p) \in \mathbb{R}^{\bar{\rho} \times \bar{\rho}}, \tag{7.36}$$

$$\mathbf{R} = \mathrm{diag}(\sigma_{\mathrm{o},1}^2, \dots, \sigma_{\mathrm{o},p}^2) \in \mathbb{R}^{p \times p}, \tag{7.37}$$

where for all $\ell \in \{1,\ldots,p\}$

$$\begin{aligned}\mathbf{Q}_\ell &= \text{diag}(\mathbf{Q}_{\ell,1},\ldots,\mathbf{Q}_{\ell,\bar{m}}) \in \mathbb{R}^{\bar{m}\rho\times\bar{m}\rho},\\ \mathbf{Q}_{\ell,j} &= T_s T_s^{\mathrm{T}} \sigma_{\mathrm{i},j}^2,\end{aligned}$$

and T_s is as defined in (7.25). Notice that $\mathbf{Q}$ depends on the standard deviation of the noise δ_{i} only, and thus $\mathbf{Q}_\ell$ is identical for all $\ell \in \{1,\ldots,p\}$ (same $\mathbf{Q}_\ell$ for each output in y_{o}).

7.4 Convergence Analysis and Optimal Kalman Gain

Define the estimation error of $\bar{x}$ as

$$\tilde{x}(k) = \bar{x}(k) - \hat{\bar{x}}(k|k). \tag{7.38}$$

The following Theorem investigates minimizing the mean-square error of the estimated states $\hat{\bar{x}}$.

Theorem 3. For the system (7.1)-(7.3) under Assumptions 1-2 and given the estimator designed in (7.15)-(7.23), the optimal Kalman gain in (7.19) minimizes the estimation mean-square error $||\tilde{x}||^2$.

Theorem 3 Proof. Define the updated estimate covariance

$$\mathbf{P}(k+1|k+1) = \text{cov}\left[\bar{x}(k+1) - \hat{\bar{x}}(k+1|k+1)\right]. \tag{7.39}$$

Kalman filter is a recursive algorithm such that the estimation at time step $k+1$ depends only on the time step k. Thus, we need to obtain $\mathbf{P}(k+1|k+1)$ as a function of $\mathbf{P}(k+1|k)$ and show that the estimation error is minimizing from k to $k+1$. Substitute (7.20) and then (7.17)

$$\begin{aligned}\mathbf{P}(k+1|k+1) = \text{cov}\big[\bar{x}(k+1) - \big[\hat{\bar{x}}(k+1|k)\\ + \mathbf{K}(k+1)(y_{\mathrm{o}}(k+1) - \bar{C}\hat{\bar{x}}(k+1|k))\big]\big].\end{aligned} \tag{7.40}$$

Note from (7.3) and (7.10)

$$\begin{aligned}y_{\mathrm{o}}(k) &= y_{\mathrm{o},0}(k) + \delta_{\mathrm{o}}(k)\\ &= \bar{C}\bar{x}(k) + \delta_{\mathrm{o}}(k).\end{aligned} \tag{7.41}$$

Substitute (7.41) in (7.40) at time step $k+1$ and collect terms yields

$$\begin{aligned}\mathbf{P}(k+1|k+1) = \operatorname{cov}\big[[I-\mathbf{K}(k+1)\bar{C}][\bar{x}(k+1) \\ -\hat{\bar{x}}(k+1|k)] - \mathbf{K}(k+1)\delta_{\mathrm{o}}(k+1)\big].\end{aligned} \tag{7.42}$$

Since δ_{o} is independent noise

$$\begin{aligned}\mathbf{P}(k+1|k+1) = \operatorname{cov}\big[[I-\mathbf{K}(k+1)\bar{C}][\bar{x}(k+1) \\ -\hat{\bar{x}}(k+1|k)]\big] - \operatorname{cov}\big[\mathbf{K}(k+1)\delta_{\mathrm{o}}(k+1)\big].\end{aligned} \tag{7.43}$$

Applying the vector covariance property [88] on the certain terms yields

$$\begin{aligned}\mathbf{P}(k+1|k+1) = \big(I-\mathbf{K}(k+1)\bar{C}\big)\operatorname{cov}\big[\bar{x}(k+1) \\ -\hat{\bar{x}}(k+1|k)\big]\big(I-\mathbf{K}(k+1)\bar{C}\big)^{\mathrm{T}} \\ -\mathbf{K}(k+1)\operatorname{cov}\big[\delta_{\mathrm{o}}(k+1)\big]\mathbf{K}^{\mathrm{T}}(k+1).\end{aligned} \tag{7.44}$$

Note that

$$\begin{aligned}\mathbf{P}(k+1|k) = \operatorname{cov}\left[\bar{x}(k+1)-\hat{\bar{x}}(k+1|k)\right], \\ \mathbf{R} = \operatorname{cov}\big[\delta_{\mathrm{o}}(k+1)\big].\end{aligned}$$

Then (7.44) becomes

$$\begin{aligned}\mathbf{P}(k+1|k+1) = \big(I-\mathbf{K}(k+1)\bar{C}\big)\mathbf{P}(k+1|k) \\ \big(I-\mathbf{K}(k+1)\bar{C}\big)^{\mathrm{T}} - \mathbf{K}(k+1)\mathbf{R}\mathbf{K}^{\mathrm{T}}(k+1),\end{aligned} \tag{7.45}$$

which can be interpreted as

$$\begin{aligned}\mathbf{P}(k+1|k+1) = \mathbf{P}(k+1|k) - \mathbf{K}(k+1)\bar{C}\mathbf{P}(k+1|k) \\ -\mathbf{P}(k+1|k)\bar{C}^{\mathrm{T}}\mathbf{K}^{\mathrm{T}}(k+1) \\ +\mathbf{K}(k+1)\tilde{\mathbf{P}}(k+1|k)\mathbf{K}^{\mathrm{T}}(k+1).\end{aligned} \tag{7.46}$$

The aim here is to minimize $\tilde{x}$, which is equivalent to minimizing the trace of $\mathbf{P}$. Therefore

$$\begin{aligned}\frac{\partial \operatorname{tr}(\mathbf{P}_{k+1|k+1})}{\partial \mathbf{K}(k+1)} = -2\left[\bar{C}\mathbf{P}(k+1|k)\right]^{\mathrm{T}} \\ +2\mathbf{K}(k+1)\tilde{\mathbf{P}}(k+1|k).\end{aligned} \tag{7.47}$$

Setting (7.47) to zero yields

$$\mathbf{K}(k+1) = \mathbf{P}(k+1|k)\bar{C}^{\mathrm{T}}\tilde{\mathbf{P}}^{-1}(k+1|k). \quad \square \tag{7.48}$$

7.5 Numerical Example

To test the proposed approach numerically, we adopt the Connected Autonomous Vehicle (CAV) platoon model in [63]. The state space model in (7.1)-(7.3) was constructed with two vehicles. Following [63], the model parameters are set as

$$A = \begin{bmatrix} A_1 & 0 \\ N & A_1 \end{bmatrix}, N = \begin{bmatrix} C_1 \\ 0 \\ 0 \end{bmatrix},$$
$$B = \begin{bmatrix} 1 & 0 & \dots & 0 \end{bmatrix}^{\mathrm{T}},$$
$$C_{\mathrm{i}} = \begin{bmatrix} C_1 & 0 & \dots & 0 \end{bmatrix}, \; C_{\mathrm{o}} = \begin{bmatrix} 0 & \dots & 0 & C_1 \end{bmatrix},$$

such that y_{i} is set to the velocity of the first vehicle, and y_{o} is set to the velocity of the second vehicle. Moreover,

$$A_1 = \begin{bmatrix} 1.8 & -0.85 & 0.0007 \\ 1 & 0 & 0 \\ 0 & 1 & 0 \end{bmatrix}, \tag{7.49}$$

$$C_1 = \begin{bmatrix} 0.034 & -0.023 & -0.0048 \end{bmatrix}. \tag{7.50}$$

We ran the platoon for 200 seconds. The process noise w was set to the non-Gaussian noise signal shown in Figure 7.3, and the velocity measurements noises $\delta\mathrm{i}, \delta\mathrm{o}$ are set to the first and second Gaussian noise signals in Figure 7.3, respectively. The standard deviation of the noise signals was computed using

$$\sigma = \sqrt{\frac{\sum_{k=0}^{\bar{k}}(\alpha_k - \mu)^2}{\bar{k}}}, \tag{7.51}$$

where $\bar{k}$ is the total number of time samples, α_k is the noise value at time step k, and μ is the noise mean. The standard deviation was computed for the process noise $\sigma_w = 4.16$, first velocity's noise $\sigma_v = 1.38$, and second velocity's noise $\sigma_y = 1.4$. Next, the probability

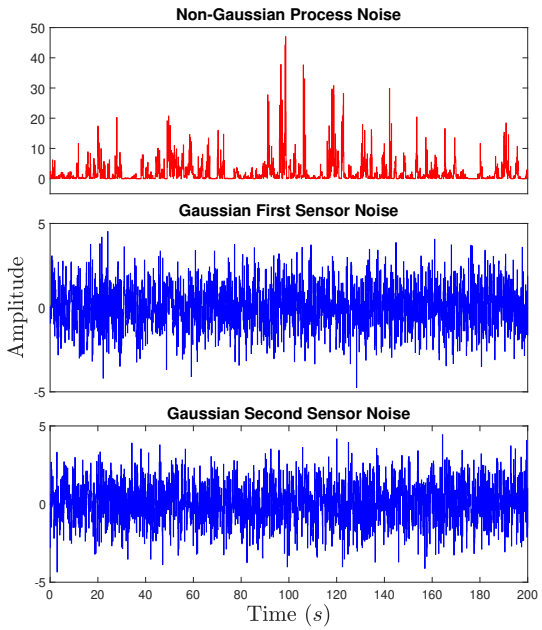

Fig. 7.3 Numerical Results: Non-Gaussian process and Gaussian measurements noise signals that are used to test the proposed approach numerically.

distribution was computed using

$$\delta(\alpha_k, \mu, \sigma) = \frac{1}{\sigma\sqrt{2\pi}} \exp\left[-\frac{1}{2}\left(\frac{\alpha_k - \mu}{\sigma}\right)\right]. \tag{7.52}$$

The probability distribution for the three noise signals are plotted in Figure 7.4. It can be noticed that w has a non-Gaussian distribution, while $y_{\mathrm{i}}, y_{\mathrm{o}}$ have Gaussian distribution. Next, the transmissibility operator T in Equation (7.8) was constructed using the simulation parameters. The computed transmissibility parameters are $b_0 = 0.0001, b_1 = -0.117, b_2 = -0.32, b_3 = 1.962, b_4 = -2.52, a_0 = 0.0007, a_1 = 0.0065, a_2 = 0.0063, a_3 = -0.047, a_4 = 0.034$.

Next, the transmissibility-based algorithm in equations (7.15)-(7.23) was then implemented on the simulation model. Figure 7.5 compares the filtered and unfiltered velocities of the second vehicle with the true noise-free velocity. The initial condition of the velocity was set to $7m/s$, and the estimation started with zero initial condition. Notice that the proposed approach was able to estimate the true velocity and filter most of the noise, while the platoon is subjected to the non-Gaussian process noise in Figure 7.3. Both velocity and position errors before and after the filtering are plotted in Figure 7.6. Notice that the position error grows with time since integrating the velocity noise accumulates it with time. Given the proposed

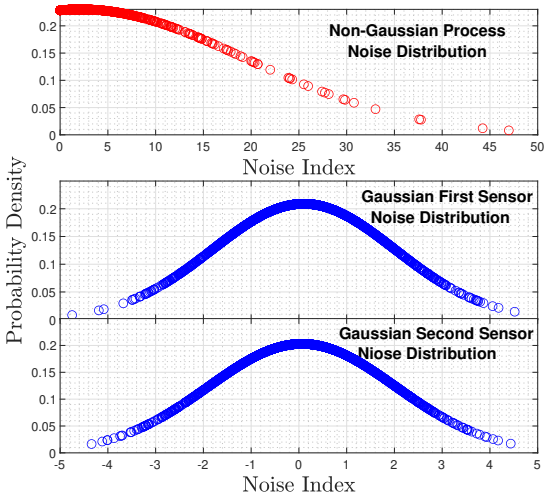

Fig. 7.4 Numerical Results: Probability distribution of the noise signals plotted in Figure 7.3.

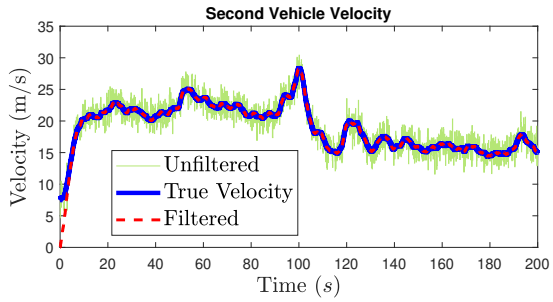

Fig. 7.5 Numerical Results: Filtered and unfiltered velocities comparison of the second vehicle with the true noise-free velocity.

approach, the second vehicle was localized very precisely while it drove in a non-Gaussian environment.

7.6 Experimental Test

7.6.1 Experimental Setup

The proposed approach was tested on the experimental setup shown in Figure 7.7, which consists of three Quanser autonomous differential robots called Qbots 2e. Each Qbot consists of two coaxial wheels, where each wheel is driven by a DC motor that is controlled using a closed-loop inverse kinematic controller. The robots are connected with V2V communication links to emulate CAV platoons. The robots follow the red line path, then both wheels' velocities are equal, and the Qbot moves forward or backward in a straight line. Qbot1 receives the excitation signal from a computer through wireless communication, and Qbot2

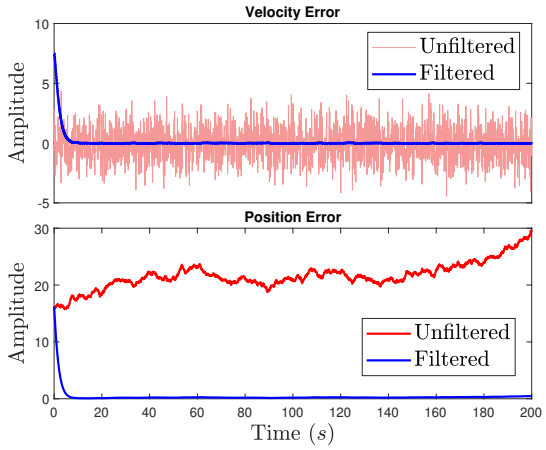

Fig. 7.6 Numerical Results: Velocity and position errors before and after the filtering. Notice that the proposed approach is able to precisely localize the second vehicle while the platoon is in a non-Gaussian environment.

follows the velocity of the first robot v_1. Similarly, Qbot3 is connected with Qbot2 via a V2V communication channel and follows the velocity of the second robot v_2. This experiment aims to localize the third robot within the 1D path using the noisy velocity measurements of the first robot, while the robots are under the effect of non-Gaussian process noise. In each robot, each wheel is supplied with an encoder, and the measured robot velocity is the average of the two encoder measurements. The measured position is computed by integrating the robot's velocity. As a reference, we measure the actual displacement of the third robot through a Polytech IVS-500 laser micro-vibrometer that has a microscale accuracy.

7.6.2 Noise Filtering

The transmissibility operator was constructed from $v_1(k)$ to $v_3(k)$, that is, we set $y_{\mathrm{i}} = v_1(k)$ and $y_{\mathrm{o}} = v_3(k)$. The robot's mathematical model was provided by Quanser (the manufacturer). The transmissibility operator in (7.8) was constructed based on the mathematical model with the parameters $b_0 = 1076, b_1 = 54.4, a_0 = 1053, a_1 = 53.31$. We ran the setup for 20 seconds by setting the desired velocity of the first robot to the noise signal in Figure 7.8. The probability distribution of the process noise plotted in Figure 7.8 was computed using the formula (7.52). The standard deviation of $y_{\mathrm{i}}, y_{\mathrm{o}}$ was estimated to be $\sigma_v = 1.39$ and $\sigma_y = 1.43$, and then $\mathbf{Q}, \mathbf{R}$ were computed as in Section 7.5.

Next, the transmissibility-based algorithm in equations (7.15)-(7.23) was then implemented on the experimental setup model. The encoder velocity measurements were recorded before and after filtering, and are plotted along with the vibrometer measurements (true

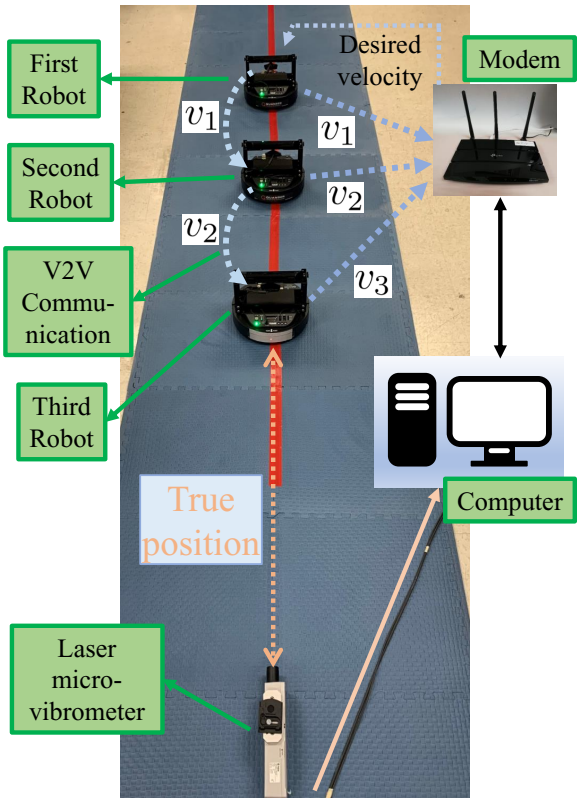

Fig. 7.7 The experimental setup consists of three connected autonomous robots. A laser micro-vibrometer is mounted to measure the true position of the third robot.

velocity) in Figure 7.9. The initial condition of the third robot's velocity was set to $0.53 m/s$, and the estimation started with zero initial condition. Notice that the proposed approach was able to estimate the true velocity and filter most of the noise, while the robots are subjected to the non-Gaussian process noise in Figure 7.8. Both velocity and position errors before and after the filtering are plotted in Figure 7.10. Given the proposed approach, the third robot was localized very precisely while the setup is under the effect of non-Gaussian noise.

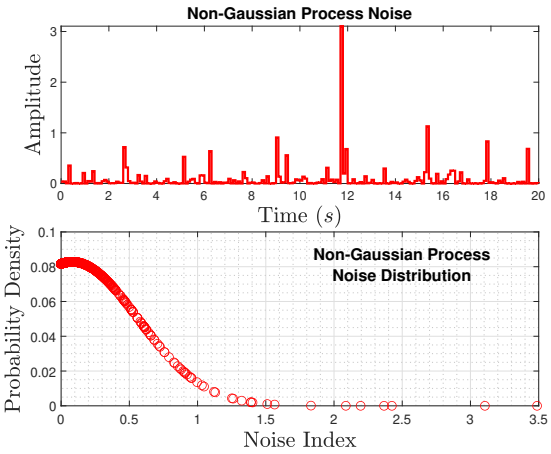

Fig. 7.8 Experimental Results: Non-Gaussian process noise that is used to derive the experimental setup in a non-Gaussian environment with its probability distribution.

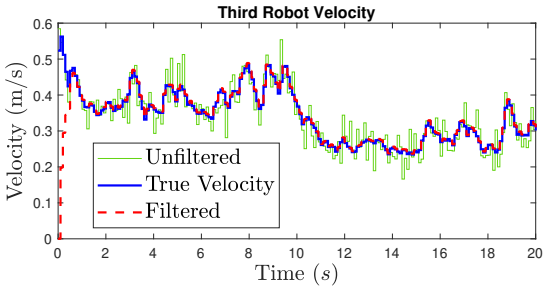

Fig. 7.9 Experimental Results: Filtered and unfiltered velocities comparison of the third robot with the true velocity. The true velocity was measured using the laser micro-vibrometer.

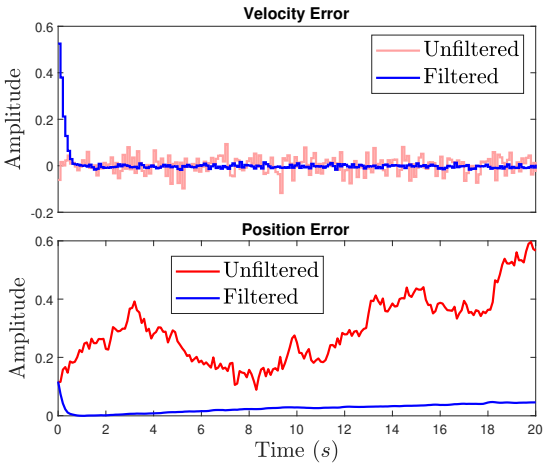

Fig. 7.10 Experimental Results: Velocity and position errors before and after the filtering. Notice that the proposed approach was able to localize the third robot while the platoon is in a non-Gaussian environment.

Chapter 8

Conclusions

This dissertation extended the transmissibility literature and deployed it for fault detection, fault-tolerant control, state estimation, and noise filtering. Transmissibility operators are mathematical objects that characterize the relationship between two subsets of responses of an underlying system. Transmissibility operators were shown to be independent of the systems inputs, unknown nonlinearities, and robust against external disturbances. Transmissibility operators were developed in this dissertation for the first time in the literature for nonlinear systems. Transmissibility operators were incorporated with sliding mode control to mitigate fault effects. Transmissibilities were extended to nonlinear time-variant systems, and recursive least squares identification was used to solve it. Moreover, a new state estimator was designed in a high-gain theme to robustly estimate the system states in a high-gain form.

Transmissibility-based estimation was incorporated in this work with three theoretical applications. For fault detection, transmissibility operators were used along a set of outputs to estimate the measurements of another set of outputs. Then faults were detected by comparing the estimated and measured outputs with each other. Control approaches used transmissibility-based estimation to construct the control signal that was injected back into the original system. Furthermore, transmissibility-based estimation was used to localize robots under non-Gaussian process noise.

These three theoretical applications (fault detection and localization, CAV control, and CAV localization) were applied to four different systems. The first system was Connected Autonomous Vehicles (CAV) platoons. Transmissibilities were used along with the measurements from sensors available in CAV platoons to identify transmissibility operators. Next, this was developed to mixed autonomous and human-driven vehicle platoons. Failure in a physical component of a vehicle, or failure in the form of an internal delay, a cyber-attack, or a communication time-delay affects the safety and security of the CAV platoons. This was also motivated by the fact that on-road human-drivers' behaviour is unknown and difficult

to be predicted. Therefore, the transmissibility superiority was exploited to gain robustness against the unknown human-driver behavior. The platoon faults were mitigated after using a transmissibility-based sliding mode controller. The controller stability and the string stability were investigated while the controller is active and the faults are mitigated. Moreover, transmissibilities were integrated with Kalman filter to localize CAV platoons while operating under non-Gaussian environment as unknown nonlinearities. The three applications were tested experimentally on a setup of three connected autonomous mobile robots.

The second system was a multi-actuator micro positioning system used in the semiconductors industry. Transmissibility operators were applied to this system for fault detection and fault-tolerant control. Fault detection was represented in applying the proposed developments to actuator fault detection. Some of the most common actuator faults, such as actuator loss of effectiveness and fatigue crack in the connection hinges were considered. Transmissibilities were used for fault detection without knowledge of the dynamics of the system or the excitation that acts on the system. Next, a transmissibility-based sliding mode control was implemented to mitigate common actuator faults in multi-actuator systems. This approach was tested numerically using an analytical simulation model and experimentally using a setup constructed with several electromechanical actuators.

The third system was flexible structures subjected to unknown and random excitations. Structures used in applications subjected to turbulent fluid flow, such as aerospace and underwater applications, are subjected to random excitations distributed along the structure. Transmissibility operators were used for the purpose of structural fault detection and localization during the system operation.

The fourth system was robotic manipulators with bounded nonlinearities and time-variant parameters. Both parameter variation and system nonlinearities are considered to be unknown. Transmissibility operators were integrated with Recursive Least Squares (RLS) to overcome the unknown variant parameters. RLS identifies transmissibilities used in the structure of noncausal FIR (Finite Impulse Response) models. While parameter variation can be treated as system nonlinearities, the RLS algorithm was used to optimize what time-variant dynamics to include in the transmissibility operator and what dynamics to push to the system nonlinearities over time. The identified transmissibilities were then used for the purpose of fault detection in an experimental robotic arm with variant-picked mass. The experimental results showed the proposed approach to be used effectively to detect faults in robotic manipulators.

Future work is represented in three directions: (i) Extending the current work to mixed platoons with longitudinal and lateral motion, (ii) Extended and detailed stability analysis of the transmissibility-based sliding mode controller, and (iii) Developing a state feedback controller that exhibits the robustness of the high-gain transmissibility state estimation.

References

[1] Adams, R., Cawley, P., Pye, C., Stone, B., 1978. A vibration technique for non-destructively assessing the integrity of structures. Journal of mechanical engineering science 20, 93–100.

[2] Alahi, M.E.E., Xie, L., Mukhopadhyay, S., Burkitt, L., 2017. A temperature compensated smart nitrate-sensor for agricultural industry. IEEE Transactions on industrial electronics 64, 7333–7341.

[3] Aljanaideh, K., Coffer, B.J., Bernstein, D.S., 2013. Closed-loop identification of unstable systems using noncausal FIR models, in: Proc. Amer. Contr. Conf., Washington, DC. pp. 1669–1674.

[4] Aljanaideh, K.F., Bernstein, D.S., 2015. Time-domain analysis of motion transmissibilities in force-driven and displacement-driven structures. Journal of Sound and Vibration 347, 169–183.

[5] Aljanaideh, K.F., Bernstein, D.S., 2016. Experimental application of transmissibility operators to fault detection, in: American Control Conference, pp. 6833–6838.

[6] Aljanaideh, K.F., Bernstein, D.S., 2017. Closed-loop identification of unstable systems using noncausal FIR models. International Journal of Control 90, 168–185.

[7] Aljanaideh, K.F., Bernstein, D.S., 2020. Output-only identification of input–output models. Automatica 113, 108686.

[8] Aljanaideh, K.F., Bernstein, D.S., Mar. 2015. Time-domain analysis of sensor-to-sensor transmissibility operators. Automatica 53, 312–319.

[9] Amoozgar, M.H., Chamseddine, A., Zhang, Y., 2013. Experimental test of a two-stage kalman filter for actuator fault detection and diagnosis of an unmanned quadrotor helicopter. Journal of Intelligent & Robotic Systems 70, 107–117.

[10] Anwar, S., Chen, L., 2007. An analytical redundancy-based fault detection and isolation algorithm for a road-wheel control subsystem in a steer-by-wire system. IEEE Transactions on Vehicular Technology 56, 2859–2869.

[11] Atoui, M.A., Verron, S., Kobi, A., 2015. Fault detection and diagnosis in a bayesian network classifier incorporating probabilistic boundary1. IFAC-PapersOnLine 48, 670–675.

[12] Avci, O., Abdeljaber, O., Kiranyaz, S., Hussein, M., Gabbouj, M., Inman, D.J., 2021. A review of vibration-based damage detection in civil structures: From traditional methods to machine learning and deep learning applications. Mechanical systems and signal processing 147, 107077.

[13] Avram, R.C., Zhang, X., Muse, J., 2017. Quadrotor actuator fault diagnosis and accommodation using nonlinear adaptive estimators. IEEE Transactions on Control Systems Technology 25, 2219–2226.

[14] Balaban, E., Saxena, A., Bansal, P., Goebel, K.F., Curran, S., 2009. Modeling, detection, and disambiguation of sensor faults for aerospace applications. IEEE Sensors Journal 9, 1907–1917.

[15] Bao, R., Wang, T., Wang, Q., . A multi-pump multi-actuator hydraulic system with on-off valve matrix for energy saving, in: IEEE/ASME International Conference on Advanced Intelligent Mechatronics (AIM), pp. 1110–1115, 2019.

[16] Bechtsis, D., Tsolakis, N., Vlachos, D., Srai, J.S., 2018. Intelligent autonomous vehicles in digital supply chains: a framework for integrating innovations towards sustainable value networks. Journal of cleaner production 181, 60–71.

[17] Bhavsar, P., Das, P., Paugh, M., Dey, K., Chowdhury, M., 2017. Risk analysis of autonomous vehicles in mixed traffic streams. Transportation Research Record 2625, 51–61.

[18] Boada, B.L., Boada, M.J.L., Zhang, H., 2019. Sensor fusion based on a dual kalman filter for estimation of road irregularities and vehicle mass under static and dynamic conditions. IEEE/ASME Transactions on Mechatronics 24, 1075–1086.

[19] Bohmann, T., Schlamp, M., Ehrlich, I., 2018. Acoustic emission of material damages in glass fibre-reinforced plastics. Composites Part B: Engineering 155, 444–451.

[20] Bresch-Pietri, D., Krstic, M., 2010. Delay-adaptive predictor feedback for systems with unknown long actuator delay. IEEE Transactions on Automatic Control 55, 2106–2112.

[21] Caccavale, F., Walker, I.D., 1997. Observer-based fault detection for robot manipulators, in: Proceedings of International Conference on Robotics and Automation, IEEE. pp. 2881–2887.

[22] Cai, B., Huang, L., Xie, M., 2017. Bayesian networks in fault diagnosis. IEEE Transactions on industrial informatics 13, 2227–2240.

[23] Cen, Z., Noura, H., Susilo, T.B., Al Younes, Y., 2014. Robust fault diagnosis for quadrotor uavs using adaptive thau observer. Journal of Intelligent & Robotic Systems 73, 573–588.

[24] Chen, H., Wang, Z., Liang, J., Li, M., 2020. State estimation for stochastic time-varying boolean networks. IEEE Transactions on Automatic Control 65, 5480–5487.

[25] Cho, C.N., Hong, J.T., Kim, H.J., 2019. Neural network based adaptive actuator fault detection algorithm for robot manipulators. Journal of Intelligent & Robotic Systems 95, 137–147.

[26] Costa, M.A., Wullt, B., Norrlöf, M., Gunnarsson, S., 2019. Failure detection in robotic arms using statistical modeling, machine learning and hybrid gradient boosting. Measurement 146, 425–436.

[27] Darbha, S., Konduri, S., Pagilla, P.R., 2018. Benefits of V2V communication for autonomous and connected vehicles. IEEE Transactions on Intelligent Transportation Systems 20, 1954–1963.

[28] Daroogheh, N., Baniamerian, A., Meskin, N., Khorasani, K., 2015. A hybrid prognosis and health monitoring strategy by integrating particle filters and neural networks for gas turbine engines, in: 2015 IEEE Conference on Prognostics and Health Management (PHM), IEEE. pp. 1–8.

[29] Dávila, A., Moreno, J.A., Fridman, L., 2010. Variable gains super-twisting algorithm: A lyapunov based design, in: Proceedings of the 2010 American Control Conference, IEEE. pp. 968–973.

[30] Deepak, J., Raja, V.B., Srikanth, D., Surendran, H., Nickolas, M., 2021. Non-destructive testing (ndt) techniques for low carbon steel welded joints: A review and experimental study. Materials Today: Proceedings 44, 3732–3737.

[31] Demetriou, M.A., . Detection of communication attacks on spatially distributed systems with multiple interconnected actuator/sensor pairs, in: IEEE Conference on Decision and Control (CDC), pp. 2896–2901, 2018.

[32] Deng, Q., Söffker, D., . Classifying human behaviors: Improving training of conventional algorithms, in: IEEE Intelligent Transportation Systems Conference (ITSC), pp. 1060–1065, 2019.

[33] Devriendt, C., Guillaume, P., 2008. Identification of modal parameters from transmissibility measurements. Journal of Sound and Vibration 314, 343–356.

[34] Ding, S.X., Yang, Y., Zhang, Y., Li, L., 2014. Data-driven realizations of kernel and image representations and their application to fault detection and control system design. Automatica 50, 2615–2623.

[35] Ding, S.X., Yin, S., Peng, K., Hao, H., Shen, B., 2012. A novel scheme for key performance indicator prediction and diagnosis with application to an industrial hot strip mill. IEEE Transactions on Industrial Informatics 9, 2239–2247.

[36] Do, M., Koenig, D., Theilliol, D., . An integrated design for robust actuator fault accommodation based on $\mathscr{H}_\infty$ proportional-integral observer, in: IEEE Conference on Decision and Control (CDC), pp. 6346–6352, 2018.

[37] Doshvarpassand, S., Wu, C., Wang, X., 2019. An overview of corrosion defect characterization using active infrared thermography. Infrared physics & technology 96, 366–389.

[38] Esfandiari, A., Bakhtiari-Nejad, F., Rahai, A., Sanayei, M., 2009. Structural model updating using frequency response function and quasi-linear sensitivity equation. Journal of sound and vibration 326, 557–573.

[39] Eski, I., Erkaya, S., Savas, S., Yildirim, S., 2011. Fault detection on robot manipulators using artificial neural networks. Robotics and Computer-Integrated Manufacturing 27, 115–123.

[40] Evangelista, C., Puleston, P., Valenciaga, F., Fridman, L.M., 2012. Lyapunov-designed super-twisting sliding mode control for wind energy conversion optimization. IEEE Transactions on industrial electronics 60, 538–545.

[41] Feng, B., Fu, M., Ma, H., Xia, Y., Wang, B., 2014. Kalman filter with recursive covariance estimation—sequentially estimating process noise covariance. IEEE Transactions on Industrial Electronics 61, 6253–6263.

[42] Fernandes, P., Nunes, U., . Platooning of autonomous vehicles with intervehicle communications in sumo traffic simulator, in: International IEEE Conference on Intelligent Transportation Systems, pp. 1313–1318, 2010.

[43] Fernandes, P., Nunes, U., 2012. Platooning with IVC-enabled autonomous vehicles: Strategies to mitigate communication delays, improve safety and traffic flow. IEEE Transactions on Intelligent Transportation Systems 13, 91–106.

[44] Gangsar, P., Tiwari, R., 2020. Signal based condition monitoring techniques for fault detection and diagnosis of induction motors: A state-of-the-art review. Mechanical systems and signal processing 144, 106908.

[45] Gao, Z., Liu, X., Chen, M.Z., 2015. Unknown input observer-based robust fault estimation for systems corrupted by partially decoupled disturbances. IEEE Transactions on Industrial Electronics 63, 2537–2547.

[46] Garcia-Bracamonte, J.E., Ramirez-Cortes, J.M., de Jesus Rangel-Magdaleno, J., Gomez-Gil, P., Peregrina-Barreto, H., Alarcon-Aquino, V., 2019. An approach on MCSA-based fault detection using independent component analysis and neural networks. IEEE Transactions on Instrumentation and Measurement 68, 1353–1361.

[47] Ghiasia, A., Lia, X., Mab, J., Quc, X., 2019. A mixed traffic speed harmonization model with connected autonomous vehicles. Transportation Research Part C: Emerging Technologies 104, 210–233.

[48] Govaers, F., 2019. Introduction and Implementations of the Kalman Filter. BoD–Books on Demand.

[49] Guo, J., Chee, S.K., Yano, T., Higuchi, T., 2013. Micro-vibration stage using piezo actuators. Sensors and Actuators A: Physical 194, 119–127.

[50] Guo, Z., Tian, Y., Liu, C., Wang, F., Liu, X., Shirinzadeh, B., Zhang, D., 2015. Design and control methodology of a 3-DOF flexure-based mechanism for micro/nano-positioning. Robotics and Computer-Integrated Manufacturing 32, 93–105.

[51] Han, K., Chen, C., Chen, M., Wang, Z., 2021. Constrained active fault tolerant control based on active fault diagnosis and interpolation optimization. Entropy 23, 924.

[52] Han, W., Wang, Z., Shen, Y., 2018. Fault estimation for a quadrotor unmanned aerial vehicle by integrating the parity space approach with recursive least squares. Proceedings of the Institution of Mechanical Engineers, Part G: Journal of Aerospace Engineering 232, 783–796.

[53] Heo, S., Lee, J.H., 2018. Fault detection and classification using artificial neural networks. IFAC-PapersOnLine 51, 470–475.

[54] Hu, Y., Zhang, S., Yan, Y., Wang, L., Qian, X., Yang, L., 2017. A smart electrostatic sensor for online condition monitoring of power transmission belts. IEEE Transactions on Industrial Electronics 64, 7313–7322.

[55] Hult, R., Campos, G.R., Steinmetz, E., Hammarstrand, L., Falcone, P., Wymeersch, H., 2016. Coordination of cooperative autonomous vehicles: Toward safer and more efficient road transportation. IEEE Signal Processing Magazine 33, 74–84.

[56] Ibrahim, A., Ismail, F., Martin, H., 1987. Modelling of the dynamics of a continuous beam including nonlinear fatigue crack. International Journal of Analytical and Experimental Modal Analysis 2, 76–82.

[57] Isermann, R., 1984. Process fault detection based on modeling and estimation methods—a survey. automatica 20, 387–404.

[58] Jiang, Y., Yin, S., Dong, J., Kaynak, O., 2020a. A review on soft sensors for monitoring, control and optimization of industrial processes. IEEE Sensors Journal .

[59] Jiang, Y., Yin, S., Kaynak, O., 2018. Data-driven monitoring and safety control of industrial cyber-physical systems: Basics and beyond. IEEE Access 6, 47374–47384.

[60] Jiang, Y., Yin, S., Kaynak, O., 2020b. Optimized design of parity relation-based residual generator for fault detection: Data-driven approaches. IEEE Transactions on Industrial Informatics 17, 1449–1458.

[61] Jin, X., Haddad, W.M., Jiang, Z.P., Vamvoudakis, K.G., Miami Beach, FL, pp. 2810-2815, 2018. Adaptive control for mitigating sensor and actuator attacks in connected autonomous vehicle platoons, in: IEEE Conference on Decision and Control.

[62] Kalman, R.E., 1960. A new approach to linear filtering and prediction problems. Journal of Fluid Engineering 82, 35–45.

[63] Khalil, A., Al Janaideh, M., Aljanaideh, K., Kundur, D., 2022a. Transmissibility-based health monitoring of the future connected autonomous vehicles networks. IEEE Transactions on Vehicular Technology .

[64] Khalil, A., Al Janaideh, M., Aljanaideh, K.F., Kundur, D., Las Vegas, NV, 2020. Output-only fault detection and mitigation of networks of autonomous vehicles, in: IEEE/RSJ International Conference on Intelligent Robots and Systems (IROS), pp. 2257–2264.

[65] Khalil, A., Aljanaideh, K.F., 2018. Aircraft structural health monitoring using transmissibility identification. IFAC-PapersOnLine 51, 969–974.

[66] Khalil, A., Aljanaideh, K.F., Al Janaideh, M., 2022b. Sensor measurements only with transmissibility operators for fault detection in flexible beams. IEEE Sensors Journal 22, 17977–17987.

[67] Khalil, A., Aljanaideh, K.F., Rideout, G., Al Janaideh, M., Denver, CO, Jul. 2020. Fault detection in flexible beams based on output only measurements, in: American Control Conference (ACC), pp. 5034–5039.

[68] Khalil, A., Pumphrey, M., Aljanaideh, K.F., Al Janaideh, M., 2021. Health monitoring of actuators of motion systems using output-only measurements, in: American Control Conference (ACC), IEEE. pp. 1595–1600.

[69] Khalil, H.K., 2017. High-gain observers in nonlinear feedback control. SIAM.

[70] Khalil, H.K., Praly, L., 2014. High-gain observers in nonlinear feedback control. International Journal of Robust and Nonlinear Control 24, 993–1015.

[71] Kim, J.T., Ryu, Y.S., Cho, H.M., Stubbs, N., 2003. Damage identification in beam-type structures: frequency-based method vs mode-shape-based method. Engineering structures 25, 57–67.

[72] Kordestani, M., Samadi, M.F., Saif, M., Khorasani, K., 2018. A new fault diagnosis of multifunctional spoiler system using integrated artificial neural network and discrete wavelet transform methods. IEEE Sensors Journal 18, 4990–5001.

[73] Law, S., Li, J., Ding, Y., 2011. Structural response reconstruction with transmissibility concept in frequency domain. Mech. Sys. Sig. Proc. 25, 952–968.

[74] Li, B., Rui, X., Tian, W., Cui, G., 2019a. Neural-network-predictor-based control for an uncertain multiple launch rocket system with actuator delay. Mechanical Systems and Signal Processing 141, 1–19.

[75] Li, D., Yang, P., Liu, Z., Wang, Z., Zhang, Z., 2021a. Fault-tolerant aircraft control based on self-constructing fuzzy neural network for quadcopter. International Journal of Automation Technology 15, 109–122.

[76] Li, F., Mikulski, D., Wagner, J., Wang, Y., 2019b. Trust-based control and scheduling for UGV platoon under cyber attacks. SAE Technical Paper .

[77] Li, H., Liu, H., Gao, H., Shi, P., 2011. Reliable fuzzy control for active suspension systems with actuator delay and fault. IEEE Transactions on Fuzzy Systems 20, 342–357.

[78] Li, J., Hao, H., Xia, Y., Zhu, H.p., 2014. Damage detection of shear connectors in bridge structures with transmissibility in frequency domain. International Journal of Structural Stability and Dynamics 14, 1350061.

[79] Li, Q., Liao, M., Jing, X., 2021b. Transmissibility function-based fault diagnosis methods for beam-like engineering structures: a review of theory and properties. Nonlinear Dynamics 106, 2131–2163.

[80] Li, S., Chen, Y., Zhan, J., 2021c. Simultaneous observer-based fault detection and event-triggered consensus control for multi-agent systems. Journal of the Franklin Institute 358, 3276–3301.

[81] Lim, P., Goh, C.K., Tan, K.C., Dutta, P., 2015. Multimodal degradation prognostics based on switching kalman filter ensemble. IEEE transactions on neural networks and learning systems 28, 136–148.

[82] Lin, F., Wang, A., Zhuang, Y., Tomita, M.R., Xu, W., 2016. Smart insole: A wearable sensor device for unobtrusive gait monitoring in daily life. IEEE Transactions on Industrial Informatics 12, 2281–2291.

[83] Liu, X., Kumar, P., . Towards safety of transportation systems with a mixture of automated and human-driven vehicles, in: International Conference on Communication Systems and Networks (COMSNETS), pp. 1–3, 2016.

[84] Lopes, A., Araújo, R.E., 2020. Active fault diagnosis method for vehicles in platoon formation. IEEE Transactions on Vehicular Technology 69, 3590–3603.

[85] Maia, N.M., Silva, J.M., Ribeiro, A.M., 2001. The transmissibility concept in multi-degree-of-freedom systems. Mechanical Systems and Signal Processing 15, 129–137.

[86] Mao, J., Sun, Y., Yi, X., Liu, H., Ding, D., 2021. Recursive filtering of networked nonlinear systems: A survey. International Journal of Systems Science 52, 1110–1128.

[87] Mazzoleni, M., Maccarana, Y., Previdi, F., 2017. A comparison of data-driven fault detection methods with application to aerospace electro-mechanical actuators. IFAC-PapersOnLine 50, 12797–12802.

[88] Means, J.D., 1972. Use of the three-dimensional covariance matrix in analyzing the polarization properties of plane waves. Journal of Geophysical Research 77, 5551–5559.

[89] Middleton, R.H., Goodwin, G.C., 1990. Digital Control and Estimation: A Unified Approach. Prentice Hall PTR, USA.

[90] Morassi, A., 2001. Identification of a crack in a rod based on changes in a pair of natural frequencies. Journal of Sound and Vibration 242, 577–596.

[91] Nguyen, A.T., Guerra, T.M., Sentouh, C., Zhang, H., 2019. Unknown input observers for simultaneous estimation of vehicle dynamics and driver torque: Theoretical design and hardware experiments. IEEE/ASME Transactions on Mechatronics 24, 2508–2518.

[92] Nyholm, S., Smids, J., 2020. Automated cars meet human drivers: responsible human-robot coordination and the ethics of mixed traffic. Ethics and Information Technology 22, 335–344.

[93] Ohnishi, W., Fujimoto, H., Sakata, K., Suzuki, K., 2016. Decoupling control method for high-precision stages using multiple actuators considering the misalignment among the actuation point. IEEJ Journal of Industry Applications 5, 141–147.

[94] Pereira, D.A., Serpa, A.L., 2015. Bank of h filters for sensor fault isolation in active controlled flexible structures. Mechanical Systems and Signal Processing 60, 678–694.

[95] Petit, J., Shladover, S.E., 2014. Potential cyberattacks on automated vehicles. IEEE Transactions on Intelligent Transportation Systems 16, 546–556.

[96] Petrillo, A., Pescapé, A., Santini, S., 2018. A collaborative approach for improving the security of vehicular scenarios: The case of platooning. Computer Communications 122, 59–75.

[97] Petrillo, A., Pescape, A., Santini, S., Mar. 2020. A secure adaptive control for cooperative driving of autonomous connected vehicles in the presence of heterogeneous communication delays and cyberattacks. IEEE Transactions on Cybernetics 51, 1134–1149.

[98] Philip, B.V., Alpcan, T., Jin, J., Palaniswami, M., 2018. Distributed real-time iot for autonomous vehicles. IEEE Transactions on Industrial Informatics 15, 1131–1140.

[99] Pirani, M., Hashemi, E., Khajepour, A., Fidan, B., Litkouhi, B., Chen, S.K., Sundaram, S., 2018. Cooperative vehicle speed fault diagnosis and correction. IEEE Transactions on Intelligent Transportation Systems 20, 783–789.

[100] Prakash, N.P.S., Chen, Z., Horowitz, R., 2021. System identification in multi-actuator hard disk drives with colored noises using observer/kalman filter identification (okid) framework. arXiv preprint arXiv:2109.12460 .

[101] Rahi, A., Yarmohammadi, R., 2020. Crack fault detection in piezoelectric sensors using particle swarm optimization. Transp Phenom Nano Micro Scales 8, 71–80.

[102] Ribeiro, A., Silva, J., Maia, N., 2000. On the generalisation of the transmissibility concept. Mechanical Systems and Signal Processing 14, 29–35.

[103] Riedel, K.S., 1992. A sherman–morrison–woodbury identity for rank augmenting matrices with application to centering. SIAM Journal on Matrix Analysis and Applications 13, 659–662.

[104] Samantaray, A.K., Bouamama, B.O., 2008. Model-based process supervision: a bond graph approach. Springer Science & Business Media.

[105] Seiler, P., Pant, A., Hedrick, K., 2004. Disturbance propagation in vehicle strings. IEEE Transactions on Automatic Control 49, 1835–1842.

[106] Shladover, S.E., 2018. Connected and automated vehicle systems: Introduction and overview. Journal of Intelligent Transportation Systems 22, 190–200.

[107] Singleton, R.K., Strangas, E.G., Aviyente, S., 2014. Extended kalman filtering for remaining-useful-life estimation of bearings. IEEE Transactions on Industrial Electronics 62, 1781–1790.

[108] Sirikham, A., Zhao, Y., Nezhad, H.Y., Du, W., Roy, R., 2018. Estimation of damage thickness in fiber-reinforced composites using pulsed thermography. IEEE Transactions on Industrial Informatics 15, 445–453.

[109] Stefansson, E., Fisac, J.F., Sadigh, D., Sastry, S.S., Johansson, K.H., . Human-robot interaction for truck platooning using hierarchical dynamic games, in: European Control Conference (ECC), pp. 3165–3172, 2019.

[110] Sun, M., Al-Hashimi, A., Li, M., Gerdes, R., 2020. Impacts of constrained sensing and communication based attacks on vehicular platoons. IEEE Transactions on Vehicular Technology 69, 4773–4787.

[111] Swaroop, D., Ph.D. dissertation, University of California, Berkeley, CA, 1994. String stability of interconnected systems: An application to platooning in automated highway systems .

[112] Tao, G., Joshi, S.M., Ma, X., 2001. Adaptive state feedback and tracking control of systems with actuator failures. IEEE Transactions on Automatic Control 46, 78–95.

[113] Taylor, A.H., Droege, M., Shaver, G., Sandoval, J., Erlien, S., Kuszmaul, J., 2020. Capturing the impact of speed, grade, and traffic on class 8 truck platooning. IEEE Transactions on Vehicular Technology 69, 10506–10518.

[114] Tidriri, K., Chatti, N., Verron, S., Tiplica, T., 2016. Bridging data-driven and model-based approaches for process fault diagnosis and health monitoring: A review of researches and future challenges. Annual Reviews in Control 42, 63–81.

[115] Treiber, M., Hennecke, A., Helbing, D., 2000. Congested traffic states in empirical observations and microscopic simulations. Physical review E 62, 1805–1824.

[116] Venkatasubramanian, V., Rengaswamy, R., Kavuri, S.N., 2003. A review of process fault detection and diagnosis: Part ii: Qualitative models and search strategies. Computers & chemical engineering 27, 313–326.

[117] Verçosa, C.A.M., Arruda, J.R.F., 1995. Structural fault localization using direct stiffness update methods, in: International Design Engineering Technical Conferences and Computers and Information in Engineering Conference, American Society of Mechanical Engineers. pp. 1229–1239.

[118] Verron, S., Tiplica, T., Kobi, A., 2010. Fault diagnosis of industrial systems by conditional gaussian network including a distance rejection criterion. Engineering applications of artificial intelligence 23, 1229–1235.

[119] Wang, B., Xu, M., Yang, L., Oct. 2014. Study on the economic and environmental benefits of different ev powertrain topologies. Energy Conversion and Management 86, 916–926.

[120] Wang, J., Zhang, X., Huang, J., Wang, X., Xiong, G., Wang, T., 2020. A modified observer based fault-tolerant control for aircraft with multi-actuator closed-loop system faults, in: CSAA/IET International Conference on Aircraft Utility Systems (AUS 2020), IET. pp. 933–938.

[121] Wang, T., Han, Q., Chu, F., Feng, Z., 2019. Vibration based condition monitoring and fault diagnosis of wind turbine planetary gearbox: A review. Mechanical Systems and Signal Processing 126, 662–685.

[122] Wang, Y., Jiang, B., Lu, N., Pan, J., 2016. Hybrid modeling based double-granularity fault detection and diagnosis for quadrotor helicopter. Nonlinear Analysis: Hybrid Systems 21, 22–36.

[123] Wu, C., Kreidieh, A., Vinitsky, E., Bayen, A.M., . Emergent behaviors in mixed-autonomy traffic, in: Conference on Robot Learning, pp. 398–407, 2017.

[124] Wu, F., Luo, H., Jia, H., Zhao, F., Xiao, Y., Gao, X., 2020. Predicting the noise covariance with a multitask learning model for kalman filter-based gnss/ins integrated navigation. IEEE Transactions on Instrumentation and Measurement 70, 1–13.

[125] Xiao, C., Yu, M., Wang, H., Zhang, B., Wang, D., 2022. Prognosis of electric scooter with intermittent faults: Dual degradation processes approach. IEEE Transactions on Vehicular Technology 71, 1411–1425.

[126] Xiao, C., Yu, M., Zhang, B., Wang, H., Jiang, C., 2021. Discrete component prognosis for hybrid systems under intermittent faults. IEEE Transactions on Automation Science and Engineering 18, 1766–1777.

[127] Xing, H., Ploeg, J., Nijmeijer, H., 2019. Compensation of communication delays in a cooperative acc system. IEEE Transactions on Vehicular Technology 69, 1177–1189.

[128] Xiong, R., Yu, Q., Shen, W., 2018. Review on sensors fault diagnosis and fault-tolerant techniques for lithium ion batteries in electric vehicles, in: 2018 13th IEEE Conference on Industrial Electronics and Applications (ICIEA), IEEE. pp. 406–410.

[129] Yan, W., Tang, D., Lin, Y., 2016. A data-driven soft sensor modeling method based on deep learning and its application. IEEE Transactions on Industrial Electronics 64, 4237–4245.

[130] Yang, H.H., Huang, M.L., Lai, C.M., Jin, J.R., 2018a. An approach combining data mining and control charts-based model for fault detection in wind turbines. Renewable Energy 115, 808–816.

[131] Yang, X., Liang, Y., Chen, W., 2018b. A local structural derivative pde model for ultraslow creep. Computers & Mathematics with Applications 76, 1713–1718.

[132] Yang, Y., Ding, S.X., Li, L., 2016. Parameterization of nonlinear observer-based fault detection systems. IEEE Transactions on Automatic Control 61, 3687–3692.

[133] Ye, L., Yamamoto, T., 2019. Evaluating the impact of connected and autonomous vehicles on traffic safety. Physica A: Statistical Mechanics and its Applications 526, 1–12.

[134] Yılmaz, B., Jasiūnienė, E., 2020. Advanced ultrasonic ndt for weak bond detection in composite-adhesive bonded structures. International Journal of Adhesion and Adhesives 102, 102675.

[135] Youssef, A., Delpha, C., Diallo, D., 2016. An optimal fault detection threshold for early detection using kullback–leibler divergence for unknown distribution data. Signal Processing 120, 266–279.

[136] Yu, M., Lan, D., Huang, Y., Wang, H., Jiang, C., Zhao, L., 2019. Event-based sequential prognosis for uncertain hybrid systems with intermittent faults. IEEE Transactions on Industrial Informatics 15, 4455–4468.

[137] Yu, M., Xiao, C., Jiang, W., Yang, S., Wang, H., 2018. Fault diagnosis for electromechanical system via extended analytical redundancy relations. IEEE Transactions on Industrial Informatics 14, 5233–5244.

[138] Yu, M., Xiao, C., Zhang, B., 2021. Event-triggered discrete component prognosis of hybrid systems using degradation model selection. IEEE Transactions on Industrial Electronics 68, 11470–11481.

[139] Yuan, F., Yu, Y., Wang, W., Tian, G., 2021. A novel probe of dc electromagnetic ndt based on drag effect: design and application in crack characterization of high-speed moving ferromagnetic material. IEEE Transactions on Instrumentation and Measurement 70, 1–10.

[140] Yuan, H., Dai, H., Wei, X., Ming, P., 2020. Model-based observers for internal states estimation and control of proton exchange membrane fuel cell system: A review. Journal of Power Sources 468, 228376.

[141] Zhang, G., Zhang, H., Huang, X., Wang, J., Yu, H., Graaf, R., Sep. 2015. Active fault-tolerant control for electric vehicles with independently driven rear in-wheel motors against certain actuator faults. IEEE Transactions on Control Systems Technology 24, 1557–1572.

[142] Zhang, L., Tseng, E., . Motion prediction of human-driven vehicles in mixed traffic with connected autonomous vehicles, in: American Control Conference (ACC), pp. 398–403, Denver, CO, 2020.

[143] Zhou, J., Guo, A., Celler, B., Su, S., 2014. Fault detection and identification spanning multiple processes by integrating pca with neural network. Applied Soft Computing 14, 4–11.

[144] Zhu, F., Tang, Y., Wang, Z., 2021. Interval-observer-based fault detection and isolation design for ts fuzzy system based on zonotope analysis. IEEE Transactions on Fuzzy Systems .

[145] Zou, L., Wang, Z., Han, Q.L., Zhou, D., 2019. Moving horizon estimation of networked nonlinear systems with random access protocol. IEEE Transactions on Systems, Man, and Cybernetics: Systems 51, 2937–2948.

Appendix A

Appendix 1: Healthy Systems Modeling

A.1 Mixed Platoon Modeling

In this appendix, we introduce an analytical bond graph model of a mixed autonomous and human-driven vehicle platoon. Although the proposed approaches do not require knowledge of the platoon dynamics, this model is used to numerically apply the proposed approaches, and then alter it to characterize the platoon fault dynamics.

A.1.1 Autonomous Vehicle Modeling Using the Bond Graph Approach

In this appendix, we model the electric powertrain topology introduced in [119] using the bond graph approach. Following [119], we consider the drive motor as a Brushless DC Motor that extracts power from the batteries based on the traction control signal. The controller is assumed to be a PI controller to characterize the cruise-control traction with proportional gain $k_{P,j}$ and integral gain $k_{I,j}$. Figure A.1 shows the bond graph model of the vehicle considered, while parameters description and their numerical values are defined in Table A.2. Next, following [136] we introduce the uncertainties in the vehicle parameters directly in the bond graph model. This is done by representing the bond graph model in the linear fractional transformation form. The vehicle parameters are represented by two decoupled parts, the first part is the nominal part $\bar{i} \in \{\bar{R}_j, \bar{I}_j, \bar{S}_j, \bar{M}_j, \bar{M}_j\bar{F}_j\}$, and the second part is the uncertain part $i \in \{\rho_R\bar{R}_j, \rho_I\bar{I}_j, \rho_S\bar{S}_j, \rho_M\bar{M}_j, \rho_F\bar{M}_j\bar{F}_j\}$, where ρ_i is the multiplicative uncertainty on the parameter i. The purpose of this form of uncertainties is to represent the uncertainties by the fictive effort and flow $\mathbf{MS}f$. The uncertain parameter i is then given by $i = \bar{i}(1+\rho_i)$. In practice, there are two methods to obtain the values of the multiplicative uncertainties ρ_i values. The first method is related to the manufacturer design where the manufacturer provides the nominal values such as $\bar{R}_j, \bar{I}_j, \bar{S}_j$ and their range of uncertainties

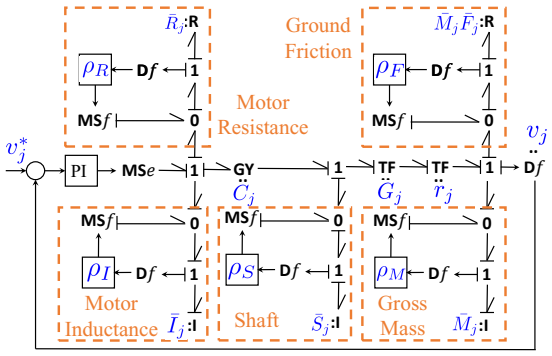

Fig. A.1 Bond graph model of an electric powertrain vehicle that is considered to characterize CAVs.

ρ_R, ρ_I, ρ_S. The second method is associated with vehicle operation, such as vehicle gross mass and ground friction coefficient $\bar{M}_j, \bar{F}_j$. This method identifies ρ_i experimentally using parameter identification techniques such as least squares identification as in Section 3.2.1. As in [136], to calculate the nominal value of a parameter, the mean value of the parameter's observation window is treated as the nominal value, and the difference between the minimum and maximum values is considered as the additive uncertainty. Following the formulation procedure in

Table A.1 Simulation parameters of the platoon model.

Symbol	Description	Value
$\bar{R}_j$	Motor Resistance	18 mΩ
$\bar{I}_j$	Motor Inductance	252 μH
$\bar{C}_j$	Motor Constant	0.26 rad/s.A
$\bar{S}_j$	Shaft moment of inertia	0.2 kg.m^2
G_j	Transmission Ratio	0.2
r_j	Wheel Radius	0.3 m
$\bar{M}_j$	Vehicle gross mass	1478 kg
$\bar{F}_j$	Friction coefficient	0.6
ρ_R	Uncertainty coefficient in R_j	0.04
ρ_I	Uncertainty coefficient in I_j	0.05
ρ_S	Uncertainty coefficient in S_j	0.03
ρ_F	Uncertainty coefficient in M_jF_j	0.04
ρ_M	Uncertainty coefficient in M_j	0.05
$k_{P,j}$	Controller proportional gain	2.5
$k_{I,j}$	Controller integral gain	0.6
$a_{\max}$	Maximum acceleration in (A.1)	1m/s^2
λ	Constant in (A.1)	4
s_0	Minimum spacing distance in (A.2)	2 m

A.1.2 Human-driven Vehicle

For human-driven vehicles, we adopt the human Intelligent Driver Model (IDM) [115]

$$a(t) = a_{\max}\left[1 - \left(\frac{v(t)}{v^*(t)}\right)^{\delta} - \left(\frac{s^*(t,v,\Delta v)}{s(t)}\right)^2\right], \tag{A.1}$$

where $a_{\max}$ is the maximum acceleration, δ is a constant that indicates how slow the human response is, s is the actual spacing distance and s^* is the desired spacing distance and is given by

$$s^*(t,v,\Delta v) = s_0 + \max\left(0, v(t)T + \frac{v(t)\Delta v(t)}{2\sqrt{a(t)a^*(t)}}\right), \tag{A.2}$$

where s_0 is the minimum allowed spacing distance, T is a time constant and Δv is the velocity difference between the vehicle and its preceding vehicle.

A.1.3 CAV Platoon with a Human-driven Vehicle

The communication topology considered each vehicle to receive the velocity from the vehicle in front of it and track it. The vehicle in front of the human-driven vehicle is considered to communicate with the vehicle that follows the human-driven vehicle. The minimal communication links that can be available is used in this word. Any additional communications (e.g. V2V with the second vehicle that follows the human-driven vehicle and V2C) can be used along with the proposed approach as redundant detectors. Note that if the distance between vehicles $i_{\mathrm{H}-1}$ and $i_{\mathrm{H}+1}$ is longer than the V2V communication range, then this platoon is considered as two separate fully autonomous platoons. CAV vehicles send information regarding the position, velocity, and acceleration to the following vehicle via V2V communication links. According to [142], CAV $i_{\mathrm{H}}+1$ receives the information $\begin{bmatrix} s_{i_{\mathrm{H}}-1} & v_{i_{\mathrm{H}}-1} & a_{i_{\mathrm{H}}-1} \end{bmatrix}^{\mathrm{T}}$ via the V2V communication link. Moreover, vehicle $i_{\mathrm{H}}+1$ measures $\begin{bmatrix} s_{i_{\mathrm{H}}} & v_{i_{\mathrm{H}}} & a_{i_{\mathrm{H}}} \end{bmatrix}^{\mathrm{T}}$ using the perception sensors such as radar and LiDAR. For all $j \in \{1 \dots n\}$, the jth vehicle uses the velocity of the preceding vehicle as the desired velocity, that is, $v_j^* = v_{j-1}$. Next, for all $t \geq 0$, let $u(t) = v_1^*(t)$, $y(t) = \begin{bmatrix} v_1(t) & \dots & v_n(t) \end{bmatrix}^{\mathrm{T}}$, then a mixed platoon of n vehicles, where vehicle i_{H} is human-driven can be represented using the state space equations (A.10)-(A.11)

where

$$A = \begin{bmatrix} A_1 & & \dots & & & 0 \\ B_2C_1 & \ddots & & & & \\ \vdots & \ddots & A_{i_\mathrm{H}} & & & \vdots \\ & & B_{i_\mathrm{H}+1}C_{i_\mathrm{H}} & A_{i_\mathrm{H}+1} & & \\ & & & \ddots & \ddots & \\ 0 & & \dots & & B_nC_{n-1} & A_n \end{bmatrix}, \tag{A.3}$$

$$B_v = \begin{bmatrix} B_1 & 0 & \dots & 0 \end{bmatrix}^{\mathrm{T}}, \tag{A.4}$$

$$B_f = \begin{bmatrix} 0 & \dots & 0 & 1 & 0 & \dots & 0 \end{bmatrix}^{\mathrm{T}}, \tag{A.5}$$

$$C = \mathrm{diag}(C_1, \dots, C_n). \tag{A.6}$$

For all $j \in \{1, \dots, n\} \setminus \{i_\mathrm{H}\}$, A_j, B_j and C_j are given by

$$A_j = \begin{bmatrix} 0 & 1 & 0 \\ 0 & 0 & 1 \\ -\gamma_j & -\beta_j & -\alpha_j \end{bmatrix}, B_j = \begin{bmatrix} 0 \\ \delta_j \\ \gamma_j - \alpha_j\delta_j \end{bmatrix},$$
$$C_j = \begin{bmatrix} 1 & 0 & 0 \end{bmatrix}.$$

Without any loss of generality, the human-driven vehicle acceleration a_{i_H} can be written as

$$\begin{aligned} \dot{x}_{i_\mathrm{H}}(t) &= a_{i_\mathrm{H}}(t, x_{i_\mathrm{H}}) \\ &= A_{i_\mathrm{H}} x_{i_\mathrm{H}}(t) + B_{i_\mathrm{H}} C_{i_\mathrm{H}-1} x_{i_\mathrm{H}-1}(t) + f(t,x), \end{aligned} \tag{A.7}$$

such that the human behaviour is split into a linear and nonlinear parts. The IDM model in (A.1) is used to obtain the measurements of the state $x_{i_\mathrm{H}} = v_{i_\mathrm{H}}$, however, $A_{i_\mathrm{H}}, B_{i_\mathrm{H}}$, and f are assumed to be unknowns. We also consider the rest of the platoon model (A.10)-(A.11) to be unknown and only the outputs $y(t)$ are measured from the bond graph model.

A.2 Multi-Actuator Systems

The following analytical model is for a precision motion system used in semiconductor manufacturing and consists of twelve actuators. The proposed approach counts for unknown dynamics thorough a system identification algorithm that will be introduced in the next

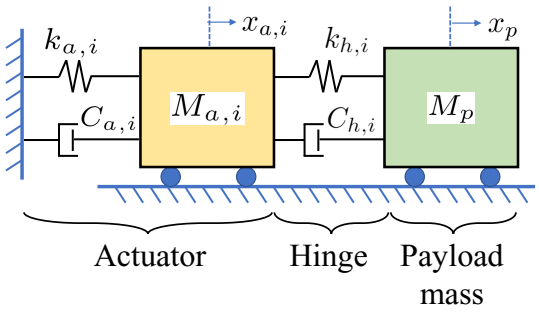

Fig. A.2 Healthy actuator model. f_i is the excitation signal, $M_{a,i}, k_{a,i}$, and $C_{a,i}$, are the equivalent mass, stiffness, and damping coefficients of the actuator, $x_{a,i}$ is the actuator output displacement. The actuator moves the payload mass M_p with the displacement x_p via a hinge with equivalent stiffness $k_{h,i}$ and equivalent damping $C_{h,i}$.

section. This analytical model is used for: (i) Illustrate the applicability of the proposed approach on multi-actuator motion systems, and (ii) Numerical validation and simulation results.

A.2.1 Actuator Model

Although, the detailed model for each class of actuators highly varies, actuators can be simplified into a general second order model for some theoretical investigations such as system control [50]. In [50], the generalized actuator model is given as a second order mass-spring-damper to characterize the dynamics of piezoelectric actuators as shown in Figure A.2. In this model, $f_i(t)$, is the input to the actuator, $M_{a,i}$, $C_{a,i}$, $k_{a,i}$ are the equivalent mass, damping coefficient, and stiffness of the actuator, respectively, $x_{a,i}(t)$, is the output displacement of the actuator, $C_{h,i}$ and $k_{h,i}$ are the hinge damping coefficient and stiffness, respectively, and x_p is the output displacement of the payload mass M_p. This actuator acts on the payload mass with two forces, namely, $F_{k,i}$ and $F_{C,i}$, which are the forces in the hinge stiffness and damping, respectively. Next, for all $i \in \{1,\ldots,n\}$ the actuator output can be written as $F_i(t) = F_{k,i}(t) + F_{C,i}(t)$. Then the state space representation of the ith actuator dynamics can be written as

$$\dot{x}_i(t) = A_i x_i(t) + B_i f_i(t), \tag{A.8}$$

$$F_i(t) = C_i x_i(t), \tag{A.9}$$

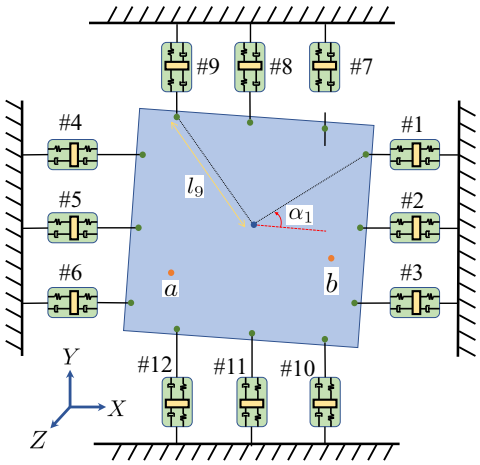

Fig. A.3 Linear time-invariant plant consists of n actuators that move the middle mass m_p in the $X-Y$ plane. The actuators dynamics are shown in Figure A.2.

where

$$A_i = \begin{bmatrix} 0 & 0 & 1 & 0 \\ 0 & 0 & 0 & 1 \\ \frac{-(k_{h,i}+k_{a,i})}{M_{a,i}} & \frac{k_{h,i}}{M_{a,i}} & \frac{-(C_{h,i}+C_{a,i})}{M_{a,i}} & \frac{C_{h,i}}{M_{a,i}}\frac{k_{h,i}}{M_p} \\ \frac{-k_{h,i}}{M_p} & \frac{C_{h,i}}{M_p} & \frac{-C_{h,i}}{M_p} & \end{bmatrix},$$

$$B_i = \begin{bmatrix} 0 & 0 & \frac{1}{M_{a,i}} & 0 \end{bmatrix}^{\mathrm{T}},$$

$$C_i = \begin{bmatrix} k_{h,i} & -k_{h,i} & C_{h,i} & -C_{h,i} \end{bmatrix},$$

and F_i is the output of the actuator.

A.2.2 System Model

Consider a rigid stage that moves in the $X-Y$ plane as shown in Figure A.3 with six actuators in the X direction, three on each side, and six actuators are acting on the Y direction, three on each side as well. The middle stage moves in the $X-Y$ directions and rotates around the Z axis with a small angle $\theta < 10^o$. Let a and b denote two sensors located at two different locations on the rigid sage. Define $u(t) \begin{bmatrix} f_1(t) & \dots & f_n(t) \end{bmatrix}^{\mathrm{T}}$, $y(t) \begin{bmatrix} a_x(t) & a_y(t) & b_x(t) & b_y(t) \end{bmatrix}^{\mathrm{T}}$, and $x(t) \begin{bmatrix} x_1(t) & \dots & x_n(t) & P_x(t) & P_y(t) & P_\theta(t) \end{bmatrix}^{\mathrm{T}}$, where (a_x, a_y) and (b_x, b_y) are the velocities of points a and b, respectively, in the X and Y directions, P_x and P_y are the middle stage momenta in the X and Y directions, respectively, and P_θ is

the angular momentum around the Z axis. Then the state space representation of the system shown in Figure A.3 can be written as

$$\dot{x}(t) = Ax(t) + Bu(t), \tag{A.10}$$
$$y(t) = Cx(t), \tag{A.11}$$

where

$$A = \begin{bmatrix} \bar{A} & 0 \\ \bar{C} & 0 \\ G & 0 \end{bmatrix}, B = \begin{bmatrix} \bar{B} \\ 0 \end{bmatrix}, C = \begin{bmatrix} 0 & E & L \\ 0 & E & \end{bmatrix},$$

where $A \in \mathbb{R}^{s\times s}, B \in \mathbb{R}^{s\times 12}, C \in \mathbb{R}^{4\times s}$, s is the system order that is considered to be unknown,

$$\begin{aligned}
&\bar{A} = \text{diag}(A_1, \ldots, A_{12}),\ \ \bar{B} = \text{diag}(B_1, \ldots, B_{12}), \\
&\bar{C} = \text{diag}(\bar{C}_x, \bar{C}_y),\ \ E = \text{diag}(\frac{1}{M_p}, \frac{1}{M_p}), \\
&\bar{C}_x = \begin{bmatrix} -C_1 & \ldots & -C_3 & C_4 & \ldots & C_6 \end{bmatrix}, \\
&\bar{C}_y = \begin{bmatrix} -C_7 & \ldots & -C_9 & C_{10} & \ldots & C_{12} \end{bmatrix}, \\
&G = \begin{bmatrix} O_{1,3} & -O_{4,6} & -Q_{7,9} & Q_{10,12} \end{bmatrix}, \\
&L = \begin{bmatrix} \frac{l_a}{J}\cos(\alpha_a) & \frac{l_b}{J}\cos(\alpha_b) & \frac{l_a}{J}\sin(\alpha_a) & \frac{l_b}{J}\sin(\alpha_b) \end{bmatrix}^{\mathrm{T}},
\end{aligned}$$

and for $i, j \in \{1, \ldots, n\}, j > i$,

$$\begin{aligned}
O_{i,j} &= \begin{bmatrix} l_i\sin(\alpha_g)C_i & \ldots & l_j\sin(\alpha_j)C_j \end{bmatrix}, \\
Q_{i,j} &= \begin{bmatrix} l_i\cos(\alpha_i)C_i & \ldots & l_j\cos(\alpha_j)C_j \end{bmatrix}.
\end{aligned}$$

For all $i \in \{1, \ldots, 12\}$, A_i, B_i, and C_i are as defined in (A.8)-(A.9), l_i is the distance from actuator i to the middle stage's center of mass, α_i is the angle between l_i and the X axis, M_p and J are the middle stage mass and moment of inertia around the Z axis, respectively, l_a, l_b are the distances between points a, b and the stage center of mass, respectively, and α_a, α_b are the angles between l_a, l_b and the X axis, respectively.

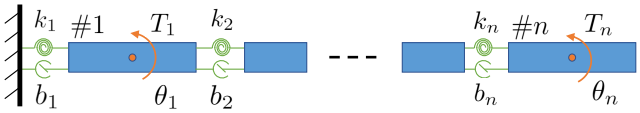

Fig. A.4 Schematic diagram of a flexible cantilever beam modeled as n lumped segments.

A.3 Flexible Beams

Consider the flexible structure in Figure A.4 that is structured as a flexible cantilever beam. This structure is modeled as a lumped mass-spring-damper system with n lumped segments. Each segment is considered to be rigid and connected to the segment before with a torsional spring and damper as shown in Figure A.4. With T_i being the input torque applied to segment i, then taking the summation of torque on segment $i \in \{1,\ldots,n\}$ yields

$$\begin{aligned} I_i\ddot{\theta}_i(t) =& T_i(t) + k_{i+1}\Delta\theta_{i+1}(t) + b_{i+1}\Delta\dot{\theta}_{i+1}(t) \\ & - k_i\Delta\theta_i(t) - b_i\Delta\dot{\theta}_i(t), \end{aligned} \tag{A.12}$$

where I_i, k_i, and b_i are the moment of inertia, torsional stiffness, and torsional damping coefficients of the segment i, respectively. θ_i is the deflection angle of the segment i, $\Delta\theta_i = \theta_i - \theta_{i-1}$ where $\theta_0 = \dot{\theta}_0 = k_{n+1} = b_{n+1} = 0$. The beam model can then be represented on the following state space model,

$$\dot{x}(t) = Ax(t) + B_T T(t) + B_f f(t,x) + B_w w(t), \tag{A.13}$$

$$\dot{\theta}(t) = Cx(t), \tag{A.14}$$

Table A.2 Simulation parameters for the multi-actuator system in (A.10)-(A.11).

Parameter	Description	Value
M_p	Middle stage mass	$2.45kg$
J	Middle stage moment of inertia	$0.0997kg.m^2$
l	Middle stage length	$0.132m$
$M_{a,i}$	Actuator mass	$0.028kg$
$k_{a,i}$	Actuator stiffness	$100 \times 10^6 N/m$
$C_{a,i}$	Actuator damping	$2681.13N.s/m$
$k_{h,i}$	Hinge stiffness	$2 \times 10^4 N/m$
$C_{h,i}$	Hinge damping	$500N.s/m$

Table A.3 Simulation parameters of the flexible beam shown in Figure A.4, where the beam is divided into 10 segments.

Description	Symbol	Value
Segment moment of inertia	I_i	$0.001 kg.m^2$
Segment bending stiffness	k_i	$22 N.m/rad$
Segment bending damping	b_i	$0.01 (N.m)/(rad/sec)$

where

$$
\begin{aligned}
x(t) &= \begin{bmatrix} \theta_1(t) & \dot{\theta}_1(t) & \dots & \theta_n(t) & \dot{\theta}_n(t) \end{bmatrix}^{\mathrm{T}} \\
T(t) &= \begin{bmatrix} T_1(t) & \dots & T_n(t) \end{bmatrix}^{\mathrm{T}}, \\
\dot{\theta}(t) &= \begin{bmatrix} \dot{\theta}_1(t) & \dots & \dot{\theta}_n(t) \end{bmatrix}^{\mathrm{T}} \\
A &= \begin{bmatrix} \alpha_1 & \frac{1}{I_1}\beta_2 & \dots & 0 \\ \frac{1}{I_2}\beta_2 & \alpha_2 & \ddots & \vdots \\ \vdots & \ddots & \ddots & \frac{1}{I_{n-1}}\beta_n \\ 0 & \dots & \frac{1}{I_n}\beta_n & \alpha_n \end{bmatrix}, \\
B &= \mathrm{diag}(\gamma_1, \dots, \gamma_n), \quad C = \mathrm{diag}(\delta_1, \dots, \delta_n), \\
\alpha_i &= \begin{bmatrix} 0 & 1 \\ \frac{-(k_i+k_{i+1})}{I_i} & \frac{-(b_i+b_{i+1})}{I_i} \end{bmatrix}, \quad \beta_i = \begin{bmatrix} 0 & 0 \\ k_i & b_i \end{bmatrix}, \\
\gamma_i &= \begin{bmatrix} 0 & \frac{1}{I_i} \end{bmatrix}^{\mathrm{T}}, \quad \delta_i = \begin{bmatrix} 0 & 1 \end{bmatrix}.
\end{aligned}
$$

The unmodeled dynamics such as shear and tensile deflections are pushed to the unknown bounded nonlinear term $f(\cdot,\cdot)$, w presents the external disturbances, and $B_f = B_w = \begin{bmatrix} 1 & \dots & 1 \end{bmatrix}$. $x \in \mathbb{R}^{2n\times 1}, T \in \mathbb{R}^{n\times 1}, \dot{\theta} \in \mathbb{R}^{n\times 1}, A \in \mathbb{R}^{2n\times 2n}, B \in \mathbb{R}^{2n\times n}$, and $C \in \mathbb{R}^{n\times 2n}$. The state vector x in (A.13) comprises all the deflection angles and angular velocities of the beam. All excitations on the beam are modeled as external torques and collected in the term T. All dynamics that can't be included in the linear term Ax are pushed to f, which includes unmodeled dynamics and parameter uncertainties. w captures the disturbances in the system. Note that the difference between T and w is that T is required and designed (can be a control signal), however, w are unwanted disturbances. Equation (A.14) maps the measured outputs $\dot{\theta}$, which are the segments angular velocities, to the systems states x through the structure of the matrix C.

Appendix B

Appendix 2: Faults Modeling

B.1 Fault Models

In this appendix, we introduce common physical and cyber fault models from the literature. The proposed technique is independent of the fault dynamics and considers any fault to result in the corrupted unknown velocity $\tilde{v}_i$.

B.1.1 Sensor Fault

Perception sensors (radar and LiDAR) play a crucial role in the the autonomous vehicle that follows the human-driven vehicle $i_{\mathrm{H}}+1$ as the velocity v_{i_H} is measured directly from these sensors. Following

B.1.2 Motor/Actuator Disturbances

Brushless DC motors that are used in electric vehicles are subjected to vulnerable operating conditions including high magnetic force and severe weather conditions. Following [141], we introduce an additive fault to the motor's nominal value of the current-to-torque ratio C_i after motor loss of effectiveness occurs. The faulty motor constant is then given by

$$\tilde{C}_i(t) = 0.8C_i + \delta_{C_i}(t), \tag{B.1}$$

where $\tilde{C}_i$ is the corrupted motor constant, and δ_{C_i} is the deviation from the original motor constant after the loss of effectiveness occurs.

B.1.3 Motor Delay

Internal delay in actuators can lead to poor control performance and potential instability [74, 20]. The motor internal delay can be modeled as a time delay between the motor electrical current and the output torque, that is,

$$\tilde{\rho}_i(t) = \rho_i(t - \tau_{e,i}(t)), \tag{B.2}$$

where $\tilde{\rho}_i$ is the delayed current, ρ_i is the original current and $\tau_{e,i}$ is the time-variant motor delay.

B.1.4 False Data Injection (Burst Transmission)

Connected autonomous vehicles platoons have several spacing-distance policies as shown in [111, 105]. One possible cyberattack is burst transmission that can affect the system performance by adding bounded random disturbances to the spacing distance between two preceding vehicles [97]. This fault can lead to instabilities, inaccuracies, and oscillations in the system performance [99, 96, 95]. For all $i = 1, \ldots, n$, let h_i denote the nominal spacing value between vehicle i and vehicle $i+1$, then for all $t \geq 0$,

$$\tilde{h}_i(t) = h_i(t) + \delta_{f,i}(t), \tag{B.3}$$

where $\tilde{h}_i$ denotes the corrupted spacing distance, and $\delta_{f,i}$ denotes the deviation from h_i due to a cyberattack. Spacing distance fault can occur due to corrupted measurements of the velocities of the vehicles. Therefore, v_i can be represented by

$$\tilde{v}_i(t) = v_i(t) + \dot{\tilde{h}}_i(t), \tag{B.4}$$

where for all $i = 1, \ldots, n$, $\tilde{v}_i$ represents the corrupted measurements of the velocity of vehicle i, $\dot{\tilde{h}}_i$ denotes the deviation from v_i due to a cyberattack.

B.1.5 Denial-of-service

Time delays in connected autonomous vehicles platoons can yield fatal faults [76]. One of the main malicious cyberattacks in vehicle platoons is the Denial-of-Service (DoS) attack [97]. DoS attack increases the service time in the communication link, which makes it busier and results in a communication time delay within the communication link. Note that, as the service time increases, the packet transmitted fades, which is known as the packet loss. In

this work, we consider small-time communication delays that cause the packet to arrive late. For all $i = 1, \ldots, n$, consider the velocity of the i-th vehicle v_i, then a delay in v_i yields the corrupted signal

$$\tilde{v}_i(t) = v_i(t - \tau_{v,i}(t)), \tag{B.5}$$

where $\tau_{v,i}$ is a relatively small time-variant communication delay in v_i that does not cause any packet loss.

Table B.1 Drunk driving conditions according to the alcohol concentration and the corresponding mathematical models.

BAC (g/dL)	Effects on driving	Mathematical model
0.02	1) Decline in visual functions 2) Decline in ability to perform two tasks at the same time	$\tilde{s}^*_{i_\mathrm{H}}(t) = s^*_{i_\mathrm{H}}(t) + \delta_{s^*}(t)$ $\lambda = 3$
0.05	1) Reduced coordination 2) Reduced ability to track moving objects 3) Reduced response to emergencies	$\tilde{s}_{i_\mathrm{H}}(t) = s_{i_\mathrm{H}}(t) + \delta_s(t)$ $\tilde{v}_{i_\mathrm{H}-1}(t) = v_{i_\mathrm{H}-1}(t - t_v)$ $\lambda = 2$
0.08	1) Short-term memory loss 2) Poor speed control 3) Impaired perception 4) Reduced information processing capability	$\tilde{v}_{i_\mathrm{H}-1}(t) = v_{i_\mathrm{H}-1}(t) + \delta_{i_\mathrm{H}-1}(t)$ $\tilde{v}_{i_\mathrm{H}}(t) = v_{i_\mathrm{H}}(t) + \delta_{i_\mathrm{H}}(t)$ $\tilde{s}_{i_\mathrm{H}}(t) = s_{i_\mathrm{H}}(t - t_s)$ $\lambda = 1$

B.2 Drunk Driver Model

The human-driver behavior in human-driven vehicles is unknown and difficult to be predicted due to many reasons such as different driving experiences and sudden changes in decisions. The proposed approach considers unknown human-driver behavior and is independent of the human effects. However, the alterations in the driver behavior due to increasing the BAC level are known. For example, regardless of how slow or fast, the human-driver response is, increasing the BAC level in the driver's blood will always result in a slower response. The proposed approach mission is capturing (identifying) the unknown healthy human-driver behavior and then inspecting the existence of any drunkenness alterations. This section inspects the drunk driving conditions and their alterations from the healthy driver behavior. The next section shows how to capture healthy driver behavior.

B.2.1 Drunkenness Driving Conditions

In this section, we introduce the drunkenness alterations in the normal human drivers due to increasing the BAC to different levels. The following alterations are related to the BAC levels

and the drunken driving conditions and are independent of the healthy driver behavior. For clarification purposes only, these alterations are applied to the healthy driver model example introduced in section A.1.2. The BAC levels range from relatively low to relatively high and are shown to have different effects on each level. This drunk driver model is then used to test the drunk driver detection algorithm in section 3.4.

Increasing the BAC level results in several effects on the driving conditions, as listed in Table B.1

Let $\tilde{s}^*_{i_H}$, $\tilde{s}_{i_H}$, $\tilde{v}_{i_H}$, and $\tilde{v}_{i_H-1}$, denote the corrupted measurements of $s^*_{i_H}$, s_{i_H}, v_{i_H}, and v_{i_H-1}, respectively. Moreover, let δ_{s^*}, δ_s, δ_{i_H}, and δ_{i_H-1}, be the corruptions in the measurements of $\tilde{s}^*_{i_H}$, s_{i_H}, v_{i_H}, and v_{i_H-1}, respectively. For BAC value of around $0.02g/dL$, a decline in visual functions arises, which we model as inaccuracies added to the desired spacing distance, that is, $\tilde{s}^*_{i_H}(t) = s^*_{i_H}(t) + \delta_{s^*}(t)$. Losing the ability to perform two tasks at the same time (i.e. tracking the vehicle ahead and following the road signs) leads to a delay in one task to perform the other, which is modeled as a slight delay in the drivers response $\lambda = 3$. At BAC $= 0.02g/dL$, the driver model in (A.1) becomes

$$\tilde{a}_{i_H}(t, v_{i_H}) = a_{\max}\left[1 - \left(\frac{v_{i_H}(t)}{v^*_{i_H}(t)}\right)^3 - \left(\frac{\tilde{s}^*_{i_H}(t, v_{i_H}, \Delta v)}{s_{i_H}(t)}\right)^2\right]. \tag{B.6}$$

For BAC levels around $0.05g/dL$, the reduced coordination effect is modeled as inaccuracies added to the vehicle position $\tilde{s}_{i_H}(t) = s_{i_H}(t) + \delta_s(t)$. The main moving object that the human-driver is expected to track is the front vehicle, we model this effect as a time delay in the velocity of the front vehicle, that is, $\tilde{v}_{i_H-1}(t) = v_{i_H-1}(t - t_{i_H})$. Moreover, the drunk driver loses the ability to respond to emergencies such as sudden brake which produces a slower response such that $\lambda = 2$. Thus, (B.6) becomes

$$\tilde{a}_{i_H}(t, v_{i_H}) = \\ a_{\max}\left[1 - \left(\frac{v_{i_H}(t)}{v_{i_H-1}(t - t_v)}\right)^2 - \left(\frac{\tilde{s}^*_{i_H}(t, v_{i_H}, \Delta v)}{\tilde{s}_{i_H}(t)}\right)^2\right]. \tag{B.7}$$

For BAC around $0.08g/dL$, losing the short-term memory is modelled as inaccuracies added to the front vehicle velocity $\tilde{v}_{i_H-1}(t) = v_{i_H-1}(t) + \delta_{i_H-1}(t)$. The poor speed control prevents the drunk driver to maintain an accurate speed for the vehicle, we model this effect as inaccuracies added to the vehicle velocity $\tilde{v}_{i_H}(t) = v_{i_H}(t) + \delta_{i_H}(t)$. The impaired perception is modelled as losing the ability to maintain the vehicle position within the platoon $\tilde{s}_{i_H}(t) = s_{i_H}(t - t_s)$. The reduced information processing capability results in an even slower

response, such as $\lambda = 1$ can be used. Thus, the drunk driver model in (B.7) becomes

$$\tilde{a}_{i_{\mathrm{H}}}(t, v_{i_{\mathrm{H}}}) = \\ a_{\max}\left[1 - \left(\frac{\tilde{v}_{i_{\mathrm{H}}}(t)}{\tilde{v}_{i_{\mathrm{H}}-1}(t-t_v)}\right) - \left(\frac{\tilde{s}^*_{i_{\mathrm{H}}}(t, v_{i_{\mathrm{H}}}, \Delta v)}{\tilde{s}_{i_{\mathrm{H}}}(t-t_s)}\right)^2\right]. \tag{B.8}$$

Therefore, the driver model in (A.7) can be written as

$$\tilde{a}_{i_{\mathrm{H}}}(t, x_{i_{\mathrm{H}}}) = \tilde{A}_{i_{\mathrm{H}}} x_{i_{\mathrm{H}}}(t) + \tilde{B}_{i_{\mathrm{H}}} C_{i_{\mathrm{H}}-1} x_{i_{\mathrm{H}}-1}(t) + \tilde{f}(t, x), \tag{B.9}$$

where $\tilde{A}_{i_{\mathrm{H}}}, \tilde{B}_{i_{\mathrm{H}}}$, and $\tilde{f}$ characterize the human-driver model with $A_{i_{\mathrm{H}}}, B_{i_{\mathrm{H}}}$, and f while the driver is drunk.

B.3 Fatigue Crack

Although the proposed approaches are independent of the fault dynamics, this section models fatigue cracks in flexible beams for testing purposes only. Fatigue cracks are common in flexible structures due to load-unload operation. Following [66], we model the initiation of fatigue cracks as changes in the stiffness at the location of the crack. This change in stiffness grows over time till a complete failure. Therefore, detecting and localizing the change in stiffness is detecting and localizing structural cracks at the early stages. As shown in [66, 56], fatigue cracks result in decreasing the bending stiffness at the location of the crack while the crack is open, and they result in no effect on the beam while the crack is closed. Thus, fatigue cracks are modeled as losses in tension stiffness only, while it makes no change in compression. The stiffness of the segment i under a fatigue crack is given by

$$\tilde{k}_i = \begin{cases} k_i, & \text{for closed crack,} \\ \frac{2k_i}{3}, & \text{for open crack,} \end{cases} \tag{B.10}$$

where $\tilde{k}_i$ is the corrupted stiffness due to the fatigue crack.

B.3.1 Actuator Loss of Effectiveness (Creep Fault)

The creep fault as introduced in [131] is an increase in the stiffness of the structure and can occur due to severe operating conditions. That is,

$$k_{h,i,\mathrm{creep}} = 1.3 k_{h,i}, \tag{B.11}$$

where $k_{h,i,\text{creep}}$ is the hinge stiffness of the actuator i after the creep fault. The faulty actuator needs higher excitation signal amplitude to achieve the desired actuator output force, and thus this fault is referred to as *loss of effectiveness*.